The Microscopic Insight into Fracturing of Brittle Materials with the Discrete Element Method

Piotr Andrzej Klejment

MONOGRAPHIC VOLUME

The Microscopic Insight
into Fracturing of Brittle Materials
with the Discrete Element Method

Piotr Andrzej Klejment

C O N T E N T S

Abstract

Geophysics is an extremely vast field of science that studies the physical processes taking place on Earth or other planets. One of such processes is fracturing of materials. To support these statesments two phenomena can be mentioned. Materials subjected to extreme external conditions, such as ice or rock masses, after exceeding their certain strength parameters, start to fracture, which is manifested by glaciers calving or catastrophic earthquakes.

Despite the huge scientific progress made in recent decades, many issues in geophysics are still unexplained. The commonly used laboratory and field research methods have their limitations. Therefore, in recent years, a relatively new research technology, the numerical modelling, has raised the interest. The rapidly increasing power of computers allows to create more and more sophisticated models and study phenomena to which traditional research methods do not give access.

In this work, the analysis of the issue of material fracturing in geophysical applications was undertaken. The Discrete Element Method was used, which is ideally suited for simulating the fracturing process, because it assumes a discrete model of matter (consisting of particles), and also allows to considerate all kinds of issues related to particle rotations and movements. The research consisted of two stages. In the first one, it was attempted to simulate material cracking during three different material tests: uniaxial compression, Brazilian test and uniaxial stretching. The aim was to obtain data that cannot be obtained during laboratory measurements. These include: particles energy – kinetic energies of linear and rotational motions, as well as, potential energies of bonds between particles; dependencies between microscopic parameters of bonds and particles, and macroscopic parameters of the whole material, as well as the influence of particle size on material behaviour under the influence of external loading.

In the second stage of the research, the transition to the extremely important and current problem of climate change was undertaken. As a result of global warming, glaciers lose more of their mass as a result of the so-called calving, i.e., the phenomena when the block of ice breaks off and falls into the water. Again, the essence of this process is the fracturing, and the DEM method can be very useful for analysing this process. As part of the research, a DEM model of calving glacier was created. Various scenarios were analysed when blocks of different sizes fall from different heights. Inside glacier and water, a network of receivers was created, measuring accelerations during the entire simulation. An attempt was made to determine how two parameters related to calving (the size of the falling down block of ice and the height from which the fall occurs) affect the acceleration of water and glacier particles.

The obtained data provided information about materials fracturing. As part of the uniaxial compression simulation, it was found that the fracturing materials are characterized by a constant relationship between different potential energies of bonds between particles, regardless of their macroscopic parameters. The highest potential energies occurred during compression and shearing between particles, the smallest in relation to bending and rotations. In the case of the Brazilian test, the linear relationship between the critical stress (at which the fracture occurs) and the inverse of the size of the smallest particles forming the material is probably the most interesting. In the uniaxial stretching test, three classes of material cracking were discovered, depending on the bonds parameters between the particles. Simulations of glacier calving provided information about the propagation of the signals in a material similar to water and ice.

ANALIZA PARAMETRÓW MIKROSKOPOWYCH PROCESU PĘKANIA MATERIAŁÓW KRUCHYCH PRZY POMOCY METODY ELEMENTÓW DYSKRETNYCH

Streszczenie

Geofizyka to niezwykle rozległa dziedzina, która zajmuje się badaniem Ziemi lub innych planet. Jednym z najczęstszych zjawisk, które leży u podstaw wielu procesów geofizycznych, jest pękanie materiałów. Dla poparcia tych słów wymienić można dwa takie procesy, niezwykle imponujące i przemawiające do wyobraźni, czyli trzęsienia ziemi oraz cielenie się lodowców. Poddane ekstremalnym warunkom zewnętrznym materiały, takie jak lód lub masy skalne, po przekroczeniu parametrów wytrzymałościowych zaczynają pękać, co przejawia się obrywaniem się mas lodu od czoła lodowca lub katastrofalnymi trzęsieniami ziemi.

Mimo ogromnego postępu naukowego, dokonanego w ostatnich dziesięcioleciach, wiele zjawisk w geofizyce wciąż pozostaje niewyjaśnionych. Stosowane powszechnie badawcze metody laboratoryjne oraz terenowe mają swoje ograniczenia. Dlatego w ostatnich latach coraz większe zainteresowanie wzbudza stosunkowo nowa technologia badawcza, jaką jest modelowanie numeryczne. Wzrastająca w szybkim tempie moc obliczeniowa komputerów pozwala na tworzenie coraz bardziej wyrafinowanych modeli i badanie zjawisk, do których tradycyjne metody badawcze nie dawały dostępu.

W niniejszej pracy podjęto się analizy zagadnienia pękania materiałów w zastosowaniach geofizycznych. Zastosowana zastała Metoda Elementów Dyskretnych, która idealnie nadaje się do symulowania procesu pękania, gdyż zakłada dyskretny model materii (składający się z cząstek), a także umożliwia rozpatrywanie wszelkiego rodzaju zagadnień związanych z ruchem obrotowym i postępowym cząstek. Przeprowadzone prace badawcze składały się z dwóch etapów. W pierwszym, podjęto się symulacji pękania materiału podczas trzech różnych testów materiałowych: ściskania jednoosiowego, próby brazylijskiej oraz jednoosiowego rozciągania. Celem było uzyskanie danych, których nie da się otrzymać podczas pomiarów laboratoryjnych. Należą do nich: energie cząstek – kinetyczna ruchu liniowego i rotacyjnego oraz energia potencjalna wiązań między cząstkami; zależności pomiędzy parametrami mikroskopowymi wiązań i ziaren oraz parametrami makroskopowymi materiału jako całości, a także wpływ wielkości cząstek (ziaren) na zachowanie materiału pod wpływem obciążenia zewnętrznego.

W drugim etapie badań podjęto się przejścia do niezwykle istotnego oraz bieżącego problemu, jakim są zmiany klimatyczne. Na wskutek ocieplenia klimatu lodowce tracą coraz większą część swojej masy w wyniku tzw. cielenia, czyli oberwania się bloku lodu i jego upadku do wody. Ponownie istotą tego procesu jest zjawisko pękania, a metoda DEM może być bardzo przydatna przy analizie tego procesu. W ramach przeprowadzonych badań stworzony został model lodowca, którego fragment pęka i spada do wody. Przeanalizowano różnorodne scenariusze, gdy bloki o różnych rozmiarach spadają z różnej wysokości. Wewnątrz lodowca i wody stworzono sieć odbiorników, mierzących przyspieszenia podczas całej symulacji. Podjęto próbę określenia, jak dwa parametry związane z cieleniem (rozmiar odrywającej się bryły lodu oraz wysokość, z której ta bryła spada) wpływają na przyspieszenia cząstek wody i lodowca.

Uzyskane dane dostarczyły informacji o sposobie, w jaki pękają materiały. W ramach symulacji ściskania jednoosiowego udało się stwierdzić, między innymi, że pękające materiały cechują się stałą zależnością pomiędzy różnymi energiami potencjalnymi wiązań pomiędzy cząstkami, niezależnie od ich parametrów makroskopowych. Największe energie potencjalne występowały podczas ściskania i ścinania pomiędzy cząstkami, najmniejsze w związku ze zginaniem oraz obrotami. W przypadku wyników dotyczących próby brazylijskiej, prawdopodobnie najbardziej interesująca jest liniowa zależność pomiędzy naprężeniem krytycznym (przy którym następuje pęknięcie) oraz odwrotnością rozmiaru najmniejszych cząstek tworzących materiał. W przypadku próby rozciągania jednoosiowego, odkryte zostały trzy klasy pękania materiału w zależności od parametrów wiązań pomiędzy cząstkami. Symulacje pękania lodowca dostarczyły informacje o propagacji sygnału w materiale podobnym do wody i materiale podobnym do lodu.

1. INTRODUCTION

Fragmentation of solid materials is an extremely complicated process that includes processes in scales from atomic (breaking intermolecular bonds) up to a scale of thousands of kilometers in the event of catastrophic earthquakes (Teisseyre 1995; Udias et al. 2014). Such a large range of the scales involved in the process raises numerous questions such as existence of factors determining the final size of the fractured area, existence of possible precursors, or scalability of cracking processes (Christensen 2013).

The well-known fact is that cracking of solid bodies is determined by the structure of the given material, and the way of applying external forces leading eventually to its destruction and fragmentation (Jaeger et al. 2007; Carmona et al. 2008). The cracking process can be described at three different levels: macroscopic (typical engineering approach), mesoscopic – underlying statistical aspects of cracking, and finally microscopic – dealing directly with physical processes at the crack tip.

The macroscopic description of the cracking process has started after pioneering vision of Griffith (1921). According to this approach, the fragmentation of brittle materials can be understood as the development of a single crack in the material that finally leads to its splitting into parts. Depending on the external load, such a crack can be static, steady in time, or enter a dynamic regime when its length increases rapidly, which can finally lead to the fragmentation of the material. An accurate analysis of the complexity of the fracture process or/and interactions of micro-cracks at large concentrations typical for the prefracture state is possible only in terms of statistical models. The kinetic model of the evolution of crack population was introduced (Petrov et al. 1970; Czechowski 1991) and developed by (Czechowski 1993, 1995, 1997, 1998, 2000). It lies at a level intermediate between the purely statistical approach and the fully microscopic approach. The elementary objects are microcracks which can nucleate, propagate and coalesce. The kinetic approach operates on the crack size distribution function whose evolution is governed by the modified coagulation equation (mesoscopic level).

Finally, breaking of solid materials can be analyzed at the microscopic level by knowing directly the physical processes in the crack tip area. This approach, depending on the formulation can go down to the molecular dynamic (atomic) level and analyze conditions and processes of breaking chemical bonds between atoms, creating the given material. This approach requires fully quantum-mechanical description. An alternative microscopic approach does not deal with atoms but operates at the level of grains forming the material and describes their evolution as a set of rigid objects interacting according to the classical Newtonian principles. This approach is quite attractive from the geophysical point of view due to the typically observed grainy structure of all known geomaterials. Moreover, with such approach it is currently possible to simulate the numerical behaviour of quite realistic objects. This microscopic approach is adopted in this work.

Classical engineering approach to the fracturing problem is rooted in continuum mechanics and is based mainly on the computer technique called Finite Element Method. As this technique allows simulations of both elastic and large deformation processes, it has become very popular in engineering applications. However, the final effect of cracking, that is, fragmentation of an object at hand, can hardly be described by this approach in a numerically efficient way, because it requires a solution to the problem of nontrivial evolving in time boundary conditions. Another proposed approach is the Discrete Element Method (DEM), which by definition implies "molecular" construction of matter. The basic concept underlying DEM is to represent an investigated body as an assemblage of discrete particles interacting with each other. Breaking interaction bonds between particles induced by external forces immediately implies creation/evolution of boundary conditions. Such simulations provide an alternative way of measuring

the properties of a material, as well as yield insight into its microscopic parameters (Kun and Herrmann 1996, 1999; Kun et al. 2013, 2014).

Measurement of the characteristics and behaviour of substances under various conditions is a field of materials testing. The data obtained in this way can be used in specifying the suitability of materials for various applications, as well as to construct mathematical models that utilize known material characteristics and behaviour to predict capabilities of the structure. Within the scope of this book the DEM method was applied to analyse fracturing process during three most primary material tests – uniaxial compression, Brazilian test, uniaxial stretching. The research performed provided an insight into fragmentation of materials under external load.

The most basic test is an uniaxial compression in which cylindrical specimen from drilled cores is loaded axially up to failure or any other prescribed level. Simulations of uniaxial compression concerned the three groups of issues: dependency between microscopic and macroscopic parameters of samples, as well as changes in potential energy of bonds and average kinetic energy of particles. Especially interesting was considering potentials energies of bonds. It appeared that the average percentage contribution of different potential energies of bonds to the average overall potential energy of bonds during the breaking process is constant, regardless of macroscopic parameters of the sample. Subsequently, Brazilian test was considered as an indirect method for measurements of the tensile strength of solid materials. This method relies on a diametrical loading of a disk-shaped sample of the brittle material until it splits apart due to an induced tensile stress. The planned simulations were aimed at following the evolution of the total kinetic and potential energies during loading, and identification of stages in response of the samples to constant speed loading. It was also observed how the size of used particles influenced each of the above stages. The last part of materials testing were simulations of uniaxial stretching, mainly focused on cracking of hypothetical three-dimensional materials subjected to force stretching with constant velocity. An attempt was made to distinguish (by analyzing stress-strain curves) different types of cracking; it means, when multicracking occurs and the cracking is dispersed in time, when dominating macro-cracks accompanied by smaller micro-cracks develop; and when a single crack is created.

Results received within the scope of material test simulations have become the basis for a large scale fracturing simulations, presented in the second part of this book. In this case, the DEM method was applied to simulate the fragmentation process in a glaciology – a branch of geophysics, which is now becoming one of the key research directions worldwide. The reason for this are current climate changes, which give a high priority to research on polar regions, particularly to glaciers. It turns out that the current scale of changes is unique in the scale of history. The World Glacier Monitoring Service reported in 2013 (basing on data from 100 glaciers around the world) that the mass balance for all reference glaciers is constantly decreasing (The World Glacier Monitoring Service, https://wgms.ch). This process has accelerated especially in the last 30 years.

In the light of the abovementioned facts, the scientific research on glaciers has become crucial for understanding these disquieting changes. Current climate changes cause that glaciers loss their mass especially due to calving. Very promising and interesting approach offers analysis of signals which are spread by calving glaciers. Głowacki et al. (2016) discovered that due to analysis of underwater sounds associated with calving glacier, it is possible to estimate how much of ice was detached. This relatively simple method can say not only when the glacier is calving, but also allows to discriminate different types of this phenomenon. Motivated by abovementioned approach, the second part of this work was devoted to the creation of a DEM model of the calving glacier. The DEM has a great potential in the area of glaciology. This model consisting of discrete particles is very suitable to simulate fracturing of ice, especially large masses of ice (glacier calving, glaciers surging), icebergs, ice floe, etc. A numerical

model, presented in this dissertation, represents the forehead of glacier and the water beneath it. Under the influence of the force of gravity, the fragment of the glacier cracks and fell into the water. Various possible scenarios were explored when a block of different size fell to water from different heights. The whole process was tracked and recorded by a network of receivers placed in a water reservoir, as well as inside the glacier. The results obtained in this way allowed to discover the dependence between different scenarios of calving and resulting wave propagation in the water.

Fragmentation of solid materials is at the heart of many processes in geophysics. In order to visualize diversity of processes covered by geophysics, it is worth recalling a very vivid depiction written by Morton (2002): "The earth stretches, it wiggles and breathes. Ocean floors begin to move and continents start to wander. Migrating continents and sliding oceans cause volcanic eruptions and earthquakes. Volcanos give birth to hot springs, geysers, and mineral waters. These dynamics contribute to and help drive the earth's atmosphere, producing climatic change and ice ages. This is earth music: earth rhythms from earth processes". As it appears from the above description, a significant part of the processes covered by the geophysics is the study of substances that form the Earth. Therefore, the main purpose of this study, which was to better understand what happens to materials when they break into fragments, fits in to the new trends in geophysical research.

2. FRACTURING OF MATERIALS

A fracture is the separation of a material into pieces under the action of stress (Hertzberg 1976; Tetelman and McEvily 1967). In case of a solid, the fracture usually occurs due to the development of some displacement discontinuity surfaces inside the material. When the displacement develops perpendicular to the surface of displacement, it is called a crack or a normal tensile crack (Łuksza 2014; Neimitz 1998; Rymarz 1993). When the displacement develops tangentially to the surface of displacement, it is called a shear crack, slip band or dislocation. Fractures may occur in two ways (Anderson 1991). Brittle fractures appear with no apparent deformation before the fractures, meanwhile, ductile fractures occur after visible deformation. A quite important factor linked with fracturing is the fracture strength or the breaking strength which describes the stress when a specimen fails or fractures. All aspects of how a fracture occurs in materials are covered by fracture mechanics (Derski et al. 1982).

2.1 Types of deformation

Deformation refers to any changes in the shape or size of an object due to an applied force or a change in temperature (Courtney 1990). In the first case, the deformation energy is transferred through work, whereas in the second case the deformation energy is transferred through heat (Garbarczyk 2000). It is feasible to distinguish different possible types of the applied force: tensile (pulling) forces, compressive (pushing) forces, shear, bending or torsion (twisting). The most significant factor, determined by the temperature, is the mobility of structural defects such as grain boundaries, point vacancies, line and screw dislocations, stacking faults and twins in both crystalline and non-crystalline solids (Elliott 1998, Garbarczyk 2000). The movement or displacement of such mobile defects is thermally activated, and thus limited by the rate of atomic diffusion. Another term for deformation is a strain. When deformation occurs, internal inter-molecular forces develope, to oppose the applied force. These forces may resist the applied force if the applied force is not too large. In such cases, the object may assume a new equilibrium state and return to its original state when the load is removed (Anderson 1991). In case of larger applied force, a permanent deformation may occur and even leads to the structural failure (Garbarczyk 2000).

Four basic types of deformation can be distinguished (Anderson 1991): elastic deformation, plastic deformation, metal fatigue and fracture. *Elastic deformation* is reversible type of deformation, it means, when the forces are no longer applied, the object returns to its original shape. Normal metals, ceramics, and most crystals exhibit linear elasticity and smaller elastic range (Knott 1973). Linear elastic deformation is governed by Hooke's Law $\sigma = E\varepsilon$, where σ is the applied stress, E is a material constant called Young's modulus or elastic modulus, and ε is the resulting strain. This relationship applies in the elastic range and can be used to find Young's modulus. The elastic range ends when the material reaches its yield strength. After this point, plastic deformation begins (Sochor 1998). *Plastic deformation* is an irreversible type of deformation. Materials such as ductile metals – copper, silver, and gold – have rather large plastic deformation range. Crystals and ceramics have minimal plastic deformation range. Under tensile stress, plastic deformation is characterized by a strain hardening region and a necking region and, finally, fracture. The material becomes stronger during strain hardening due to the movement of atomic dislocations. The necking phase is caused by a reduction in the cross-sectional area of the specimen (Knott 1973). When the ultimate strength is achieved, the necking begins – this means that the material can no longer withstand the applied stress and the strain in the specimen rapidly increases. The final effect of the plastic deformation is the fracture of the material. *Metal fatigue* occurs mainly in ductile metals. It was originally thought that a material in elastic deformation range returns to its original state once the forces are removed. However, faults are introduced at the molecular level with each deformation (Knott 1973). As a result, after many deformations cycles cracks will begin to appear and, consequently, fracture, with no apparent plastic deformation in between. Depending on many factors, failure may occur even after millions, billions or trillions of deformations cycles. *Fracture* is an irreversible type of deformation. When a material reaches the end of the elastic and plastic deformation ranges, a break occurs. At the breaking point forces accumulate until they are sufficient to cause a fracture (Hertzberg 1976). If there is no dulling of the edge of the crack face, the local stress before breakage can reach very high values and can reach the theoretical strength of the material. In this case it is large enough to disrupt the bonds between atoms in a specific area – the crack grows between a pair of atomic planes (Knott 1973).

Propagation of cracks in materials is the domain of fracture mechanics. This science was started by aeronautical engineer A.A. Griffith (Griffith 1921; Courtney 1990), to explain the failure of brittle materials. Fracture mechanics applies the physics of stress and strain behaviour of materials, in particular the theories of elasticity and plasticity, to the microscopic crystallographic defects found in real materials in order to predict the macroscopic mechanical behaviour of those bodies (Hertzberg 1976). Because brittleness of materials is the main area of this work, in the next subchapter some basic assumptions of fracture mechanics are described. The content of the next subchapter is mostly based on (Roylance 2001b).

2.2 Basics of the fracture mechanics

2.2.1 The energy-balance approach

Charles E. Inglis was famous for calculating the stress concentrations around elliptical holes and attempting to use them to predict fracture strengths (Courtney 1990). However, Inglis had a serious problem with the crack tip. In his solution, the stresses approach infinity at the crack tip in the limit of a perfectly sharp crack. Using such a result would predict that materials would have near-zero strength – even for very small applied loads, the stresses near crack tips would become infinite. Alan A. Griffith solved this problem and created one of the most famous developments in materials science, the energy-balance approach (Anderson 1991; Zehnder 2012).

If a material is linear ($\sigma = E\varepsilon$), then the strain energy per unit volume is given as follows:
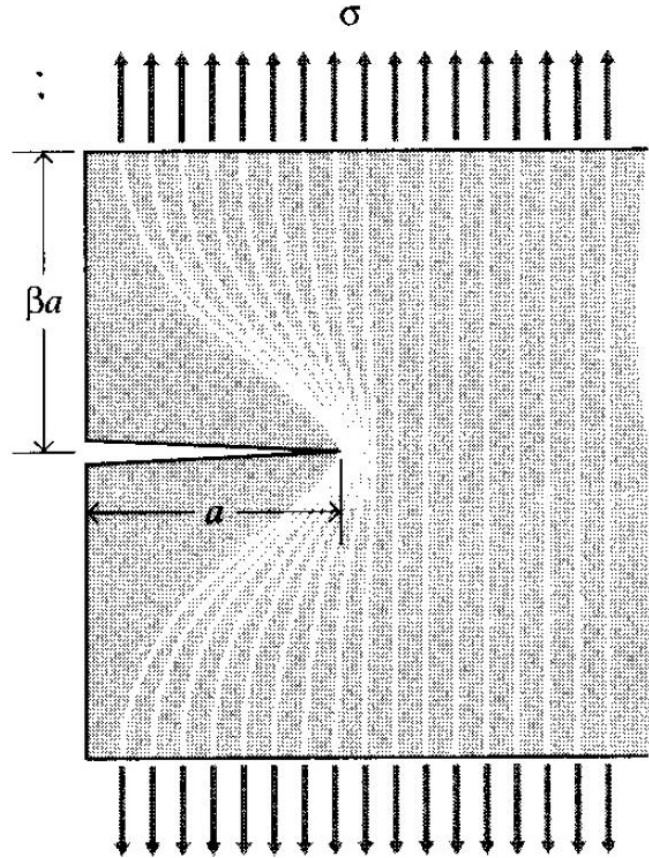
Fig. 1. Idealization of unloaded region near crack flanks (from Roylance 2001b).

$$U^* = \frac{E\epsilon^2}{2} = \frac{\sigma^2}{2E} \qquad (1)$$

Griffith, on the basis of Inglis solution, used a crack depth a inside a solid to compute how much strain energy is released.

Two triangular regions near the crack flanks, illustrated in Fig. 1, of width a and height βa, are regarded as being completely unloaded. The remaining material undergoes the full stress σ. The parameter β for plane stress loading is equal to π. Finally, the total strain energy U released is the strain energy per unit volume times the volume in both triangular regions:

$$U = -\frac{\sigma^2}{2E} \cdot \pi a^2 \qquad (2)$$

Because the dimension normal to the *x-y* plane is taken to be unity, U is the strain energy released per unit thickness of the specimen. This strain energy is liberated by crack growth. But in forming a crack, bonds must be broken, and as a result, the requisite bond energy is absorbed by the material. The surface energy S associated with a crack of length a (and unit depth) is given as follows:

$$S = 2\gamma a \qquad (3)$$

where γ is the surface energy (e.g., joules/meter^2) and the factor 2 is needed as two free surfaces have been formed. As shown in Fig. 2, the total energy associated with the crack is then the sum of the (positive) energy absorbed to create the new surfaces, and the (negative) strain energy liberated by allowing the regions near the crack flanks to become unloaded.
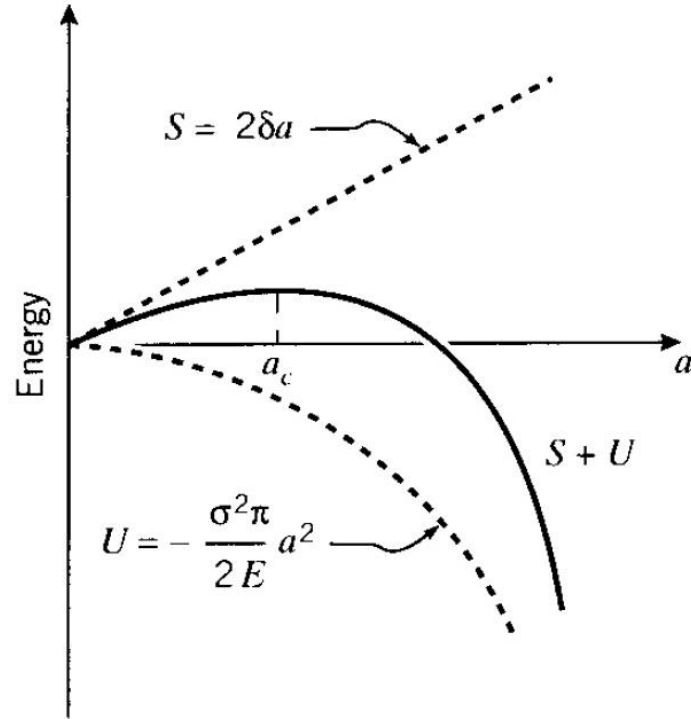
Fig. 2. The fracture energy balance (from Roylance 2001b).

As the crack grows longer (a increases), the quadratic dependence of strain energy on a eventually dominates the surface energy, and beyond the critical crack length a_c the system can lower its energy by allowing the crack grow still longer (Hertzberg 1976). Up to the point where $a = a_c$, the crack will grow only if the stress is increased. Beyond that point, the crack growth is spontaneous and limited only by size/shape of the body.

The value of the critical crack length can be found by setting the derivative of the total energy $S+U$ to zero, i.e.:

$$\frac{\partial(S+U)}{\partial a} = 2\gamma - \frac{\sigma_f^2}{E}\pi a = 0 \tag{4}$$

Because fracture is imminent when this condition is satisfied, the stress is written as σ_f.

$$\sigma_f = \sqrt{\frac{2E\gamma}{\pi a}} \tag{5}$$

Griffith's original work was devoted to brittle materials, specifically glass rods. When material exhibits more ductility, consideration of the surface energy alone fails to provide an accurate model for fracture (Åström et al. 2000). This drawback was later overcome, at least in part, independently by Irwin (1948) and Orowan (1949). They suggested that in a ductile material a considerable amount – in fact the vast majority – of the released strain energy was absorbed not by creating new surfaces but by energy dissipation due to plastic flow in the material near the crack tip (Hertzberg 1976). They suggested that catastrophic fracture occurs when the strain energy is released at a rate sufficient to satisfy the needs of all these energy "sinks" and denoted this critical strain energy release rate by the parameter G_C; the Griffith equation can then be rewritten in the following form:

$$\sigma_f = \sqrt{\frac{EG_C}{\pi a}} \qquad (6)$$

This expression describes, in a very succinct way, the relationship among three important aspects of the fracture process: the material, as evidenced in the critical strain energy release rate G_C; the stress level σ_f; and the size, a, of the flaw. In designing situation, one might choose the value of a based on the basis of the smallest crack that could be easily detected. Then for a given material with its associated value of G_C, the safe level of stress σ_f could be determined. The structure would then be sized so as to keep the working stress comfortably below this critical value (Barsom 1987).

It is important to realize that the critical crack length is an absolute number, which does not depend on the size of the structure containing the crack. Each time the crack grows further, by a small increment δa, an additional quantity of strain energy is released from the newly unloaded material near the crack (Landau and Lifshitz 1970; Landau and Lifshitz 1969; Landau and Lifszic 1958). Using simplistic picture of a triangular-shaped region that is at zero stress while the rest of the structure continues to feel the overall applied stress, it is possible to see in Fig. 3 that increasingly more energy is released due to the crack growth at position 2 than at position 1. This is why small objects tend to be stronger: they simply are not large enough to contain a critical crack length.

There are three elementary cracking modes depending on orientation of external force with respect to a fracture plane (Hertzberg 1976). Mode I is an opening mode (a tensile stress normal to the plane of the crack), Mode II is a sliding mode (a shear stress acting parallel to the plane of the crack and perpendicular to the crack front) and Mode III is a tearing mode (a shear stress acting parallel to both the plane of the crack and the crack front).
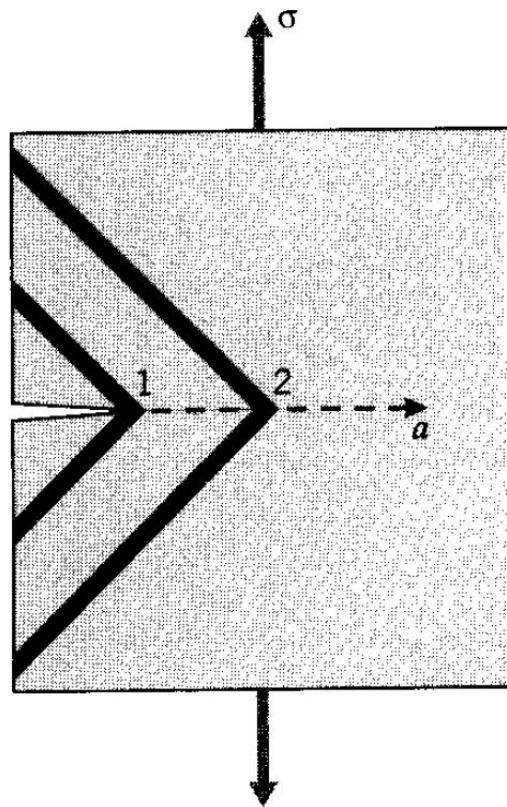
Fig. 3. Energy released during an increment of crack growth, for two different crack lengths (from Roylance 2001b).
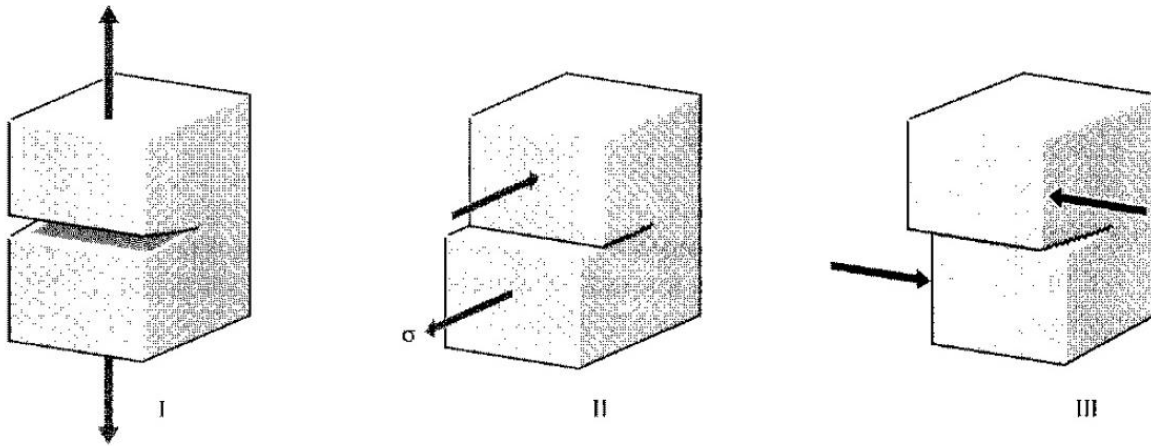
Fig. 4. Fracture modes (from Roylance 2001b).

These elementary modes are shown in Fig. 4. Mode I is a normal-opening mode, while modes II and III are shear sliding modes.

Computer simulations are flexible and useful tool in the field of fracture mechanics (Gordon 1976). With increasing power of computers, they offer increasingly more possibilities in analyzing fracturing process. The following chapter presents the overview of accessible numerical methods.

3.   THE DISCRETE ELEMENT METHOD

3.1 Numerical modelling of physical processes

Computer simulations of materials include two types of approaches – one of them assumes the continuity of the medium, and the other its discrete structure. Both have their advantages and disadvantages; thus, their applicability depends on the problem (Seweryn 2003).

3.1.1 Continuum methods for numerical simulations

One of the most common and popular numerical methods based on the continuum mechanics is the Finite Element Method (FEM), widely used in the engineering and in the science (Seweryn 2003; Munjiza 2004). The idea underlying FEM is to divide the considered continuous area into a finite number of subareas (finite elements) connected to each other at nodes and to approximate the solution in the element area using interpolation functions (shape functions) and values in nodes. Equations of the FEM are obtained from the formulation of an integral (global) problem, by using the variational principle or the residual (weighted) method (Rojek 2007). The advantages of the FEM method are: simplicity of discretization of complex shapes, the ease of determining boundary conditions and an adaptive coarsening and refinement of the mesh (Rojek 2007).

3.1.2 Discrete methods for numerical simulations

The FEM, despite its versatility, also has serious limitations. In this approach, the discrete nature of the granular medium and the relative displacements and rotation of particles inside the material are not considered. The FEM cannot be used for analysis of such phenomena as fragmentation, separation or mixing of materials. FEM is generally used for static or quasi-static problems in the field of small deformations (Balevičius et al. 2006; Rojek 2007). In the case of large strains or phenomena related to the flow of substances, the simulation often become unstable and, as a result, gives incorrect results.

Particle-based numerical methods offer an alternative approach which is being increasingly used for solving a variety of problems in engineering and applied science. Among the numerous particle-based methods, the Discrete Element Method (DEM) is one of the most popular (Rojek 2007). It is used for simulating granular and particulate flows, tracks particle motions and detects, and models collisions between particles and with their environment.

For purposes of this work, the DEM method is particularly interesting. In comparison to other numerical modeling approaches, DEM describes better the evolution of fractures in brittle materials (Rojek 2007). It has been widely used to simulate a single fracture at the local scale or at the field scale of fractured rock masses that contain a huge number of fractures (Cundall and Strack 1979; Cundall 1971, 1974, 1978). The main advantage of DEM is explicitly depicting the fracture geometry in relative details and considering the progressive degradation of material integrity during the degradation process (Abe et al. 2002; Abe and Mair 2005). More detailed insight into DEM is presented in the following subchapter.

3.2 Overview of Discrete Element Method

3.2.1 Basic assumptions

The DEM is a numerical method for simulating the dynamics of brittle-elastic or granular materials. Materials are represented as assemblies of particles, the so-called discrete elements, each of which may interact with neighbouring particles or other objects (such as external walls) through simplified force-displacement interactions. In DEM simulations, elements can move, rotate and interact with each other (Cundall and Strack 1979; Cundall 1971, 1974, 1978).

The elements are not subject to deformation; however, they can partially overlap each other. When two particles overlap, they start to interact. The magnitude of this interaction depends on the contact forces (Kazerani 2013) by the force-displacement relation. At the point of contact, compressive and tensile forces (if bonds are present), as well as tangent forces perpendicular to forces in the normal direction to the plane of contact appear and are transferred from one to another element.

The macroscopic behaviour of the material results from the movement and impact of individual particles. Thus, the macroscopic material response during the simulation depends on the microparameters of the elements and models of contacts between them. It is possible to distinguish several types of microparameters such as geometrical and physical microparameters, like shape, size, density and constitutive microparameters, like contact stiffness and attenuation. The simulation by DEM is a dynamic process, and the equilibrium occurs only when all contact (internal) forces are balanced. Each discrete element moves and rotates, and contacts between elements are detected in every step of the simulation (Fraige and Langston 2004; Rojek 2007).

One of the most important problems regarding DEM simulations is the proper selection of microparameters describing the elements and the interactions between them. There is a lack of close relationship between parameters describing interactions between simulation objects and those describing the sample as a whole. The selection of appropriate values of microparameters in order to obtain a macroscopic response of the system in accordance with the actual material is very difficult. Direct modelling, when the parameters are known in advance, is a rare situation (Fraige and Langston 2004; Rojek 2007; Freireich et al. 2015). The only solution to this problem is the iterative approach, so called inverse modelling, in which the selection of microparameters takes place on the basis of macroscopic parameters. A commonly used approach is to perform laboratory tests of a material sample to determine the macroscopic characteristics, and then numerically reflect selected tests and iteratively change selected microparameters until the expected response is achieved (Kruggel-Emden et al. 2008, 2011).

As mentioned above, particles building a sample can interact with one another and different types of contacts can be implemented (Johnson 1985; Kazerani et al. 2010). Namely, the contact

force can have two components: a normal component operating in the normal direction to the contact plane and a tangent component acting in the tangent plane. Three components describing properties of a contact can be described: contact stiffness (which provides a flexible relationship between the contact force and the relative displacement of elements), slip and separation conditions. It is possible to use different contact models depending on the needs of a given simulation, but in general, the two most commonly used models are the linear model and the Hertz-Mindlin model. In the linear model, the force and relative displacement are related linearly through constant contact stiffness. On the other hand, in the Hertz-Mindlin model, the force and relative displacement are related in a nonlinear way through variable contact stiffness.

Another important issue is generating the packing of elements (Cundall and Strack 1979; Cundall 1971, 1974, 1978). Two basic ways of packaging can be distinguished: dynamic and geometric algorithms. In a dynamic algorithm, a sample is created, for example, by a free fall of subsequent layers of elements. The advantage is that a predetermined size distribution of elements is obtained. In the case of a geometric model, elements are placed according to geometric relationships, often using pre-prepared grids (Rojek 2007).

The algorithm of the DEM (Fig. 5) can be divided into two main parts: the first one is related to the creation of a contact model and the calculation of forces acting on the elements, and in the second part, the second Newton's law of dynamics is applied to each element to calculate changes of position and velocity as a result of unbalanced action forces (Cundall and Strack 1979; Cundall 1971, 1974, 1978). Motion equations are solved separately for each particle. The solving algorithm is based on an explicit scheme of integration of motion equations. To maintain the numerical stability of the simulation, it is necessary to use small time steps so that the elements do not move too much in a time interval. This means that the selected time step value should be small enough to make the element movement small enough to affect only the immediate surroundings of the element.

The DEM method has one big disadvantage – it requires huge computing power. The heavy computational burden of the DEM relative to other numerical methods is often the single most limiting factor determining the quality and utility of simulation results. Nearly 40 years ago, when this method was developed, it was only a theoretical tool that could be used only for small and simplified scientific problems. Even now, modeling large-scale problems is still extremely time consuming and requires numerous simplifications. This is due to the fact that during simulation a huge amount of data are processed and collected (Cundall and Strack 1979; Cundall 1971, 1974, 1978).
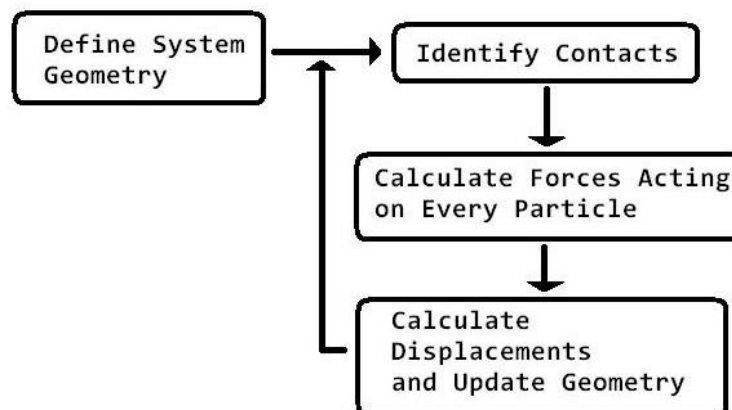

Fig. 5. The scheme of DEM simulation (O'Sullivan 2011).

Summarizing, the DEM method has extremely wide applications – it allows the description of dynamic and static phenomena related to materials. Using DEM, it is possible to model flows, separation, fragmentation, mixing, segregation, compression, stretching, cracking and many other phenomena (O'Sullivan 2011; O'Sullivan and Bray 2004). DEM also has a number of common applications, namely: ideal gas dynamics involving collisions between indivisible particles, gravitational acceleration of individual particles or bonded particles, sandpiles and landslides, hopper (or silo) flow, brittle failure of solids under uniaxial compression, and shear of granular media within an annular shear cell apparatus.

3.3 ESyS-Particle

In the presented research, an open-source DEM software has been used, named ESyS-Particle. The reasons behind this choice and the description of this software are presented below.

3.3.1 General description

ESyS-Particle is an open source software developed by the Earth Systems Science Computational Centre (ESSCC), the University of Queensland (Abe et al. 2014). It was designed to provide a basis to study the physics of rocks and the nonlinear dynamics of earthquakes, and to address the computational limits of existing DEM software. The major feature that distinguishes ESyS-Particle from other existing DEM codes is an explicit representation of particle orientations using unit quaternion, which allows a new way of decomposing the relative rotations between two rigid particles so that torques and forces accompanying such relative rotations can be uniquely determined.

The development of the ESyS-Particle software consists of a few major stages (Wang et al. 2012; Place et al. 2002; Potyondy and Cundall 2004). The first one was in the early 1990s, when the early version of Atomic Lattice Solid Model appeared. This was a 2D implementation of molecular dynamics principles written in Fortran. In the simplified model, there was interaction between particles only in the radial direction, and no intrinsic friction between existing particles. The next stage was extended to 3D, object-oriented approach LSMearth written in C++, with easily added or removed micro-physics. Further steps were as follows (Wang et al. 2012): parallel code using MPI; incorporation of intrinsic friction between particles; thermal effect; particle rotation and full rigidity between particles; Python script interface; theoretical analysis on particle parameter calibration; hydro-effect and Darcy flow; fully solid-fluid coupling based on DEM and Lattice Boltzman Method.

ESyS-Particle is written in C++ and designed for execution on parallel supercomputers, clusters or multi-core PCs (Abe et al. 2014). The simulation engine implements spatial domain decomposition through the Message Passing Interface (MPI) (Wang et al. 2012). A Verlet list neighbour search algorithm (Verlet 1967) is implemented for detecting neighbouring particles and a variety of particle interaction models are implemented. Particles building a sample may have up to three translational and three rotational degrees of freedom. An explicit first-order finite difference time integration scheme is employed. Provision is made for file storage of both the entire model state or specific field variables during simulations as the applications for the DEM are broad and varied (Abe et al. 2014).

ESyS-Particle provides an Application Programming Interface (API) allowing users to design simulations by scripts written in the Python programming language (Abe et al. 2014). For numerous applications, there is no need to modify the C++ simulation engine or recompile the software. Before running the code, the initial conditions, physical parameters, integration steps, types of particles (simple or rotational particles), types of loading walls, the contact properties (elastic, frictional, bonded contacts), artificial viscosity, ways of loading (force controlled or displacement controlled) and output fields are specified in the script. The Python API allows

users to specify the initial locations and properties of particles and walls, define the types of interactions acting on these objects, select the types and frequency of data output during simulations, and perform user-defined computations at regular intervals. Preprocessing includes a particle generation package, which can generate regular or random-sized particles. Aggregates or grains, gouges and faults can also be made. Postprocessing includes Povray and VTK visualization packages, which can visualize particles and fields (velocity, displacements).

The current version of ESyS-Particle stands out with two features. They were described by Weatherley et al. (2010) and Weatherley (2015) from the University of Queensland, one of the lead developers: "ESyS-Particle has two main advantages. The first is that its MPI parallel engine has been demonstrated to scale (weakly) to in excess 30 000 CPU cores and hence is definitely well suited for HPC DEM simulations. The second advantage is the BrittleBeamPrms particle-pair interactions that has been specifically designed for rock fracture and fragmentation simulations. This interactions correctly simulates Griffith crack propagation and, in particular, the formation of wing cracks. Credit to Dr. Yucang Wang for the mathematical formulation. Aside from the BrittleBeam interactions, ESyS-Particle provides a range of other interaction types."

3.3.2 Micromechanical model implemented in the ESyS-Particle

ESyS-Particle provides different types of interactions (bonds) between particles. In this research, two types of interactions were used. The first one "BrittleBeamPrms" (which has been designed for simulating brittle fracturing) was used in the simulations of uniaxial compression, Brazilian test and glacier calving. The second type of interaction called "NRotBondPrms" (designed for simulating material behaviour under tensional condition) was used here for uniaxial stretching simulations. In the following section are presented basics of the both models.

Bonded particles – *"BrittleBeamPrms"* type of bonds

The "BrittleBeamPrms" interaction model is actually the most advanced model the software uses and supports and involves all six degrees of freedom of each interacting particle (Li 2012). For each particle, three parameters x, y, z are used to represent the position of centre of the mass of the particle, and three other parameters ϕ, θ, ψ (such as Euler angles) to represent rotations around the centre of the mass.

Assuming small deformations, the relationship between interactions (forces or torques) and relative displacements between two bonded particles could be written in the linear form as:

$$
\begin{aligned}
F_r &= K_r \Delta r \\
F_{s1} &= K_{s1} \Delta s_1 \\
F_{s2} &= K_{s2} \Delta s_2 \\
M_t &= K_t \Delta \alpha_t \\
M_{b1} &= K_{b1} \Delta \alpha_{b1} \\
M_{b2} &= K_{b2} \Delta \alpha_{b2}
\end{aligned}
\tag{7}
$$

where: F represents forces, M – torques, K – rigidity constant, Δr and Δs – relative translational displacement, $\Delta \alpha$ – relative angular displacement. The meaning of the symbols r, s, t and b is as follows: r – radial component, s – shearing component, t – twisting component, b – bending component. In the isotropic case, $K_s = K_{s1} = K_{s2}$ and $K_b = K_{b1} = K_{b2}$. Therefore, only four rigidity parameters are required.

Particle motion can be decomposed into two completely independent parts, translational motion of the centre of the mass and rotation about the centre of the mass. The translational

motion of the center of the mass is governed by the Newtonian equations and integrated using a conventional Molecular Dynamic scheme (Mora et al. 1993, 1994).

$$\ddot{\vec{x}}(t) = \frac{\vec{F}(t)}{M} \tag{8}$$

where: $\boldsymbol{x}(t)$ and M are position of the particle and the particle mass, respectively. $\boldsymbol{F}(t)$ is the total force acting on the particle, which may include the spring forces by the neighbouring particles, the forces by the walls, viscous force and gravitational force. The above equation can be integrated using the velocity Verlet scheme (Rougier et al. 2004).

$$\vec{x}(t + \Delta t) = \vec{x}(t) + \vec{v}(t)\Delta t + \frac{1}{2}\vec{a}(t)\Delta t^2$$

$$\vec{v}(t + \Delta t) = \vec{v}(t) + \frac{\vec{a}(t) + \vec{a}(t + \Delta t)}{2}\Delta t \tag{9}$$

The standard implementation scheme of this algorithm is:
Step 1: Calculate $\vec{v}\left(t + \frac{1}{2}\Delta t\right) = \vec{v}(t) + \vec{v}(t)\Delta t + \frac{1}{2}\vec{a}(t)\Delta t$
Step 2: Calculate $\vec{x}(t + \Delta t) = \vec{x}(t) + \vec{v}\left(t + \frac{1}{2}\Delta t\right)\Delta t$
Step 3: Derive $\vec{a}(t + \Delta t)$ from the interaction potential using $\vec{x}(t + \Delta t)$
Step 4: Calculate $\vec{v}(t + \Delta t) = \vec{v}\left(t + \frac{1}{2}\Delta t\right) + \frac{1}{2}\vec{a}(t + \Delta t)\Delta t$

Eliminating the half-step velocity, this algorithm may be shortened to
Step 1: Calculate $\vec{x}(t + \Delta t) = \vec{x}(t) + \vec{v}(t)\Delta t + \frac{1}{2}\vec{a}(t)\Delta t^2$
Step 2: Derive $\vec{a}(t + \Delta t)$ from the interaction potential using $\vec{x}(t + \Delta t)$
Step 3: Calculate $\vec{v}(t + \Delta t) = \vec{v}(t) + \frac{1}{2}(\vec{a}(t) + \vec{a}(t + \Delta t))\Delta t$

This algorithm assumes that acceleration $\vec{a}(t + \Delta t)$ only depends on position $\vec{x}(t + \Delta t)$, and does not depend on velocity $\vec{v}(t + \Delta t)$.

The particle rotation depends on the total applied torque and its description within the used software usually involves two coordinate frames: one is fixed in space, called the space-fixed frame, in which Eq. (8) is applied, and the other is attached to the principal axis of the body rotation, referred to the body-fixed frame. The particle rotation is governed by the Euler's equations (in the body-fixed frame).

$$\tau_x^b = I_{xx}\dot{\omega}_x^b - \omega_y^b\omega_z^b(I_{yy} - I_{zz})$$
$$\tau_y^b = I_{yy}\dot{\omega}_y^b - \omega_z^b\omega_x^b(I_{zz} - I_{xx}) \tag{10}$$
$$\tau_z^b = I_{zz}\dot{\omega}_z^b - \omega_x^b\omega_y^b(I_{xx} - I_{yy})$$

where τ_x^b, τ_y^b, τ_z^b are the components of total torque $\boldsymbol{\tau}^b$ expressed in the body-fixed frame, ω_x^b, ω_y^b, ω_z^b are the components of angular velocity $\boldsymbol{\omega}^b$ measured in the body-fixed frame, and I_x^b, I_y^b, I_z^b are the three principal moments of inertia in the body-fixed frame in which the inertia tensor is diagonal. In case of 3D spheres, $I = I_{xx} = I_{yy} = I_{zz}$.

In this model, the unit quaternion $q = q_0 + q_1 i + q_2 j + q_3 k$ is used to explicitly describe the orientation of each particle. The physical meaning of a quaternion is that it represents a one-

step rotation around the vector $q_1\hat{\imath} + q_2\hat{\jmath} + q_3\hat{k}$ with a rotation angle of $2\boldsymbol{arccos}(q_0)$. A quaternion for each particle satisfies the following equation:

$$\dot{\boldsymbol{Q}} = \frac{1}{2}\boldsymbol{Q}_0(q)\varOmega \tag{11}$$

where

$$\dot{\boldsymbol{Q}} = \begin{pmatrix} \dot{q}_0 \\ \dot{q}_1 \\ \dot{q}_2 \\ \dot{q}_3 \end{pmatrix}, \quad \boldsymbol{Q}_0(q) = \begin{pmatrix} q_0 & -q_1 & -q_2 & -q_3 \\ q_1 & q_0 & -q_3 & q_2 \\ q_2 & q_3 & q_0 & -q_1 \\ q_3 & -q_2 & q_1 & q_0 \end{pmatrix}, \quad \varOmega = \begin{pmatrix} 0 \\ \omega_x^b \\ \omega_y^b \\ \omega_z^b \end{pmatrix}. \tag{12}$$

Equations (10) and (11) can be solved according to the algorithm outlined below. The quaternion $q(t + dt)$ is obtained at the next time step using:

$$q(t + dt) = q(t) + dt\dot{q}(t + dt/2) + O(dt^3) \tag{13}$$

Hence, the quaternion derivative at mid-step $\dot{q}\,(t + dt/2)$ is required. Equation (11) indicates that $q(t + dt)$ and $\omega^b(t + dt)$ are also required, where the former can be easily calculated using:

$$q(t + dt/2) = q(t) + \dot{q}(t)dt/2 \tag{14}$$

where $\dot{q}(t)$ again is obtained from Eq. (11) and $\boldsymbol{\omega}^b(t + dt)$ can be calculated using

$$\boldsymbol{\omega}^b(t) = \boldsymbol{\omega}^b(t - dt/2) + I^{-1}\boldsymbol{\tau}^b(t)dt \tag{15}$$

and $\boldsymbol{\omega}^b(t + dt/2)$ can be obtained, using

$$\boldsymbol{\omega}^b(t + dt/2) = \boldsymbol{\omega}^b(t - dt/2) + I^{-1}\tau^b(t)dt \tag{16}$$

The algorithm for calculating particle motion, presented in this section, was developed by Wang et al. (2012). To avoid the buildup errors during temporal evolution, it is a common practice to renormalize quaternions at frequent intervals (usually done every step). Thus, the algorithm of time evolution is as follows:

Step 1: calculate torque $\tau^b(t)$ at time t
Step 2: using the stored $\omega\left(t - \frac{dt}{2}\right)$, update $\omega(t)$ using Eq. (8)
Step 3: gain $\dot{q}(t)$ using (5)
Step 4: using the stored $\omega\left(t - \frac{dt}{2}\right)$, calculate $\omega\left(t + \frac{dt}{2}\right)$ using Eq. (9)
Step 5: compute $q\left(t + \frac{dt}{2}\right)$ using Eq. (7)
Step 6: evaluate $\dot{q}\left(t + \frac{dt}{2}\right)$ using Eq. (5)
Step 7: calculate $q(t + dt)$ using Eq. (6)
Step 8: renormalize the quaternion $q(t + dt)$

Given the position and orientation for each particle, the calculation of interactions between neighbouring ones due to relative motion involves a unique decomposition of the relative motions in such a way that interactions can be uniquely calculated. Decomposition of the relative translation can be found in Wang et al. (2004), decomposition of relative rotation in Wang (2009).

Particles can have bonds between each other. The key issue is a threshold criterion of bonds breaking. A bond is permitted to break under purely extension if the force exceeds certain threshold F_{r0}, but it does not break under compression. Similarly, a bond breaks under pure shear load when shear force reaches F_{s0}, or under pure twisting load if twisting torque exceeds M_{t0}, or under pure bending load if bending torque exceeds value M_{b0}. When all the interactions exist at the same time, the following criterion is used to judge whether or not a bond is going to break

$$\frac{F_r}{F_{r0}} + \frac{|F_s|}{F_{s0}} + \frac{|M_t|}{M_{t0}} + \frac{|M_b|}{M_{b0}} \geq 1 \qquad (17)$$

where $\overrightarrow{F_s} = \overrightarrow{F_{s1}} + \overrightarrow{F_{s2}}, \overrightarrow{M_b} = \overrightarrow{M_{b1}} + \overrightarrow{M_{b2}}$. F_r is set positive under extension and negative under compression, therefore the effects of normal force on breakage of the bond has been taken into account. Input parameters of the presented model include the particle mass m, radius R, rigidity parameters K_r, K_s, K_b and K_t and fracture parameters F_{r0}, F_{s0}, M_{t0} and M_{b0}.

Presented rotational interactions, created by Wang (2009), are generalised 3D rotational bonded interactions, which requires specification of eight model parameters, namely: *normalK* (elastic stiffness for compression/tension), *shearK* (elastic stiffness for shear), *bendingK* (elastic stiffness for bending), *torsionK* (elastic stiffness for torsion), *normalBreakForce* (maximum tensile/compressive force), *shearBreakForce* (maximum shear force), *bendingBreakForce* (maximum bending moment), *torsionBreakForce* (maximum torsion moment). The first four model parameters determine the elastic properties of the interaction between two particles. The second four parameters determine when a bond will break via a generalised Mohr-Coloumb failure criterion (Weatherley et al. 2010).

This formulation (Wang 2009) is quite general in the sense that one can explore quite a broad (eight-dimensional) parameter space for the relative impact of normal/shear/bending/ torsion components of deformation between two particles. However, this formulation is mostly applicable for models built of spheres of equal size. For models comprised of spheres with a range of sizes (the usual case for ESyS-Particle simulations) the general formulation (based on elastic stiffnesses) is not scale-invariant (Weatherley et al. 2010), it means, this formulation does change if scales of length, energy, or other variables, are multiplied by a certain factor.

Interactions that use a constant elastic stiffness (e.g. *normalK* in Newtons/metre) to bind particles of differing radii, result in a macroscopic particle-size dependency of the elastic properties (e.g. Young's modulus) of the particle assembly. By contrast, a linear elastic material does not have such a size-dependency (elastic properties are scale-invariant).

The particle-size dependency can be eliminated from DEM models by assigning a constant bond Young's modulus between bonded particles, and then assigning the elastic stiffness (such as *normalK*) as a function of the constant bond modulus and geometrical properties that depend on the radii of the two bonded particles (Weatherley et al. 2010). More specifically, it is necessary to assume that bonded interaction between the two particles has a particular shape (i.e. an equilibrium length, L and a cross-sectional area, A). For *BrittleBeamPrms* interaction model, it is assumed that the interaction between two particles is a cylindrical beam whose equilibrium length is $L = R_1 + R_2$ and cross-sectional area is $A = \frac{\pi(R_1+R_2)^2}{4}$, i.e. the effective radius of the cylindrical beam is the arithmetic mean of the two particle radii R_1, R_2.

Particle-pair interactions can include both translational and rotational degrees of freedom. Two bonded particles may undergo normal and shear forces, as well as bending and twisting moments (Fig. 6). Bonds designed to import such forces and moments are known as cementitious bonds (in ESyS-Particle, *BrittleBeamPrms* interaction). Unlike the non-rotational equivalent, rotational frictional interactions impart a torque to both particles, causing the particles to rotate relative to each other when in frictional contact. The physical interpretation of rotational bonds is that two particles are connected to one another with a cylindrical elastic beam whose radius is the mean of the radii of the bonded particles and whose equilibrium length is the sum of the radii of those particles. The elasticity of bonds is determined by a microscopic Young's modulus (*youngsModulus* parameter) and a microscopic Poisson's ratio (*poissonsRatio* parameter). It should be emphasized that the macroscopic elastic properties of an assembly of bonded particles do not necessarily match the microscopic elastic properties of the bonds themselves (Weatherley et al. 2010).

Applying these assumptions and linear elastic beam theory, permits to define the four elastic stiffness parameters as functions of two elastic properties - the bond Young's modulus and bond Poisson's ratio (Weatherley et al. 2010). These beam interactions break according to a Mohr-Coulomb failure criterion (governed by two model parameters: *cohesive strength C* and *internal friction angle ψ* – Eq. (1), so, the four breakage forces can be computed as functions of *C* and *ψ*. A bond will fail (or break) if the shear stress within the bond exceeds its shear strength ($τ$) given by:

$$\tau = C + \sigma_N \tan\left(\varphi_f\right) \tag{18}$$

where *C* is the cohesive strength of the bond for zero normal stress (σ_N) and φ_f is the internal angle of friction of the bond. The *cohesion* and *tanAngle* parameters, respectively, define the cohesive strength and friction angle of bonds.


```
BrittleBeamPrms(
    name="pp_bonds",
    youngsModulus=100000.0,
    poissonsRatio=0.25,
    cohesion=100.0,
    tanAngle=1.0,
    tag=1
)
)
```
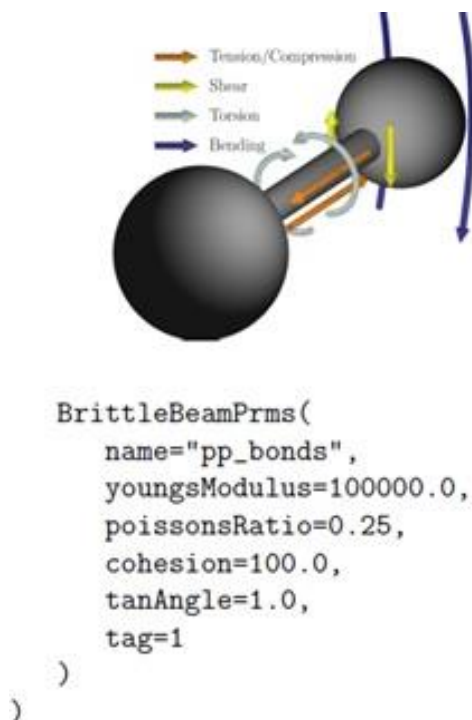
Fig. 6. Forces and moments between particles bonded through rotational elastic-brittle bonds (from Abe et al. 2014).

In this model the near-neighbourhood particles interact with each other with repulsive/cohesive radial forces and nonradial "shearing" ones. If interacting particles separate by fixed distance (in terms of percentage of their radii) the interacting bond is broken and interaction is reset to zero. Breaking of shearing forces is based on the Coulomb-Mohr criterion (Abe et al. 2014). Under these assumptions a specimen represents a medium which for small external loading behaves as an ideal elastic body. For larger loads, when some inter-particles bonds break and particles can significantly move away from their initial location the material exhibits some plasticity. Finally, in large stress concentration regions, the particles can separate due to a significant stress redistribution when interaction bonds break (a similar effect is observed in soft-clamp Fiber Bundle Model; Hansen et al. 2015) which finally leads to an initiation and development of cracks. This way, with this simple setup the behaviour of a variety of solid materials can be simulated.

Consequently, only four model parameters must be specified for BrittleBeamPrms. They are as follows: *youngsModulus* (Young's modulus of bonds – stress units), *poissonsRatio* (Poisson's ratio for bonds – dimensionless), *cohesion* (Mohr-Coulomb cohesion factor – stress units), *tanAngle* – (tangent of angle of internal friction for Mohr-Coulomb failure criterion – dimensionless). Two parameters are set by default: *meanR_scaling* (determines how the effective radius of bonds between two particles is calculated), *truncated* (factor by which to truncate tensile strength).

The last argument (*truncated*) is a number between 0.0 and 1.0 defining the factor by which to reduce the tensile strength. If *truncated* = 1.0, the Mohr-Coulomb envelope is not truncated under tension. It *truncated* = 0.0, bonds have no tensile strength. The *meanR_scaling* argument determines how the effective radius of bonds between two particles is calculated. By default, the effective bond radius is $R_b = \frac{R_1 + R_2}{2}$, where R_1, R_2 are the radii of the two particles to be bonded together.

The bond parameters used by the code to influence and control bonded particle motion are K_n, K_s, K_b, K_t. These are calculated from E (Young's modulus) and v (Poisson's ratio), as well as the length and cross-sectional area of the bond. These formulae may be written in this way:

$$K_n = \frac{EA}{L}$$
$$K_s = \frac{GA}{L}$$
$$K_b = \frac{EI}{L}$$
$$K_t = \frac{GJ}{L}$$

(19)

where

$G = \frac{E}{2*(1+v)}$ is the shear modulus,

$A = \pi R_b{}^2$ is the cross-sectional area of the cylindrical beam (with radius R_b)

$L = R_1 + R_2$ is the equilibrium length of the beam

$I = \frac{\pi R_b{}^4}{4}$ is the cross-sectional moment of inertia, and

$J = \frac{\pi R_b{}^4}{2}$ is the polar moment of inertia.

Some general rules between mechanical properties of bonds and macroscopic properties of the material are as follows: macroscopic Young's modulus is proportional to microscopic bond modulus and weakly depends on bond Poisson's ratio; peak strength (unconfined compressive strength) is proportional to bond cohesion and weakly depends on bond internal friction angle; the elastic properties of bonds do not impact macroscopic strength and the breakage properties of bonds do not impact macroscopic elasticity; the constants of proportionality depend on choice of particle packing parameters, particularly the ratio of R_{min}:R_{max} (Weatherley et al. 2010).

Bonded particles – *NRotBondPrms* type of bonds

NRotBondPrms is one of the simplest particle interactions incorporated to ESyS-Particle. According to this model, neighbouring particles are initially connected via a linear elastic spring whose spring constant is given by the value of *normalK* parameter if parameter called *scaling==False*. If *scaling==True*, *normalK* defines a Young's modulus for the spring and its spring constant is determined based upon the radii (*R*1, *R*2) of the two interacting particles.

Parameter *breakDistance* determines when the bonded interaction "breaks" under tension. When the separation of the two particles exceeds *breakDistance*(R1+R2)*, the bonded interaction is destroyed (Weatherley et al. 2010).

NRotBondPrms(

name = "sphereBonds",

normalK = 10000.0,

breakDistance = 0.5,

tag = 1,

scaling = True

)

Fig. 7. Parameters of *NRotBondPrms* type of bonds.

Interaction *NRotBondPrms* contains five parameters (Fig. 7): a bond *tag* specifying which bonded particles will undergo this interaction, a unique *name* for the interaction group, the elastic stiffness (*normalK*) of the bonds, a Boolean variable (*scaling*) to specify whether to scale the stiffness with particle size, and a *breakDistance* specifying the separation distance that must be exceeded in order to break a bond between two particles. When the distance between a pair of bonded particles exceeds *breakDistance*, the bond is broken and finally removed. The particles thereafter interact according to the interactions specified for unbonded particle-pairs *(*Abe et al. 2014).

Unbonded particles

Particles can undergo bonded interactions or frictional (unbonded) interactions but not both. This is achieved by specifying an exclusion between the two interaction groups. Because a broken bond represents a fracture surface, it is appropriate to specify frictional interactions between unbonded particles. In the ESyS-Particle, the function responsible for this has four parameters: *youngsModulus*, *poissonsRatio*, *dynamicMu*, *staticMu*.

Rotational frictional interactions are defined by a microscopic Young's modulus (*youngs Modulus*) and Poisson's ratio (*poissonsRatio*) and two microscopic coefficients of friction. Typically the Young's modulus and Poisson's ratio for *FrictionPrms* interactions are set equal to their *BrittleBeamPrms* counterparts. The *staticMu* coefficient of friction is applied when two particles are in static frictional contact, i.e., prior to the first time the frictional sliding criterion is met. Thereafter the *dynamicMu* coefficient of friction is applied. By setting *dynamicMu* < *staticMu*, it is possible to simulate the physical observation that the frictional force required to maintain sliding is smaller than the force necessary to initiate sliding. The friction coefficients (*dynamicMu* and *staticMu*) are dimensionless and for real materials, are typically in the range 0.2-0.8. Parameter *dynamicMu* should be less than or equal to *staticMu* (Abe et al. 2014).

Other important parameters – viscosity, damping, numerical stability and time step

Any acoustic emissions generated during fracturing should dissipate rapidly compared with the duration of the simulation. To achieve these conditions, it is necessary to incorporate two body forces designed to attenuate translational (called *LinDampingPrms*) and rotational oscillations *(RotDampingPrms)*. The purpose of this artificial viscosity is to attenuate kinetic energy of particles and avoid unphysical buildup of kinetic energy. The viscosity coefficients are chosen to be small so that damping has little effect on the elastic response of the simulated rock sample but sufficient to attenuate unwanted oscillations.

In this software, these two damping forces have two basic parameters: *viscosity* and *maxIterations*. The *viscosity* coefficient can take any value. It is in units of [1/time]. In order to compute the net force on a particle in the presence of such a viscous term, it is necessary to use a convergence loop controlled by the second parameter (Weatherley et al. 2010). Such iteration is necessary to compute the correct viscous forces. Parameter *maxIterations* determines the maximum number of iterations of this convergence loop. In most cases the loop converges very quickly (<10 iterations).

The *LinDampingPrms* and *RotDampingPrms* interactions are "body forces" that act on particles individually (Weatherley et al. 2010). They are proportional to the current velocity of the particle. For linear damping, a bulk viscosity force acting on particle *i* is:

$$F_i = -1 * visc * v_i * m_i \tag{20}$$

where $visc$ is the coefficient of viscosity (supplied as an argument to *LinDampingPrms*), v is the current velocity of the particle. A similar damping moment calculation (proportional to the angular velocity of the particle) is applied when using *RotDamping*.

Another key parameter of the ESyS-Particle simulations is the size of the time step, responsible for numerical stability of the simulation (Weatherley et al. 2010). The following formula is usually used to verify the numerical stability by checking the Courant condition during the time step increment:

$$\Delta t \leq \sqrt{\frac{\frac{4}{3}\pi\rho * R_{\min}^3}{E_{\max} * R_{\max}}} \tag{21}$$

where: ρ is the particle density, $E_{\max} * R_{\max}$ is the the maximum stiffness approximately equal to Young's modulus (E) multiplied by the maximum radius of the particles $R_{\max}$, and $\frac{4}{3}\pi\rho * R_{\min}^3$ is the minimum particle mass.

The DEM and its open source implementation, ESyS-Particle, are specially designed for simulating brittle fracturing. In the next two chapters are presented results of efforts in simulating fracturing processes. The first chapter of these two shows simulations of geomechanical laboratory tests of materials. The second one is devoted to glacier calving.

4. DISCRETE ELEMENT SIMULATIONS OF SOLID MATERIALS UNDER EXTERNAL LOAD

4.1 Introduction

The numerical analysis of cracking processes requires an appropriate numerical technique (Gordon 1976; Rong et al. 2013). Classical engineering approach to the problem has its roots in the continuum mechanics and is based mainly on the FEM (Di Renzo and Di Maio 2004; Egholm 2007). This technique allows simulations of both elastic and large deformation processes; therefore, it is very popular in the engineering applications. However, a final effect of cracking – fragmentation of an object at hand can hardly be described by this approach in a numerically efficient way as it requires a solution of a problem of nontrivial evolving in time boundary conditions (Cook et al. 1964).

For this reason, this research was focused on the DEM, which by definition implies the "molecular" construction of the matter (Williams et al. 1985; Wolff et al. 2013). Consequence of that is that DEM includes an evolution of boundary conditions treating them as yet another particle-particle interaction. The DEM is widely recognized as an efficient method for granular

and brittle material modelling (Bidgoli et al. 2013; Kwapinska et al. 2006). The material model built using discrete elements can be treated as physically compatible with the structure that characterizes the real one. For example, it can consider the existing discontinuities and other defects of solid bodies. The unique feature of this approach is that it explicitly considers the individual particles in the material and their interactions. DEM presents an alternative to the typical approach adopted when simulating the mechanical behavior of materials, which uses a continuum mechanics framework (Fakhimi and Gharahbagh 2011; Lambert and Coll 2014; Lisjak and Grasselli 2014). In a continuum model material is assumed to behave as a continuous and the relative movements and rotations of the particles inside the material are not considered. Sophisticated constitutive models (i.e., equations related to the stress and strain in a material) are then needed to capture the complexity of the material behaviour that arises owing to the particulate nature of the material (Carmona et al. 2014, Collins 1981).

Fig. 8. Uniaxial compression – laboratory experiment.

It is well known that not all aspects of the fracturing process can be analysed by experimental methods (Nouguier-Lehon et al. 2003; Pál et al. 2014; Zhao 2017). Thus, computer modelling can be a complement solution, since it provides additional useful tool for studying the microscopic aspects of fracturing – especially, particles interactions, rotations and movements (Klejment and Dębski 2017, 2018; Klejment et al. 2016, 2018a, b). In this chapter are presented the results of DEM application to three different material tests: uniaxial compression, Brazilian Test and uniaxial stretching. Such tests are extremely important in many areas of science and engineering and provide an effective way to characterize a material's response to loading (Gordon 1976). Presented DEM models are still only the simplifications and do not capture all aspects related to a real material's structure. However, numerical simulations have a lot to offer and in the future can partially replace expensive and arduous laboratory experiments (Figs. 8 and 9).

Fig. 9.   Brazilian Test – laboratory experiment.

4.2 Uniaxial compression

Simulations of the uniaxial compression were the first part of the research.

4.2.1 Motivation and outline

Uniaxial compression is a common laboratory test in which cylindrical sample is compressed from the top and the bottom (Fig. 10) and it provides a simple and effective way to characterize a material's response to loading (Rojek 2007; Jing et al. 2013). Specimens from drilled cores are prepared by cutting them to the specified dimensions. The recommended ratio of height/ diameter of the specimens is between 2 and 3 (Rojek 2007; International Society for Rock Mechanics, Commission on Standardization of Laboratory and Field Tests (1978). By subjecting a sample to a controlled tensile or compressive displacement along a single axis, the change in dimensions and resulting load can be recorded to calculate the stress-strain profile. From the obtained curve, elastic and plastic material properties can then be determined. Two material features measured in this way are especially important: the Young's modulus and the Poisson's ratio (Rojek 2007). The movement of plates is typically held at a constant rate, and the displacement and resulting load are recorded (Sochor 1998). The following relations are used to calculate various quantities in this type of experiment.

Strain can be calculated as follows:

$$\varepsilon_e = \frac{\Delta L}{L_0} \tag{22}$$

where ΔL is the measured displacement and L_0 is initial sample length along a single axis. Stress is defined as follows:

$$\sigma_e = \frac{P}{A_0} \tag{23}$$

where P is the applied load and A_0 is the initial cross-sectional area of the sample normal to the loading direction.

The material subjected to loading initially behaves in a linear elastic manner, i.e., stress and strain are linearly related, and on unloading, the deformation is recoverable. The slope of the strain-stress curve within the linear elastic regime is equal to Young's modulus, which is the ratio of the stress to axial strain (Sochor 1998):

$$E = \frac{\sigma_e}{\varepsilon_e} \tag{24}$$

Poisson's ratio can be calculated as a value of Young's modulus divided by the ratio between the stress to diametric strain.

The DEM is very popular in studying uniaxial compression. There are two reasons behind this fact. The first one is the importance of uniaxial compression itself, which is very popular and very basic laboratory test. The second one is that modelling of uniaxial compression is an initial part of the most of the DEM simulations, because this is a primary way to calibrate parameters of modelled material (Strawley et al. 1965).

Numerous papers about the DEM modelling of the uniaxial compression have been published in recent years. Duan et al. (2016) proposed a new numerical approach to model the mechanical behaviors of inherently anisotropic rocks in which the rock matrix is represented as a bonded particle model, and the intrinsic anisotropy is imposed by replacing any parallel bonds dipping within a certain angle range with smooth-joint contacts. The radial strain control method for uniaxial compression tests was introduced by Shimizu et al. (2010) in the distinct
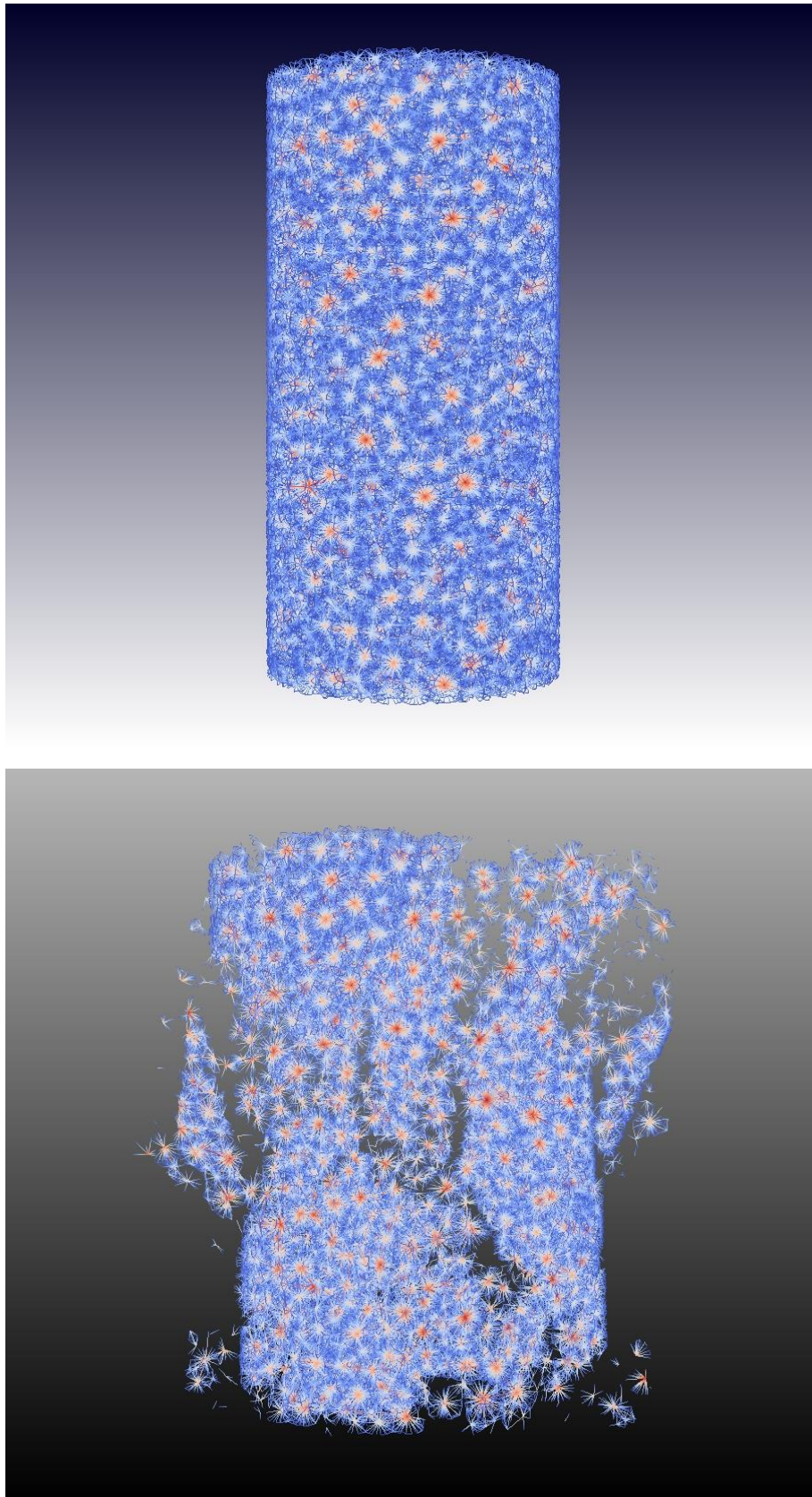
Fig. 10. An exemplary sample before (top) and after (bottom) uniaxial compression. View of bonds. Colour stands for the radius of the particle that is set in this place – red means the largest particles, blue – the smallest particles.

element method codes and the Class II behavior of rocks was simulated. Wiącek et al. (2012) numerically showed that an increase in the particle aspect ratio strongly affected the mechanical response of a specimen under uniaxial compression. Nitka (Nitka and Tejchman 2015) has focused on the DEM modelling of the behaviour of plain concrete under uniaxial compression and uniaxial tension using the discrete element method. Vesga et al. (2008) used DEM to study how cracks propagate in a continuum material (clay) subjected to a uniaxial compressive stress. The DEM proved to be a very successful approach for the visualization of secondary crack formations and their propagation in the simulated samples. Yang et al. (2014) adopted the particle flow code (PFC2D) to carry out a discrete element modelling for the fracture coalescence behavior of red sandstone specimens containing two unparallel fissures under uniaxial compression. Ergenzinger et al. (2011) investigated a bonded-particle model using extended Discrete Element Method with respect to failure of strong rock under uniaxial compression. Scholtes and Donze (2012) discovered that instabilities in rock structures involve coupled mechanisms related to both deformations along existing discontinuities and brittle fracture of intact rocks.

In comparison to the abovementioned studies, this research is focused mainly on the changes in microscopic structure of the material during applying compressive force. Such analysis involves relationship between the microscopic parameters of bonds and macroscopic parameters of the whole sample, especially different aspects related to rotational and linear movements of material's particles.

4.2.2 Simulation settings

In this subsection the details of performed uniaxial compression simulations are described. A model of the cylindrical sample was constructed of approximately $100\,000$ particles with radii from 0.3 to 3.0 mm. Two types of samples were prepared: with density of 940 kg/m^3 corresponding to an ice-like material (Riikilä 2017), and with density of 2260 kg/m^3 corresponding to a sandstone-like material (Hertzberg 1976). Particles inside the samples were connected by bonds created to simulate behaviour of brittle materials called in ESyS-Particle the *BrittleBeamPrms* as described in Section 3.3.2. Modeled cylindrical sample was compressed by two walls, both moving with a constant velocity 0.5 mm/s (an exemplary view of the sample before and after the fracture is shown in Fig. 10). Although this rate is significantly higher than that typically used in laboratory uniaxial compression experiments, it is sufficiently small to maintain quasi-static conditions in the simulations. The initial acceleration of the walls from zero to the desired speed (during the first $50\,000$ timesteps) also helps to ensure thta the sample is loaded quasi-statically without generating an acoustic waves. The full set of used parameters is shown in Table 1.

4.2.3 Simulation results

Presented simulations were mainly focused on the relationship between four microscopic parameters of bonds and two macroscopic parameters of the sample. These microscopic parameters were, namely, Young's modulus, Poisson ratio, cohesion, and friction angle of bonds, as described in Section 3.3.2. The considered macroscopic parameters of the samples were Young's modulus (stiffness of the sample in the linear elasticity regime) and Poisson's ratio. The full list of used parameters and obtained results are shown in Table 2 and 4.

Young's modulus and Poisson's ratio were calculated according to the scheme presented in the diagram from Fig. 11. Young's modulus is calculated as a slope of the curve axial stress – axial strain, for an initial (linear) part of the strain-stress curve. Poisson's ratio is calculated as the ratio between the value of Young's modulus and slope of axial stress – diametral strain curve (also linear part).

Table 1

Uniaxial compression simulations – parameter settings

Particles size	from 0.3 to 3.0 mm
Time step	5.0e-06s
Time steps	2 000 000
Particles density	940 kg/m^3 or 2240 kg/m^3
Type of bonds	
Name: *BrittleBeamPrms*	Parameters: name = "pp_bonds", youngsModulus = in according with Table 2 and Table 4, poissonsRatio = in according with Table 2 and Table 4, cohesion = in according with Table 2 and Table 4, tanAngle = in according with Table 2 and Table 4, tag=0
Unbonded particles	
Name: *FrictionPrms*	Parameters: name ="friction", youngsModulus = the same as youngsModulus in *Brittle BeamPrms* interaction, poissonsRatio = the same as poissonsRatio in *Brittle BeamPrms* interaction, dynamicMu = 0.4, staticMu = 0.6
Elastic repulsion with the walls	
Name: *NRotElasticWallPrms*	Parameters: normalK = the same as youngsModulus in *BrittleBeamPrms* interaction
Translational viscous damping	
Name: *LinDampingPrms*	Parameters: viscosity = 0.002, maxIterations = 50
Name: *RotDampingPrms*	Parameters: viscosity = 0.002, maxIterations = 50
Compressing rate	
Velocity	0.5 mm/s
rampTime	50 000 time steps

The analysis of the obtained results concerned three main groups of issues: dependencies between microscopic and macroscopic parameters of samples with different densities; changes of components of potential energy of bonds during the fragmentation process; changes of components of kinetic energy of particles during the fragmentation process.
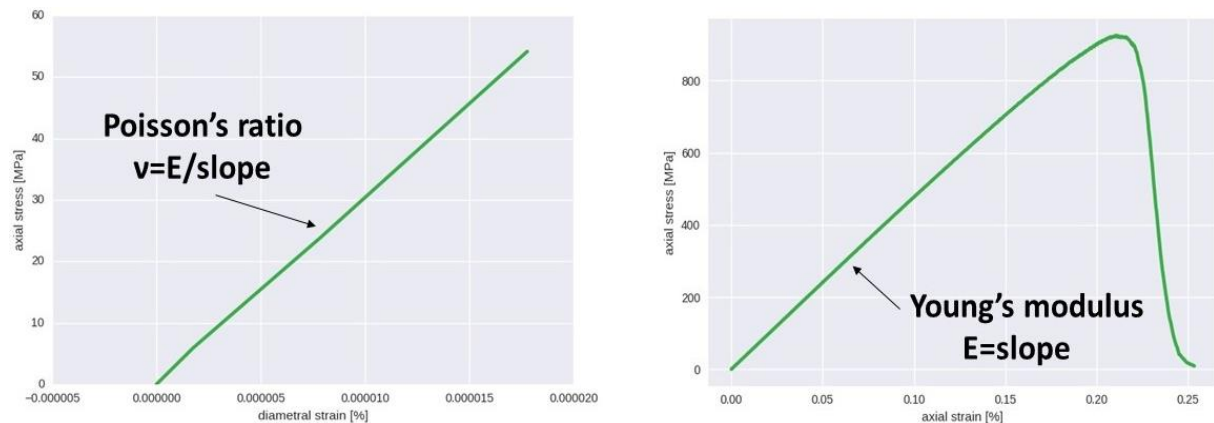
Fig. 11. Macroscopic parameters of the sample (Young's modulus and Poisson's ratio) were calculated from the stress-strain curves. Young's modulus as a slope of axial stress – axial strain curve, and Poisson's ratio as a Young's modulus divided by the slope of the axial stress – diametral strain curve.

Microscopic and macroscopic parameters of samples

Table 2

The relationship between microscopic and macroscopic parameters of a sample of density 940 kg/m^3 under uniaxial compression

	Microscopic parameters				Macroscopic parameters	
	Young's modulus [MPa]	Poisson ratio [dimensionless]	Cohesion [dimensionless]	Tangent of the friction angle	Young's modulus [GPa]	Poisson ratio [dimensionless]
Uniaxial Test 1	1.00E+03	0.25	10 000	1.0	5.21E+00	0.13
Uniaxial Test 2	1.00E+03	0.25	1000	1.0	5.21E+00	0.13
Uniaxial Test 3	1.00E+03	0.34	100	1.0	5.12E+00	0.14
Uniaxial Test 4	1.00E+03	0.34	1000	1.0	5.12E+00	0.14
Uniaxial Test 5	1.00E+04	0.25	1	1.0	4.67E+01	0.14
Uniaxial Test 6	1.00E+04	0.34	100	1.0	4.85E+01	0.16
Uniaxial Test 7	1.00E+05	0.50	100	1.0	4.63E+02	0.17
Uniaxial Test 8	1.00E+05	0.15	10 000	0.5	5.07E+02	0.14
Uniaxial Test 9	1.00E+05	0.50	10 000	1.0	4.66E+02	0.17
Uniaxial Test 10	1.00E+05	0.40	10 000	0.0	4.75E+02	0.17
Uniaxial Test 11	1.00E+05	0.25	100	0.0	4.92E+02	0.15
Uniaxial Test 12	1.00E+05	0.25	100 000	1.0	4.83E+02	0.13
Uniaxial Test 13	1.00E+05	0.25	1000	1.0	4.92E+02	0.15
Uniaxial Test 14	1.00E+05	0.34	100	1.0	4.82E+02	0.16
Uniaxial Test 15	1.00E+05	0.34	1000	1.0	4.80E+02	0.16
Uniaxial Test 16	1.00E+05	0.25	100	1.0	4.92E+02	0.15
Uniaxial Test 17	1.00E+05	0.20	100	1.0	5.00E+02	0.15

Table 2 presents the dependence between four microscopic parameters and two macroscopic parameters of the whole sample. The study of this relationships was carried out for a whole series of parameters selected in a possibly wide and cross-sectional way (however, with the greatest emphasis on microscopic Young's modulus and cohesion).

One of the most visible results is a clear relationship between the microscopic Young's modulus and the macroscopic Young's modulus. A higher value of the first parameter corresponds to a higher value of the second parameter. Another conclusions came from the observation of a parameter such as cohesion. When keeping the remaining three parameters fixed, the change in cohesion does not affect macroscopic parameters Young's modulus and Poisson's ratio (cases Uniaxial Test 1 and Uniaxial Test 2, as well as Uniaxial Test 3 and Uniaxial Test 4) or an effect is minor (Uniaxial Test 12 and Uniaxial Test 13 or Uniaxial Test 14 and Uniaxial

Table 3

Samples that broke apart under considered loading selected from the samples from Table 2.
On the horizontal axis, axial strain [%]; on the vertical axis, axial stress [MPa]

Uniaxial Test 1   Uniaxial Test 5   Uniaxial Test 6

Uniaxial Test 7   Uniaxial Test 11   Uniaxial Test 13

Uniaxial Test 14   Uniaxial Test 15   Uniaxial Test 16

Uniaxial Test 17
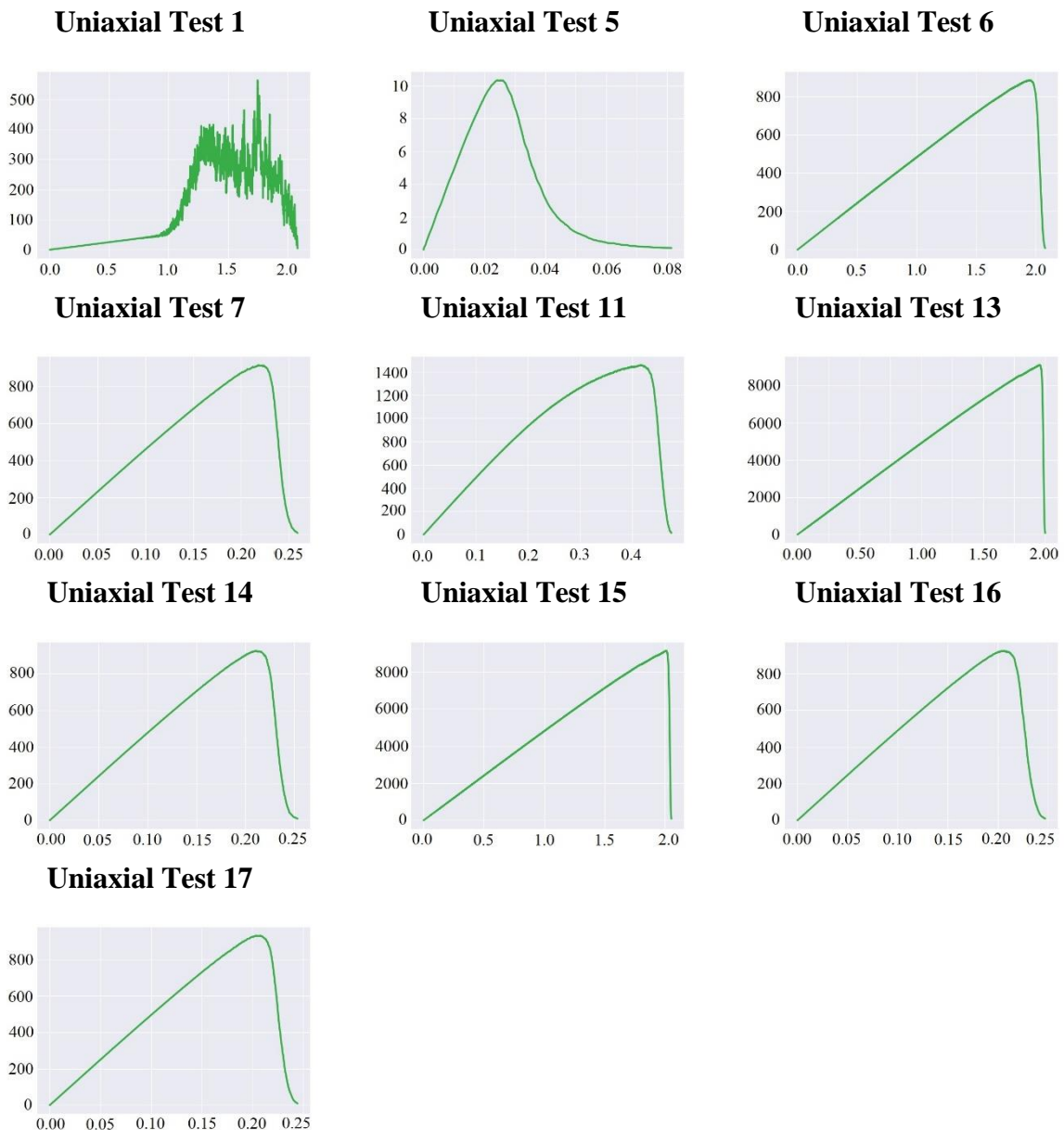
Test 15). The last two pairs of results suggest that the higher microscopic cohesion corresponds to the lower macroscopic Young's modulus. However, it was observed that the cohesion parameter is crucial for defining the sample "brittleness" and breaking moment. From the tests Uniaxial Test 13 and Uniaxial Test 15, and also from three tests Uniaxial Tests, 14, 16, and 17, it can be concluded that the lower microscopic Poisson's ratio translates into a higher macroscopic Young's modulus.

For assumed simulation parameters (Table 2), not every sample broke apart under considered loading. Sometimes this was due to the characteristics of the sample itself, and sometimes due to the limited simulation time. The samples for which breaking occurred are shown in Table 3, together with their stress-strain curves. The specific noisy shape of the curve for the Uniaxial Test 1 is most likely due to numerical dispersion.
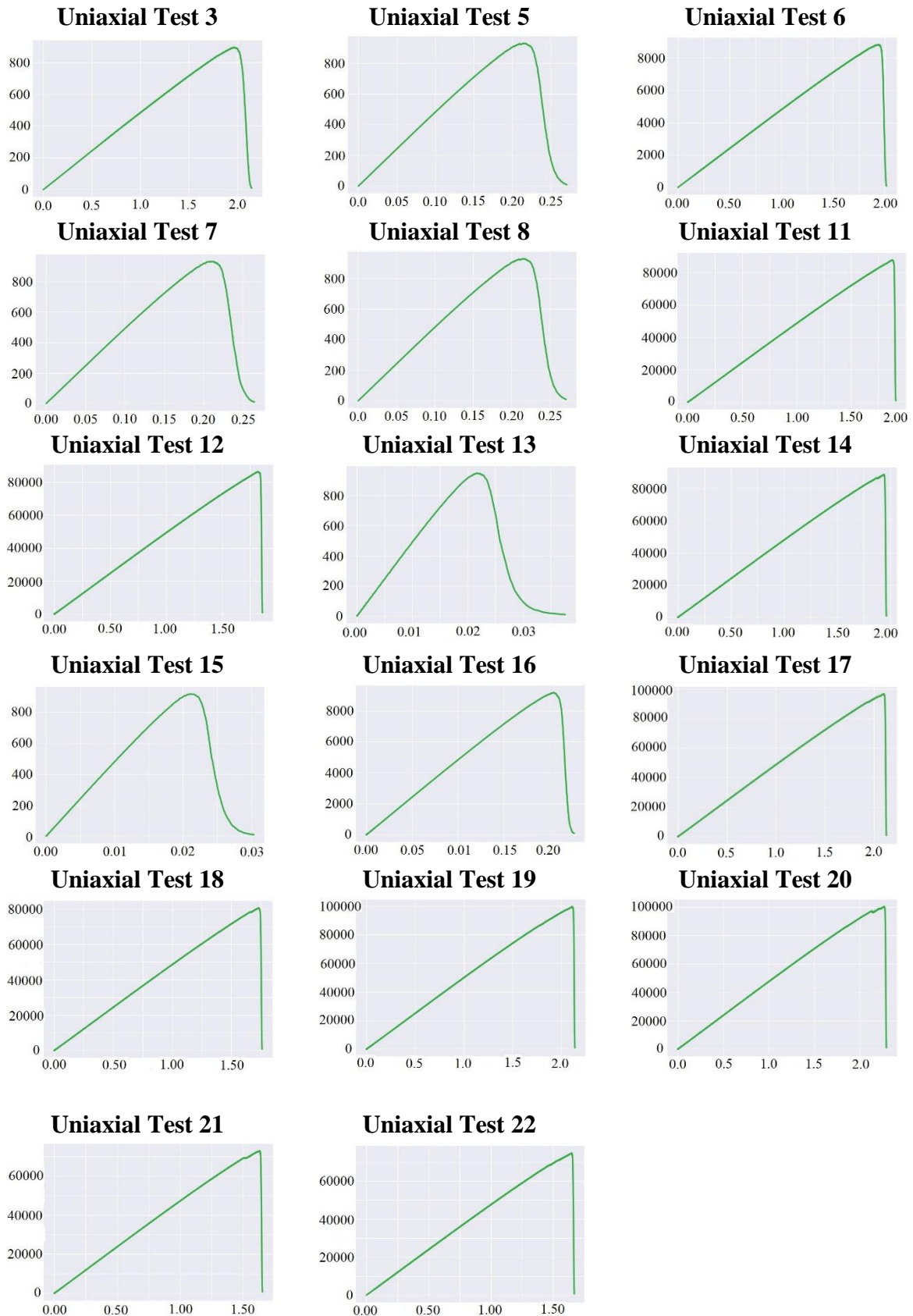
Table 4

The relationship between microscopic and macroscopic parameters of a sample of density 2260 kg/m^3 under uniaxial compression

	Microscopic parameters				Macroscopic parameters	
	Young's modulus [MPa]	Poisson ratio [dimensionless]	Cohesion [dimensionless]	Tangent of the friction angle	Young's modulus [GPa]	Poisson ratio [dimensionless]
Uniaxial Test 1	1.00E+03	0.25	1000	1.0	5.42E+00	0.14
Uniaxial Test 2	1.00E+03	0.34	100	1.0	5.29E+00	0.14
Uniaxial Test 3	1.00E+04	0.34	100	1.0	4.91E+01	0.15
Uniaxial Test 4	1.00E+05	0.25	10 000	1.0	4.93E+02	0.15
Uniaxial Test 5	1.00E+05	0.34	100	1.0	4.82E+02	0.16
Uniaxial Test 6	1.00E+05	0.34	1000	1.0	4.81E+02	0.16
Uniaxial Test 7	1.00E+05	0.25	100	1.0	4.93E+02	0.15
Uniaxial Test 8	1.00E+05	0.20	100	1.0	5.01E+02	0.15
Uniaxial Test 9	1.00E+06	0.30	10 000	1.0	1.30E+02	0.06
Uniaxial Test 10	1.00E+06	0.25	100	1.0	1.28E+03	0.16
Uniaxial Test 11	1.00E+06	0.25	10 000	1.0	4.84E+03	0.24
Uniaxial Test 12	1.00E+06	0.20	10 000	1.0	4.95E+03	0.15
Uniaxial Test 13	1.00E+06	0.25	100	1.0	4.90E+03	0.14
Uniaxial Test 14	1.00E+06	0.30	10 000	1.0	4.88E+03	0.06
Uniaxial Test 15	1.00E+06	0.25	100	1.0	4.51E+03	0.15
Uniaxial Test 16	1.00E+06	0.25	1000	1.0	4.84E+03	0.16
Uniaxial Test 17	1.00E+06	0.25	10 000	0.8	4.73E+03	0.10
Uniaxial Test 18	1.00E+06	0.25	10 000	1.2	4.75E+03	0.19
Uniaxial Test 19	1.00E+06	0.15	10 000	0.7	4.95E+03	0.16
Uniaxial Test 20	1.00E+06	0.35	10 000	0.7	4.71E+03	-0.01
Uniaxial Test 21	1.00E+06	0.35	10 000	1.5	4.61E+03	0.15
Uniaxial Test 22	1.00E+06	0.35	10 000	1.5	4.77E+03	0.15

Table 5

Samples that broke apart under considered loading selected from the samples from Table 4.
On the horizontal axis, axial strain [%]; on the vertical axis, axial stress [MPa]

Analogously to the abovementioned results regarding the material with a density of 940 km/m³, the results for material with a density of 2260 km/m³ were considered in a similar manner. First, Table 4 presents the relationship between microscopic and macroscopic parameters. The results, segregated according the microscopic Young's modulus, have been given names from Uniaxial Test 1 to Uniaxial Test 22. Again the microscopic Young's modulus is a key parameter affecting macroscopic Young's modulus and this is a very strong influence. The lower value of the microscopic Poisson's ratio corresponds to the higher macroscopic Young's modulus (e.g., Uniaxial Test 1 and 2). The effect of microscopic parameters on macroscopic Poisson's ratio is definitely less visible. From the Uniaxial Test 17 – Uniaxial Test 22 (for which the microscopic value of Young's modulus and cohesion was fixed, while microscopic Poisson's ratio and tangent of the friction angle were changed) it can be seen that microscopic Poisson's ratio and tangent of the friction angle have a significant effect on macroscopic Poisson's ratio, while the effect on macroscopic Young's modulus is much weaker.

The stress-strain curves for the samples that broke apart are presented in Table 5.

In the next step, the obtained results were used for analysis of potential energy of bonds and kinetic energy of particles. The dependence between particular components of potential energy (bending, normal, shearing and twisting) and kinetic energy (linear and rotational) was considered. These calculations were carried out only for the samples that broke apart during simulated compression, for both densities, 940 kg/m³ and 2260 kg/m³. Such samples are listed in Table 3 and 5 together with their stress-strain curves, and detailed data on microscopic and macroscopic parameters of simulated materials can be found in Table 2 and 4. Samples for which compression simulations ended only in the linear part of the stress-strain curve, without breaking, were not taken into account in these considerations.

Importantly, it was observed that the breaking process occurred for different samples in different ways. Therefore, to obtain comparable results, the following procedure was implemented:

- ❑ Step 1: in equal, regular time intervals the sum of all types of rotational energy of all bonds and all types of kinetic energy of all particles was recorded.
- ❑ Step 2: for each sample the breaking range was extracted (Fig. 12). In this range, values obtained in the first step were added to each other and then averaged over a time intervals mentioned in the first step.
- ❑ Step 3: the percentage share was calculated of particular types of different kinetic and potential energies in average kinetic and potential energies, which values were calculated in the previous step.
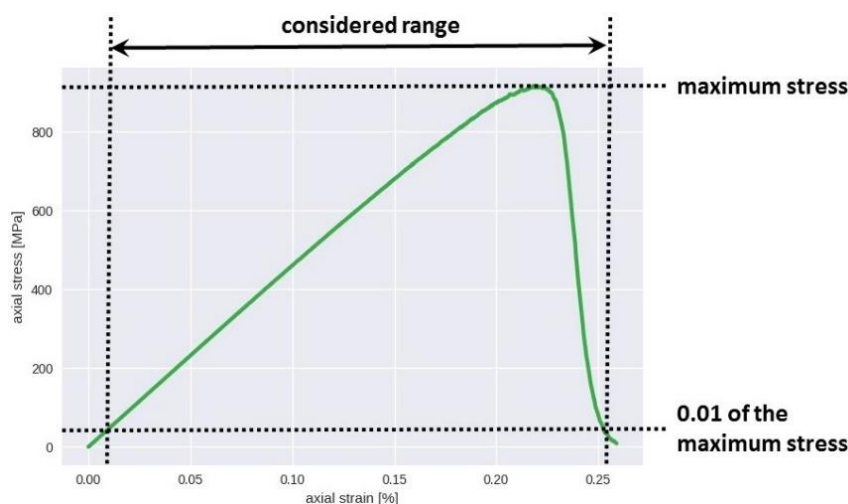
Fig. 12. The breaking range considered during calculating the components of potential energy of bonds and the components of kinetic energy of particles.

Components of potential energy of bonds

At the beginning, the potential energies of bonds were considered. The bending energy, normal energy, shearing energy and twisting energy as a percentage of the total average potential energy of all bonds are shown as columns at Fig. 13 respectively. The exact numerical values are listed also in Table 6.

Fig. 13. Visual representation of potential energies of the bonds (bending, normal, shearing and twisting energy) as a percentage of total potential energy for the data from Table 6.

Table 6

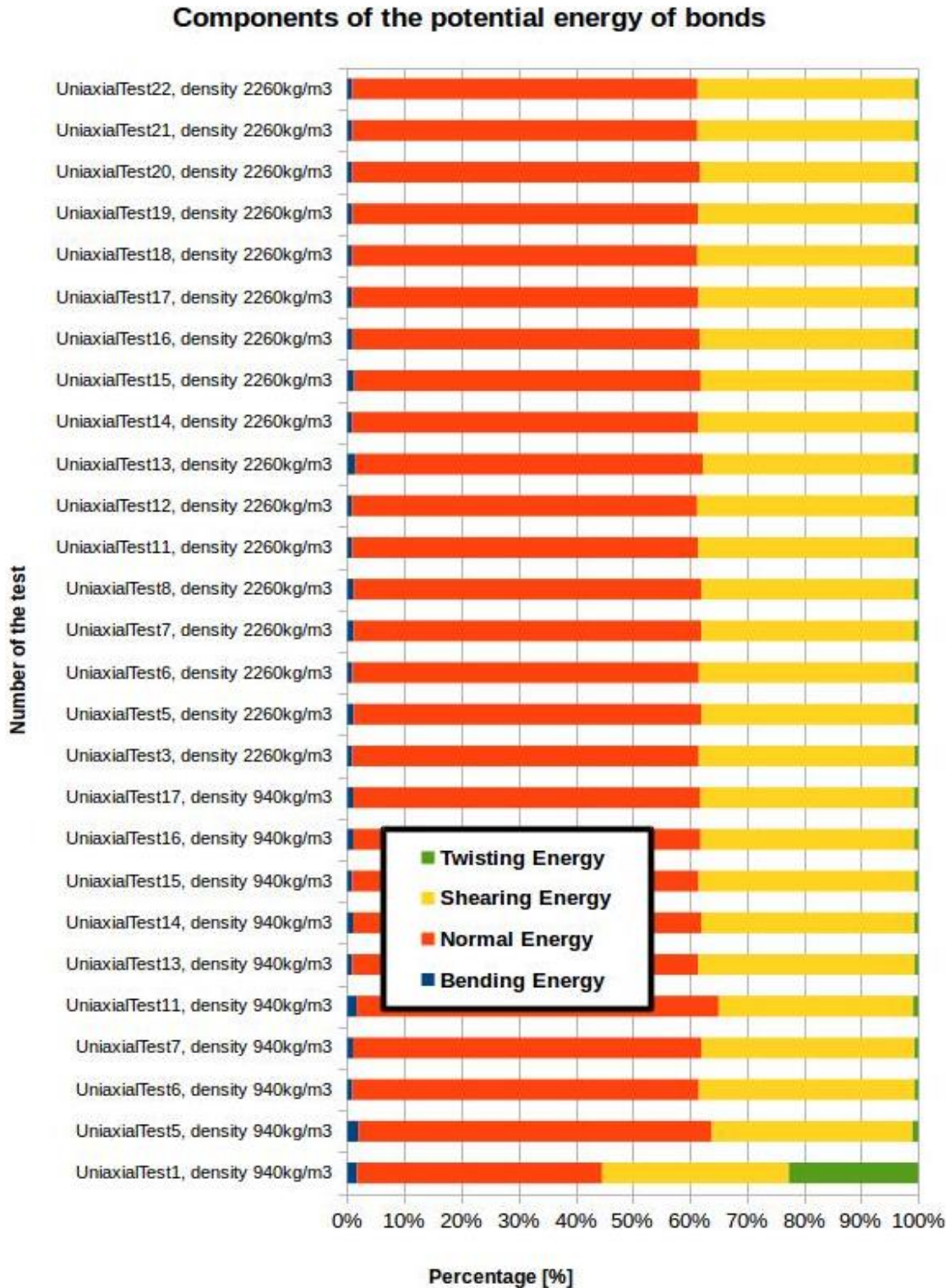Potential energies of the bonds (bending, normal, shearing and twisting energy) as a percentage of total potential energy for the samples from Table 3 and 5. Average value per time step

	Components of the potential energy of bonds			
	Bending energy	Normal energy	Shearing energy	Twisting energy
Uniaxial Test 1, density 940 kg/m^3	1.70%	42.96%	32.69%	22.66%
Uniaxial Test 5, density 940 kg/m^3	1.94%	61.91%	35.17%	0.98%
Uniaxial Test 6, density 940 kg/m^3	0.86%	60.75%	37.79%	0.60%
Uniaxial Test 7, density 940 kg/m^3	1.02%	61.08%	37.27%	0.63%
Uniaxial Test 11, density 940 kg/m^3	1.64%	63.44%	34.05%	0.87%
Uniaxial Test 13, density 940 kg/m^3	0.84%	60.60%	37.94%	0.62%
Uniaxial Test 14, density 940 kg/m^3	1.03%	60.95%	37.35%	0.67%
Uniaxial Test 15, density 940 kg/m^3	0.84%	60.73%	37.84%	0.59%
Uniaxial Test 16, density 940 kg/m^3	1.04%	60.86%	37.40%	0.70%
Uniaxial Test 17, density 940 kg/m^3	1.04%	60.84%	37.41%	0.71%
Uniaxial Test 3, density 2260 kg/m^3	0.88%	60.72%	37.80%	0.60%
Uniaxial Test 5, density 2260 kg/m^3	1.10%	60.97%	37.80%	0.60%
Uniaxial Test 6, density 2260 kg/m^3	0.84%	60.77%	37.80%	0.59%
Uniaxial Test 7, density 2260 kg/m^3	1.10%	60.94%	37.25%	0.71%
Uniaxial Test 8, density 2260 kg/m^3	1.10%	60.93%	37.25%	0.73%
Uniaxial Test 11, density 2260 kg/m^3	0.82%	60.60%	37.97%	0.61%
Uniaxial Test 12, density 2260 kg/m^3	0.82%	60.50%	38.05%	0.63%
Uniaxial Test 13, density 2260 kg/m^3	1.35%	60.94%	36.89%	0.82%
Uniaxial Test 14, density 2260 kg/m^3	0.83%	60.68%	37.90%	0.59%
Uniaxial Test 15, density 2260 kg/m^3	1.20%	60.72%	37.29%	0.78%
Uniaxial Test 16, density 2260 kg/m^3	0.94%	60.83%	37.57%	0.67%
Uniaxial Test 17, density 2260 kg/m^3	0.84%	60.70%	37.84%	0.62%
Uniaxial Test 18, density 2260 kg/m^3	0.82%	60.51%	38.06%	0.61%
Uniaxial Test 19, density 2260 kg/m^3	0.85%	60.57%	37.92%	0.66%
Uniaxial Test 20, density 2260 kg/m^3	0.84%	60.98%	37.59%	0.59%
Uniaxial Test 21, density 2260 kg/m^3	0.83%	60.50%	38.08%	0.59%
Uniaxial Test 22, density 2260 kg/m^3	0.84%	60.52%	38.06%	0.58%

Interestingly, almost identical results and dependencies were obtained for all samples, regardless of their microscopic and macroscopic parameters. The only one exception was the Uniaxial Test 1 for a density 940 km/m^3. This exception fully reflected the results from Table 3 and 5. Only Uniaxial Test 1 is distinguished by a different shape of the stress-strain curve. Probably, this was the result of numerical dispersion, as mentioned earlier. The remaining samples had similar stress-strain diagrams, in which the stress linearly increases in the function of

the strain, followed by one main break and then a rapid decrease in stress to zero. The main difference lies in different stress and strains values corresponding to breaking. As mentioned above, virtually all samples showed identical relationships between different types of potential energies. Normal potential energy was fixed around 61%, shearing potential energy around 38%. The smallest share belonged to bending potential energy and twisting potential energy, both of these energies were generally less than 1%. Detailed values are presented in Table 6.

Table 7

Kinetic energies of the bonds (linear and rotational) as a percentage of total kinetic energy for the samples from Table 3 and 5. Average value per time step

Components of the kinetic energy of particles		
	Linear kinetic energy	Rotational kinetic energy
Uniaxial Test 1, density 940 kg/m^3	3.77%	96.23%
Uniaxial Test 5, density 940 kg/m^3	96.00%	4.00%
Uniaxial Test 6, density 940 kg/m^3	90.58%	9.42%
Uniaxial Test 7, density 940 kg/m^3	92.69%	7.04%
Uniaxial Test 11, density 940 kg/m^3	87.91%	12.09%
Uniaxial Test 13, density 940 kg/m^3	84.39%	15.61%
Uniaxial Test 14, density 940 kg/m^3	93.03%	6.97%
Uniaxial Test 15, density 940 kg/m^3	84.51%	15.49%
Uniaxial Test 16, density 940 kg/m^3	92.90%	7.10%
Uniaxial Test 17, density 940 kg/m^3	92.90%	7.10%
Uniaxial Test 3, density 2260 kg/m^3	92.38%	7.62%
Uniaxial Test 5, density 2260 kg/m^3	94.00%	6.00%
Uniaxial Test 6, density 2260 kg/m^3	87.63%	12.37%
Uniaxial Test 7, density 2260 kg/m^3	94.00%	6.00%
Uniaxial Test 8, density 2260 kg/m^3	94.28%	5.72%
Uniaxial Test 11, density 2260 kg/m^3	80.28%	19.72%
Uniaxial Test 12, density 2260 kg/m^3	78.50%	21.50%
Uniaxial Test 13, density 2260 kg/m^3	94.68%	5.32%
Uniaxial Test 14, density 2260 kg/m^3	80.28%	19.72%
Uniaxial Test 15, density 2260 kg/m^3	91.07%	8.93%
Uniaxial Test 16, density 2260 kg/m^3	89.22%	10.78%
Uniaxial Test 17, density 2260 kg/m^3	78.14%	21.86%
Uniaxial Test 18, density 2260 kg/m^3	79.05%	20.95%
Uniaxial Test 19, density 2260 kg/m^3	75.73%	24.27%
Uniaxial Test 20, density 2260 kg/m^3	78.26%	21.74%
Uniaxial Test 21, density 2260 kg/m^3	80.99%	19.01%
Uniaxial Test 22, density 2260 kg/m^3	81.31%	18.69%

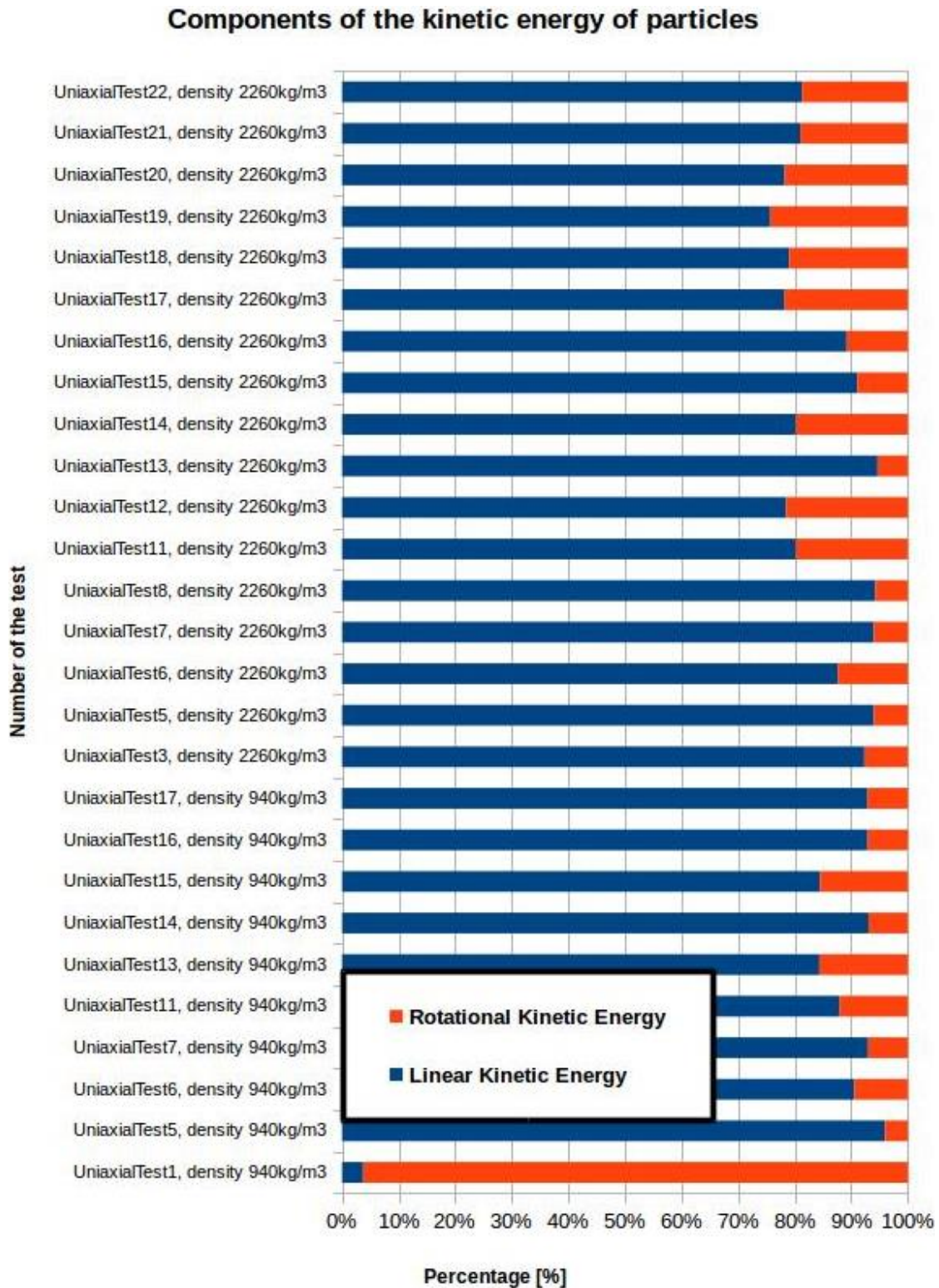## Components of the kinetic energy of particles

Fig. 14. Visual representation of kinetic energies of the particles (linear and rotational energy) as a percentage of the total kinetic energy for the data from Table 7.

The results presented above are average values for all existing bonds. For the results extracted in this way, a certain regularity was found between different types of potential energy of bonds. Normal potential energy of bonds, associated with approaching or moving away of particles, is the largest part, the second one the most important potential energy is this connected

with shearing between particles. All movements connected with bending or twisting make a very small contribution. Especially interesting is the fact that the ratio between particular potential energies of bonds is always constant, despite very various microscopic and macroscopic parameters of considered samples.

Components of kinetic energy of particles

Further, the kinetic energies of particles were taken into account. The individual columns present the linear kinetic energy and the rotational kinetic energy as a percentage of total kinetic energy of all particles (Fig. 14, Table 7).

The relationship between kinetic energies of particles is not as obvious at first glance as in the case of energy of potential bonds. Again, Uniaxial Test 1 stands out, for which 96% is rotational kinetic energy. For the remaining samples, linear kinetic energy prevails, ranging from about 80% to 96%. It is possible to distinguish between two groups of results for which the ratio between linear kinetic energy and rotational kinetic energy is about 80% to 20% or about 94% to 6%. A comparison with Table 2 and Table 4 leads to the conclusion that for the higher proportion of rotational kinetic energy during the breaking process is responsible the microscopic parameter – cohesion.

4.2.4 Conclusions

The simulations of uniaxial compression provided results in three groups of issues: dependencies between microscopic (Young's modulus, Poisson's ratio, cohesion, tangent of the friction angle) and macroscopic (Young's modulus, Poisson's ratio) parameters of samples with densities of 940 kg/m^3 and 2260 kg/m^3, average potential energy of bonds, average kinetic energy of particles.

One of the clearest relationships between microscopic and macroscopic parameters was this between the microscopic Young's modulus and the macroscopic Young's modulus. A higher value of the first parameter corresponds to a higher value of the second parameter. Another conclusions came from the observation of a parameter such as cohesion. When keeping the remaining three microscopic parameters fixed, the change in cohesion does not affect macroscopic parameters, Young's modulus and Poisson's ratio, or affects it slightly. In some cases, the higher microscopic cohesion corresponds to the lower macroscopic Young's modulus. On the other hand, the cohesion parameter is crucial for defining the sample brittleness and breaking moment. It can be also concluded that the lower microscopic Poisson's ratio translates into a higher macroscopic Young's modulus. Additionally, microscopic Poisson's ratio and tangent of the friction affect significantly macroscopic Poisson's ratio, while much smaller macroscopic Young's modulus.

Interesting results were obtained while considering potential energies of bonds. The average percentage contribution of different potential energies of bonds to the average overall potential energy of bonds during the breaking process was always constant. Normal energy was fixed around 61%, shearing energy around 38%. The smallest share belonged to bending energy and twisting energy, both of these energies being generally less than 1%. The relationship between kinetic energies of particles was not as clear as in the case of potential energy of bonds. Linear kinetic energy prevailed, ranging from about 80% to 96%. It was possible to distinguish between two groups of results for which the ratio between linear kinetic energy and rotational kinetic energy was about 80% to 20% or about 94% to 6%. A comparison with microscopic parameters of bonds led to the conclusion that the microscopic parameter – cohesion – was mainly responsible for this difference.

4.3 Brazilian test

Simulations of the Brazilian test were the second part of the research. These results were presented at V International Conference on Particle-based Methods in Hannover, September 2017 (Klejment and Dębski 2017).

4.3.1 Motivation and outline

The tensile strength of solid materials is one of the most important parameter that describes the behaviour of materials under mechanical load and thus its knowledge is of great practical importance (Lavrov and Vervoort 2002). However, the direct measurement of tensile strength, especially for brittle materials is quite difficult and thus only limited results are available. To cope with this situation, Akazawa (1943) has proposed an indirect method of estimation of the tensile strength known as the Brazilian test (Fig. 15). The method relies on diametrically loading of a disk-like sample of a brittle material until it splits apart due to induced tensile stress as shown in Fig. 16. The justification of the method comes from the theory of elasticity which predicts that for an ideal homogeneous elastic cylinder of radius R and length L subjected to a diametrically linear loading P the stress inside the body reads (Hobs 1964; Zhang and Eckert 2005):

$$\sigma_x = \frac{P}{\pi RL} - \frac{2P}{\pi L}\left(\frac{x^2(R-y)}{[x^2+(R-y)^2]^2} + \frac{x^2(R+y)}{[x^2+(R+y)^2]^2}\right)$$

$$\sigma_y = -\frac{P}{\pi RL} - \frac{2P}{\pi L}\left(\frac{(R-y)^3}{[x^2+(R-y)^2]^2} + \frac{x(R+y)^2}{[x^2+(R+y)^2]^2}\right) \quad (25)$$

$$\tau_{xy} = \frac{2P}{\pi L}\left(\frac{x(R-y)^2}{[x^2+(R-y)^2]^2} - \frac{x(R+y)^2}{[x^2+(R+y)^2]^2}\right)$$

where x and y refer to coordinates, as shown in Fig. 16. As it follows from above, at the loading plane ($x = 0$) the σ_x and σ_y are normal stresses ($\sigma_{xy} = 0$) perpendicular and parallel to the loading plane, respectively, and the tensile stress σ_x is constant and reads
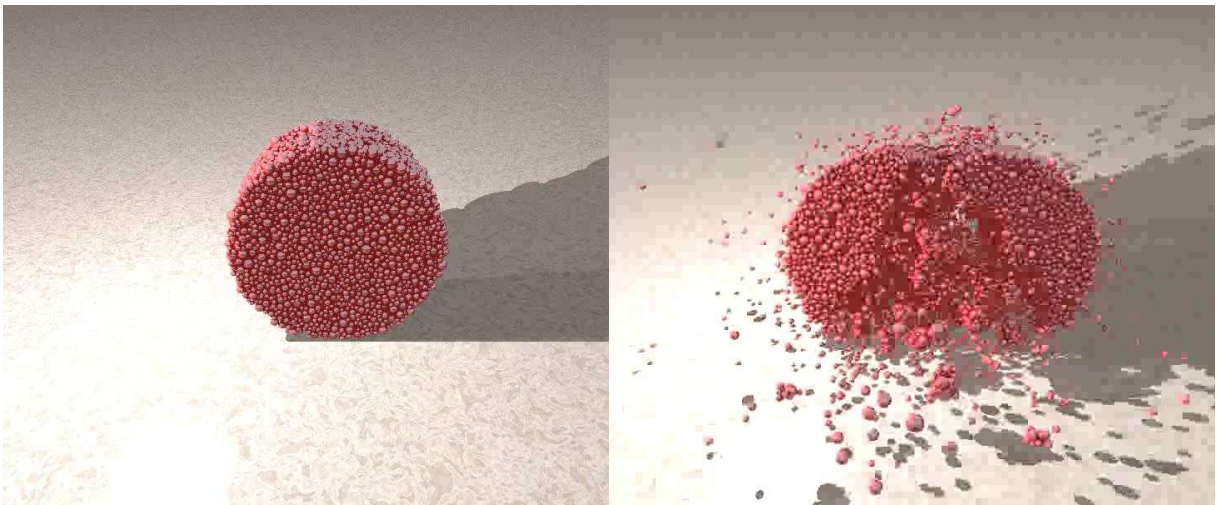

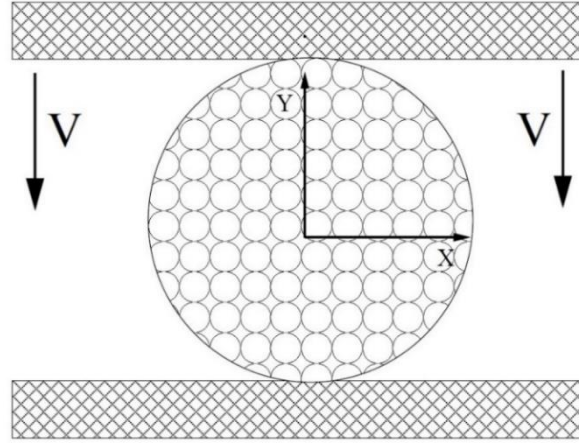Fig. 15. A sample before (left) and after experiment (right).

Fig. 16. Sketch of the simulation setup used in numerical simulations. The horizontal loading plates are assumed to be perfectly rigid. The lower plate is fixed while the upper one moves downward with constant velocity V providing the diameter loading of the disk (after Klejment and Dębski 2017).

$$\sigma_T = \frac{P}{\pi RL} \tag{26}$$

while the compressional stress σ_y increases from $3\sigma_x$ at the centre of the disk to infinity at the loading point.

These formulas have been extended to a more realistic laboratory situations considering loading over a finite, bended surface, and nonhomogeneity and anisotropy of the material, to name a few extensions. The usefulness and simplicity of the Brazilian test follow directly from Eq. (26), which predicts that tensile is proportional to the loading. Thus, assuming that splitting of the samples occurs when tensile stress reaches the material tensile strength, it can easily be estimated from Eq. (26) by recording the loading force when the sample is crushed (Sator and Hietala 2010; Sator et al. 2008).

The Brazilian test method has gained considerable popularity not only because of the simplicity of its application but also due to more fundamental concepts concerning mechanisms of creation and development of the tensile fractures under simple initial and boundary conditions (Behera et al. 2005). However, it has also received considerable criticism because of the lack of robustness and proximity. These disadvantages are due to the fact that the Brazilian test results show a systematic overestimation of the tensile toughness with respect to values obtained in direct measurements. Thus, there is a considerable ongoing discussion on reasons of these discrepancies.

There remains an open question on the dynamics of nucleation and the development of the main tensile and secondary cracks resulting in a final breaking apart of the specimen. The classical theory predicts the creation of such crack in the centre of the sample where the compressing stress is the smallest. After nucleation, the crack is expected to propagate along the loading plane outwards. However, in many experiments the crack was observed to nucleate not in centre but close to the sample surface (Hudson et al. 1972). Wing-type and secondary cracks were also observed (Cai 2013). Another open question is which criterion should be used for the estimation of the tensile strength. The most popular approach is based on the stress criterion according to which the material breaking occurs when tensile stress reaches the critical value and Eq. (26) is then directly used to calculate the tensile strength. However, this is fully an arbitrary choice. Another, physically justified strain criterion was proposed by Stacey (1981). Both criteria are equivalent (at least from the mathematical point of view) for perfectly elastic media but not if large deformation effects are considered.

Theoretical analysis of the Brazilian test method are based mainly on the classical continuum mechanics (Claesson and Bohloli 2002; Exadaktylos and Kaklis 2001; Kundu et al. 2016) and is limited to the simplest cases. Analysis of more realistic cases can be done only numerically. Authors of such studies most often use different variants of the Finite and/or Boundary Element Methods (Onate and Rojek 2004; Cai and Kaiser 2004; Zhu and Tang 2006). Only recently, a simple but very interesting analysis based on the Fiber Bundle Method has been presented (Kundu et al. 2016). In this chapter, some of the abovementioned issues were analysed from a "molecular" point of view using the DEM (Abe et al. 2014).

4.3.2 Simulation settings

A number of numerical simulations of Brazilian test (Fig. 18) were performed considering the specimen in the form of disk (cylinder) of diameter 10 mm and thickness 5 mm and diametrically loaded as shown in Fig. 16. The sample was built of spherical particles of varying sizes within predefined ranges. The maximum radius of used particles was always kept fixed and equal to $R_{max} = 0.2$ mm. The minimum radius varies among simulations in the range of 0.027 up to 0.1 mm. An external load was supplied by two perfectly rigid plates. The lower plate was fixed while the upper one moved downward with a constant velocity $V = 4$ mm/sec. Simulations ended when the vertical displacement of the upper plate reached the predefined level of
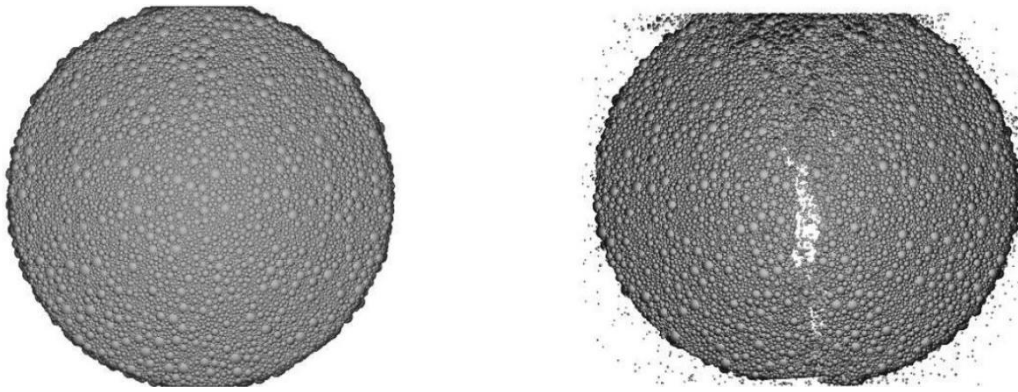

Fig. 17. Example of facial views of a sample before loading (left) and after the creation of a tensile crack (right) in the middle of the sample (after Klejment and Dębski 2017).
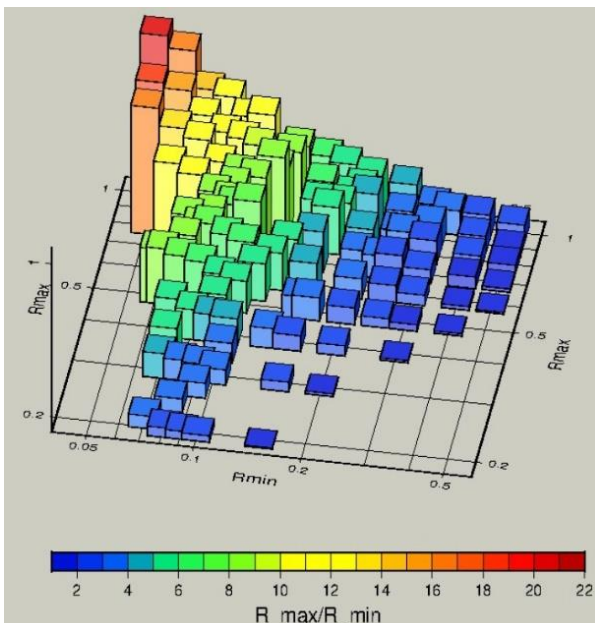

Fig. 18. The relationship between the maximum and minimum particle radii analyzed in simulations.

0.2 mm, selected as large enough to induce the sample breaking and a beginning of the postfail-ure stage. Fig. 17 shows facial views of one of the samples before and after the creation of a main tensile crack (but still before complete breaking of the sample) are shown. During loading, the vertical position of the upper plate and the total vertical force acting on it were recorded at each step; therefore, a stress-strain relation was continuously monitored. Besides, the total ki-netic energy of particles and the total potential energy of inter-particle interactions were also recorded.

The most nontrivial element of any DEM simulation is defining the particle interactions and breaking conditions. The model of "elastic-brittle interactions" supported by ESyS-Particle was used (*BrittleBeamPrms*). Full description of this kind of interactions can be found in the Sec-tion 3.3.2.

Table 8

Brazilian Test simulations – parameter settings

Particles size	in accordance with Fig. 18
Time step	2.0e-06 s
Time steps	1000000
Type of bonds	
Name: *BrittleBeamPrms*	Parameters: name = "pp_bonds", youngsModulus = 100000.0, poissonsRatio = 0.25, cohesion = 1000.0, tanAngle = 1.0, tag = 1
Unbonded particles	
Name: *FrictionPrms*	Parameters: name = "friction", youngsModulus = 100000.0, poissonsRatio = 0.25, dynamicMu = 0.4, staticMu = 0.6
Elastic repulsion with the walls	
Name: *NRotElasticWallPrms*	Parameters: normalK = 1.0e+06
Translational viscous damping	
Name: *LinDampingPrms*	Parameters: viscosity = 0.002, maxIterations = 50
Name: RotDampingPrms	Parameters: viscosity = 0.002, maxIterations = 50
Compressing rate	
Velocity	0.2 mm/s
rampTime	500 time steps

In the current simulations, a question was raised how the size of particles building the sample influences simulation results. For this reason, particle interactions were fixed, and the loading rate was also kept constant. The built disk samples consisted from about $5 \cdot 10^4$ up to almost $2 \cdot 10^6$ particles and typical $5 \cdot 10^4$ time steps were required to break the samples apart. The time step which was used for the temporal integration (evolution) was fixed and reads $dt = 5 \cdot 10^{-6}$ (and was always smaller than time step calculated from the stability criterion Eq. (21) for all parameters sets). With this simulation setup computational time on 10 cores CPU workstation ranged between 6 and 90 hours. The full set of used parameters is presented in Table 8.

4.3.3 Simulation results

The first step of discussion about the obtained results starts from an analysis of the relation between the applied load and vertical displacement (strain) of the sample. The scaled together (for presentation purpose) strain-stress relations for five simulations are shown in Fig. 19 and few particular features are clearly visible in this figure.

First, the maximum attained values of load P_{max}, at which the samples break apart, strongly depend on the minimum size R_{min} of particles building the sample. On the contrary, the critical strain d_c at which f_{max} becomes weak depends on R_{min} ranging from approximately 0.1 mm up to 0.12 mm. Consequently, the slope of the initial part of the strain-stress curves also significantly varies with R_{min}. Second, for small strains, the response of the sample to the load is essentially elastic, manifesting itself in an almost linear strain-stress dependence. The visible undulation of the curve is partially due to an acoustic wave generated at the beginning of loading when the upper plate "hits" the sample with a constant speed and partially due to a numerical noise. Only for very small strains (less than 0.01 mm) this linearity is broken and a "flattening" of the stress-strain curves is observed. This is a purely numerical effect linked to a non-optimum initial packing of particles in the samples. Third, the elastic behaviour vanishes at larger strains and manifests itself as a flattening of the curves. This plastic regime starts earlier for samples built of larger particles. In case of samples with $R_{min} = 0.03$ mm, the plastic regime appears just before reaching the maximum withstand load, while in samples built of particles with $R_{min} \sim$
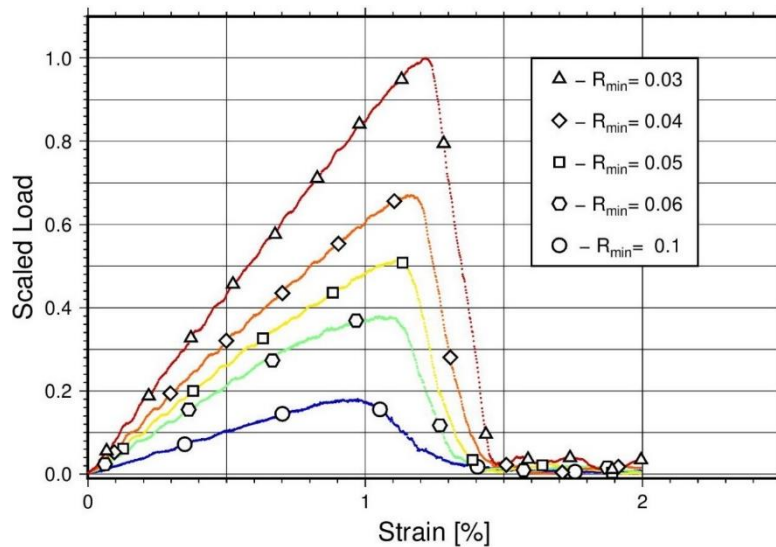

Fig. 19. Load against the vertical displacement (strain) for five different samples composed of particles with different minimum radii R_{min}. The maximum radius was fixed for all samples $R_{max} = 0.2$ mm. The weak undulation in first part of curve is mainly due to acoustic waves generated by the abrupt beginning of loading of the samples in the beginning (after Klejment and Dębski 2017).
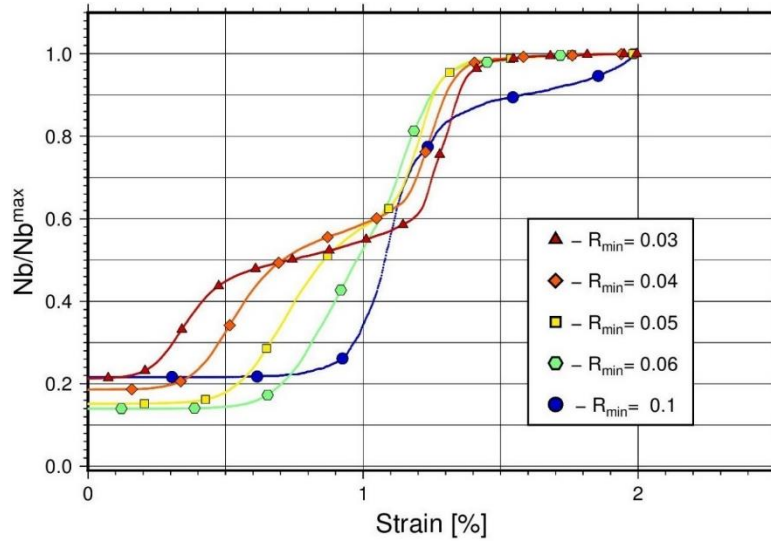
Fig. 20. Number of broken inter-particle bonds as a function of the vertical deformation of a sample (after Klejment and Dębski 2017).

0.1–0.06 mm it starts almost in half of the strain value at given sample breaks. Finally, in the postfailure stage the stress drop rate is smaller for samples built of larger particles. It is interesting to note that the postfailure stress reaches the minimum (complete breakage of the sample) for similar values of strain in all cases. To summarize, a significant mechanical strengthen-ing was observed for samples composed of smaller particles with respect to softer samples build of larger particles. However, the vertical deformation at which samples break apart only weakly depends on R_{min}.

In the next step the variation in the number of broken inter-particle bonds was analysed with the increase in load. The results are shown in Fig. 20 where separately scaled numbers of broken bonds for five considered samples are shown together. The behaviour of plotted curves is very similar in a narrow vicinity of critical strain d_c when samples start to break for all but one case. An abrupt increase in bond breaking starts just around reaching the critical load P_{max} and continues until the sample fully breaks and the load reaches the minimum value. Only for the very soft sample ($R_{min} = 0.1$) inter-particle bonds start to break massively earlier and the process goes smoother with larger range of sample deformations.

The particle composition of the samples influences significantly the initial part of curves corresponding to the elastic behaviour of samples. For deformations less than 0.1 mm (visible in Fig. 20), the smaller are particles inside the sample, the sooner inter-particle bonds start to break. Simultaneously, the smaller the R_{min}, the larger the hardening of a sample before the final breakage is observed. This effect manifests itself by flattening of curves when the strain approaches 0.1 mm. Because during the simulations interaction bonds were not allowed to re-heal after breaking, the observed initial increase of bond breaking can be interpreted as beginning of a viscoplastic deformation of the samples. It should be noted that this effect is quite feeble and can hardly be visible in the strain-stress curves in Fig. 19. The degree of this induced viscosity significantly depends on the particle size. From a physical point of view this observation suggests that at intermediate values of loading, some dislocations are induced in the samples. Indeed, such dislocations are more probable for smaller particles and, for this reason, viscous behaviour would start earlier for samples with smaller R_{min}. Moreover, the particle rearrangement by dislocations very soon leads to denser particle packing and consequently to the hardening of samples. Finally, for a very small deformation, no particle bond breaking was observed. This is a perfectly elastic regime.
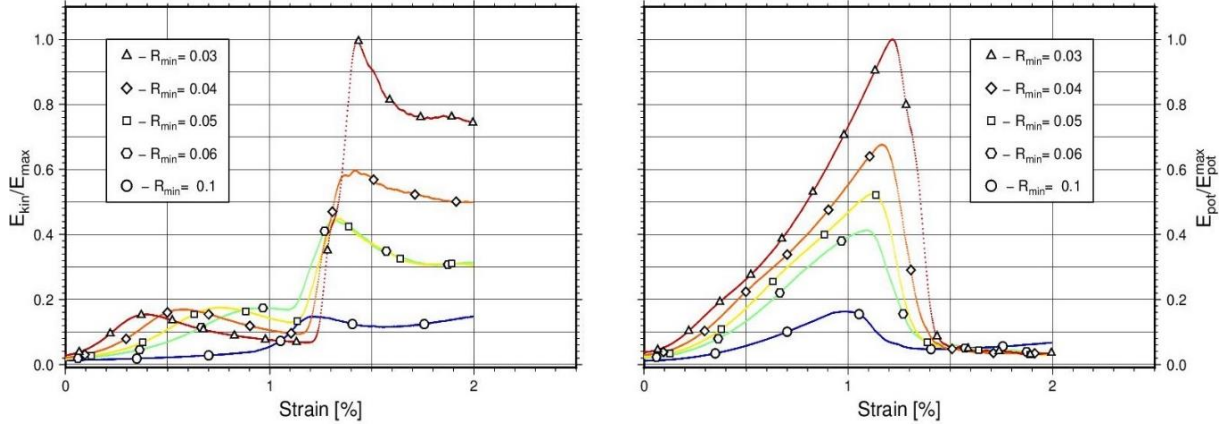
Fig. 21. The absolute value of the kinetic (left) and potential energies of particle interactions (right) scaled to the maximum value obtained in all simulations (after Klejment and Dębski 2017).

Next, the change in the potential energy of particle interaction and the particle kinetic energy was considered (without rotational energy) with progressing vertical deformation. The results are shown in Fig. 21. In the first approximation one can assume that an external compressional load induces harmonic repulsive forces between interacting particles. Consequently, a change in the total potential energy should be proportional to the squared sample deformation. Such a behavior is indeed visible in the right panel in Fig. 21 for small and intermediate deformations. For larger deformations, when the rupture process nucleates, the potential energy starts to be released and diminishes. Besides, these changes of the potential energy with deformation are different for samples with different R_{min}. The potential energy increases most rapidly for samples build of smaller particles and reaches larger values, as expected. The samples built of smaller particle can accumulate larger elastic deformation (potential) energy. As a result, considering that the breaking (critical) strain d_c only slightly increases with the decrease in R_{min} and deformation at which the samples break apart is almost the same for all samples bacause the potential energy released is more abrupt for samples with smaller R_{min}. Thus, it can be expected that the breaking process will be faster for samples build of smaller particles.

As far as the kinetic energy E_{kin} is concerned, it is visible in the left panel of Fig. 21 that it is quite stable in the first phase of loading. Some increase and variations in E_{kin} at the intermediate loading can be attributed to the dislocation processes discussed above. During the breaking stage, the kinetic energy increases significantly due to the release of potential energy. The changes (mostly decrease) of E_{kin} in the postfailure stage are more complex due to a possible secondary cracking of the samples (Cai 2013). However, at this stage, the behavior of E_{kin} is also strongly influenced by a numerical dumping implemented in the used code and thus include a non-physical component. For this reason this stage is not analysed any more.

Considering energy transformations during the loading and breaking stages of the process the difference was analysed between the work of the external load and the sum of the kinetic and potential energies. The obtained results are shown in Fig. 22.

For small, elastic deformations the work of the loading force (ΔW) fully converts into the elastic ($E_T = E_{kin} + E_{pot}$) energy. Consequently, $\Gamma = \Delta W - E_T$ vanishes. At the intermediate loading stage a monotonic increase of Γ with the sample deformation can be observed. This is a signature of non-elastic transfer of external energy. This can be attributed to the breaking of inter-particle interaction bonds and particle dislocations. In real materials at this stage the external energy is also efficiently transformed into the heat energy. However, in performed simulations, the thermal effects were not considered. It is interesting to observe that at this stage Γ exhibits a strong dependence on particle size (R_{min}). During the breaking stage ($0.11 < dl < 0.14$) Γ further increases and finally saturates, as expected.
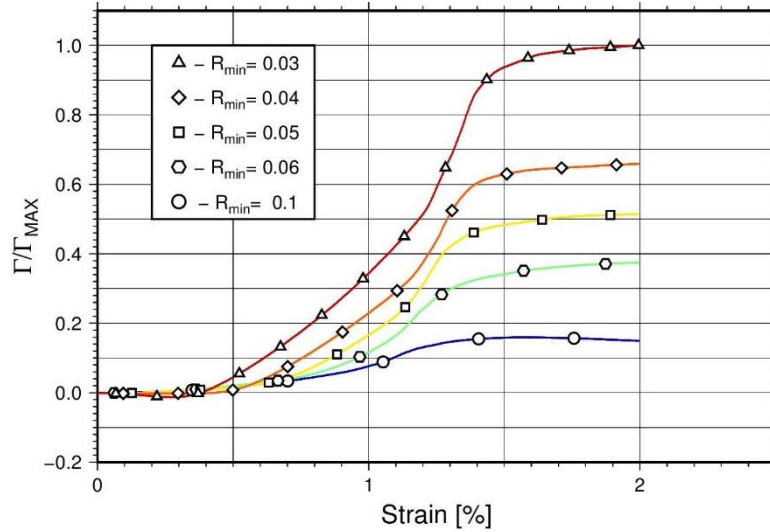
Fig. 22. The difference between external load work (ΔW) and the sum of kinetic and potential energies. The obtained values were scaled by the largest value obtained in all simulations (after Klejment and Dębski 2017).
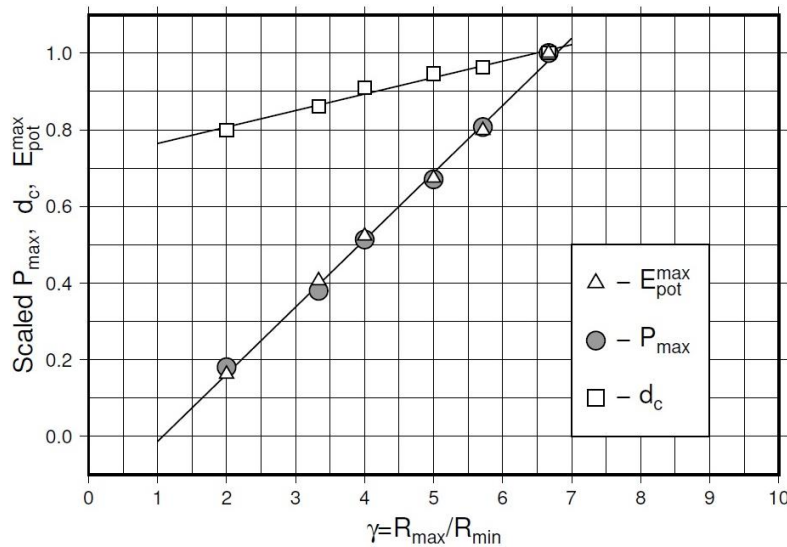

Fig. 23. The maximum critical load, critical strain d_c and potential energy at d_c strain as the function of $= R_{max}/R_{min}$ (after Klejment and Dębski 2017).

From the results shown in Fig. 19 it was noticed that the maximum load the sample can withstand depends significantly on R_{min}. To analyze this issue deeper, the maximum loads P_{max}, d_c, and the potential energy at the d_c strain for all considered samples were plotted, as shown in Fig. 23.

The obtained results show that the dependence of P_{max} on inverse of R_{min} is almost perfectly linear. A quite similar behaviour is exhibited by the potential energy calculated for the strain when the load reaches its maximum value. The critical strain d_c is also almost linearly dependent (but, much weaker) on the R_{max}/R_{min} ratio. Presently, no explanation of this observed P_{max} (potential energy) scaling was found. Indeed, a preliminary analysis carried out for a larger set of samples with different R_{max} confirmed with a quite good approximation that P_{max} depends only on the R_{max}/R_{min} ratio and thus the reported scaling holds.

4.3.4 Conclusions

With the performed numerical simulations a few goals were attained. From the technical point of view, it was proved that ESyS-Particle software works correctly with this type of problems, providing the most advanced particle interaction model is used. The obtained results are in full agreement with similar results obtained both analytically and by a more traditional FEM methods (Cohen et al. 2009; Kundu et al. 2016; Li and Wong 2013). Moreover, exceptional abilities of the DEM method with solving problems including sample fragmentation was demonstrated.

The method has allowed a detailed monitoring of internal microscopic state of loaded samples including changes in kinetic and potential energies of particles. From the physical point of view, an insight into the creation of the tensile cracks under the simulated laboratory conditions was obtained. It was able to monitor the nucleation and temporal evolution of a tensile crack which finally led to the breaking apart of Brazilian test samples. Following the evolution of the total kinetic and potential energies during loading it was possible to identify a few stages in a response of the samples to constant speed loading. At the beginning of loading, the elastic response of the samples was clearly visible. For the intermediate loading, the samples exhibited a viscoelastic property due to the induced particle dislocations. At the end of this stage, large dislocation occurring in block resulted in a visible plastic behaviour of the samples and finally led to crack nucleation and breaking the samples apart.

The most interesting was, however, observing how size of used particles influenced each of the above stage. Although relatively small range of particle sizes was used, the obtained results clearly showed that the most sensitive to the material composition is the intermediate loading stage when dislocations start to change the properties of materials and lead to crack nucleation. On the other hand, the rather weak dependence of the critical strain and the strain when the crack fully breaks the sample into two pieces shows that this failure stage is rather insensitive to the material composition. However, it seems that the most important result of the performed simulations is reporting of the scaling of the critical load which the sample can withstand with the inverse of the size of the smallest particles building the sample. At present, no physical explanation of the observed scaling can be given.

4.4 Uniaxial stretching

Simulations of the uniaxial stretching are the third case of this part of the dissertation. Some of these results were presented at 17th International Fatigue Congress in Poitiers, 2018 (Klejment and Dębski 2018).

4.4.1 Motivation and outline

In contrast to the theory of elasticity, which deals with materials that have a capacity to store mechanical energy, the theory of viscoelasticity is associated with those materials that are capable of dissipating mechanical energy as well as storing it (Pestel and Leckie 1963, Sadd 2009). If a load is suddenly applied – but not impulsively so as to excite a dynamic response – an elastic material will respond instantaneously and reach a final state of deformation. There are materials for which a suddenly applied and maintained state of uniform stress induces an instantaneous deformation followed by a flow process that may or may not be limited in magnitude as time elapses (Christensen 2010; Ferry 1965). This is the behaviour that is referred to as viscoelastic. The governing differential equations in viscoelasticity are linear if infinitesimal strains are considered, whereas they become nonlinear if large strains are involved. Viscoelastic materials can be modeled in order to determine their stress and strain or force and displacement relations as well as their temporal dependencies. Viscoelastic behavior has elastic and viscous components modeled as linear combinations of springs and dashpots, respectively (Eringen 1962; Mavko et al. 1998).

The elastic components, as previously mentioned, can be modeled as springs of elastic constant E, given the formula:

$$\sigma = E\varepsilon \qquad (27)$$

where σ is the stress, E is the elastic modulus of the material, and ε is the strain that occurs under the given stress, similar to Hooke's law.

The viscous components can be modeled as dashpots such that the stress-strain rate relationship can be given as

$$\sigma = \eta \frac{d\varepsilon}{dt} \qquad (28)$$

where σ is the stress, η is the viscosity of the material, and $d\varepsilon/dt$ is the time derivative of strain. (Roylance 2001a).

The most important viscoelastic models are, namely, the Maxwell model, the Kelvin–Voigt model, the standard linear solid model, and the Burgers model. They are used to predict a material's response under different loading conditions.

The Maxwell model can be represented by a purely viscous damper and a purely elastic spring connected in series (Fig. 24). The model can be represented by the following equation $\sigma + \frac{\eta}{E}\dot{\sigma} = \eta\dot{\varepsilon}$. Under this model, if the material is put under a constant strain, the stresses gradually relax. When a material is put under a constant stress, the strain has two components. First, an elastic component occurs instantaneously, corresponding to the spring, and relaxes immediately upon release of the stress. The second is a viscous component that grows with time as long as the stress is applied (Lakes 2009; Roylance 2001a; Tanner 2000; McCrum et al. 1997; Meyers and Chawla 2008). The Maxwell model predicts that stress decays exponentially with time. One limitation of this model is that it does not predict creep accurately. The Maxwell model for creep or constant-stress conditions postulates that strain will increase linearly with time.

The Kelvin–Voigt model, also known as the Voigt model, consists of a Newtonian damper and Hookean elastic spring connected in parallel (Fig. 25). The constitutive relation is expressed as a linear first-order differential equation $\sigma = E\varepsilon + \eta\dot{\varepsilon}$. This model represents a solid undergoing reversible, viscoelastic strain (Lakes 2009; Roylance 2001a; Tanner 2000; McCrum et al. 1997; Meyers and Chawla 2008). Upon application of a constant stress, the material deforms at a decreasing rate, asymptotically approaching the steady-state strain. When the stress is released, the material gradually relaxes to its undeformed state. At constant stress (creep), the model is quite realistic as it predicts strain to tend to σ/E as time continues to infinity. Similar to the Maxwell model, the Kelvin–Voigt model also has limitations. The model is extremely good with modelling creep in materials, but with regards to relaxation the model is much less accurate.
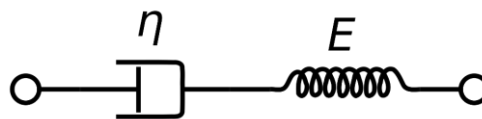

Fig. 24. Schematic representation of the viscoelastic Maxwell model (Roylance 2001a).
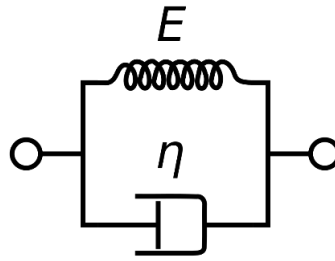
Fig. 25. Schematic representation of the viscoelastic Kelvin–Voigt model (Roylance 2001a).

The standard linear solid model, also known as the Zener model, consists of two springs and a dashpot. It is the simplest model that describes both the creep and stress relaxation behaviors of a viscoelastic material properly. For this model, the governing constitutive relations are: $\sigma + \frac{\eta}{E_2}\dot{\sigma} = E_1\epsilon + \frac{\eta(E_1+E_2)}{E_2}\dot{\varepsilon}$ (Maxwell representation, Fig. 26), $\sigma + \frac{\eta}{E_1+E_2}\dot{\sigma} = \frac{E_1E_2}{E_1+E_2}\epsilon + \frac{E_1\eta}{E_1+E_2}\dot{\epsilon}$ (Kelvin representation, Fig. 26). Under a constant stress, the modeled material will instantaneously deform to some strain, which is the instantaneous elastic portion of the strain. After that it will continue to deform and asymptotically approach a steady-state strain, which is the retarded elastic portion of the strain (Lakes 2009; Roylance 2001a; Tanner 2000; McCrum et al. 1997; Meyers and Chawla 2008). Although the Standard Linear Solid Model is more accurate than the Maxwell and Kelvin–Voigt models in predicting material responses, mathematically it returns inaccurate results for strain under specific loading conditions.

The Burgers model combines the Maxwell and Kelvin–Voigt models in series (Fig. 27). The constitutive relation is expressed as follows: $\sigma + \left(\frac{\eta_1}{E_1} + \frac{\eta_2}{E_2} + \frac{\eta_3}{E_3}\right)\dot{\sigma} + \frac{\eta_1\eta_2}{E_1E_2}\ddot{\sigma} = \eta_2\dot{\epsilon} + \frac{\eta_1\eta_2}{E_1}\ddot{\epsilon}$. This model incorporates viscous flow into the standard linear solid model, giving a linearly increasing asymptote for strain under fixed loading conditions.
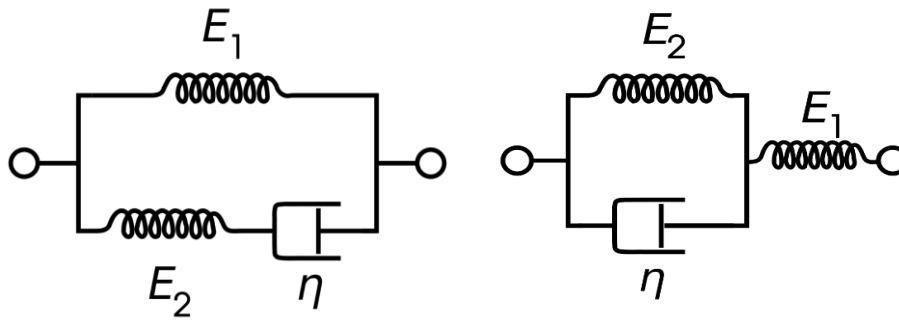

Fig. 26. Schematic representation of the viscoelastic standard linear solid model. On the left is the Maxwell representation, on the right the Kelvin representation (Roylance 2001a).
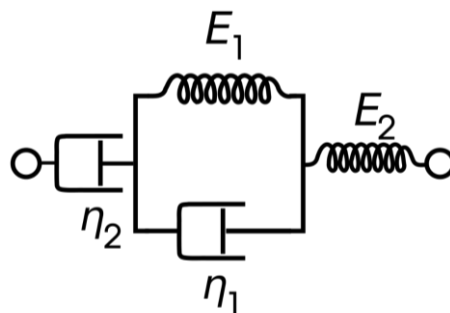

Fig. 27. Schematic representation of the viscoelastic Burgers model (Roylance 2001a).
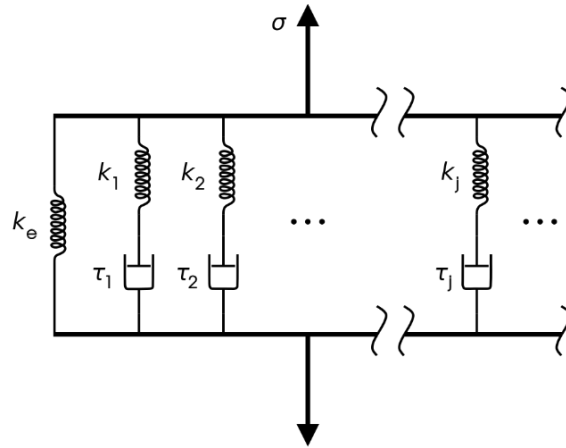
Fig. 28. Schematic representation of the viscoelastic Wiechert model (Roylance 2001a).

The Generalized Maxwell model, also known as the Wiechert model (Fig. 28), is the most general form of the linear model for viscoelasticity (Tanner 2000; McCrum et al. 1997; Meyers and Chawla 2008). It takes into account that the relaxation does not occur at a single time, but at a distribution of times. Due to molecular segments of different lengths, with shorter ones contributing less than longer ones, there is a varying time distribution. The Wiechert model shows this by having as many spring–dashpot Maxwell elements as are necessary to accurately represent the distribution (Mavko et al. 1998; Roderic 2019).
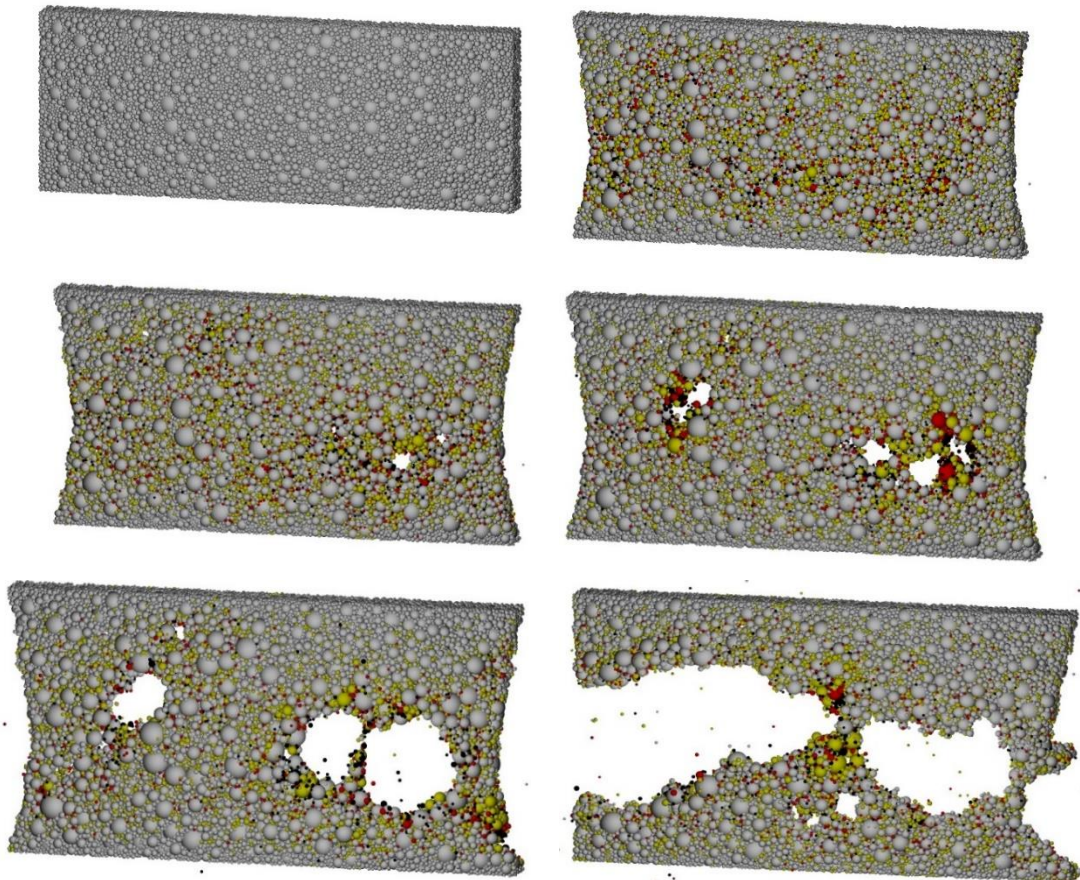

Fig. 29. Crack nucleation in a three-dimensional elastic material – a sequence of snapshots of the sample state. Intensity of colours stands for kinetic energy of particles (grey – the lowest, red and black – the highest).
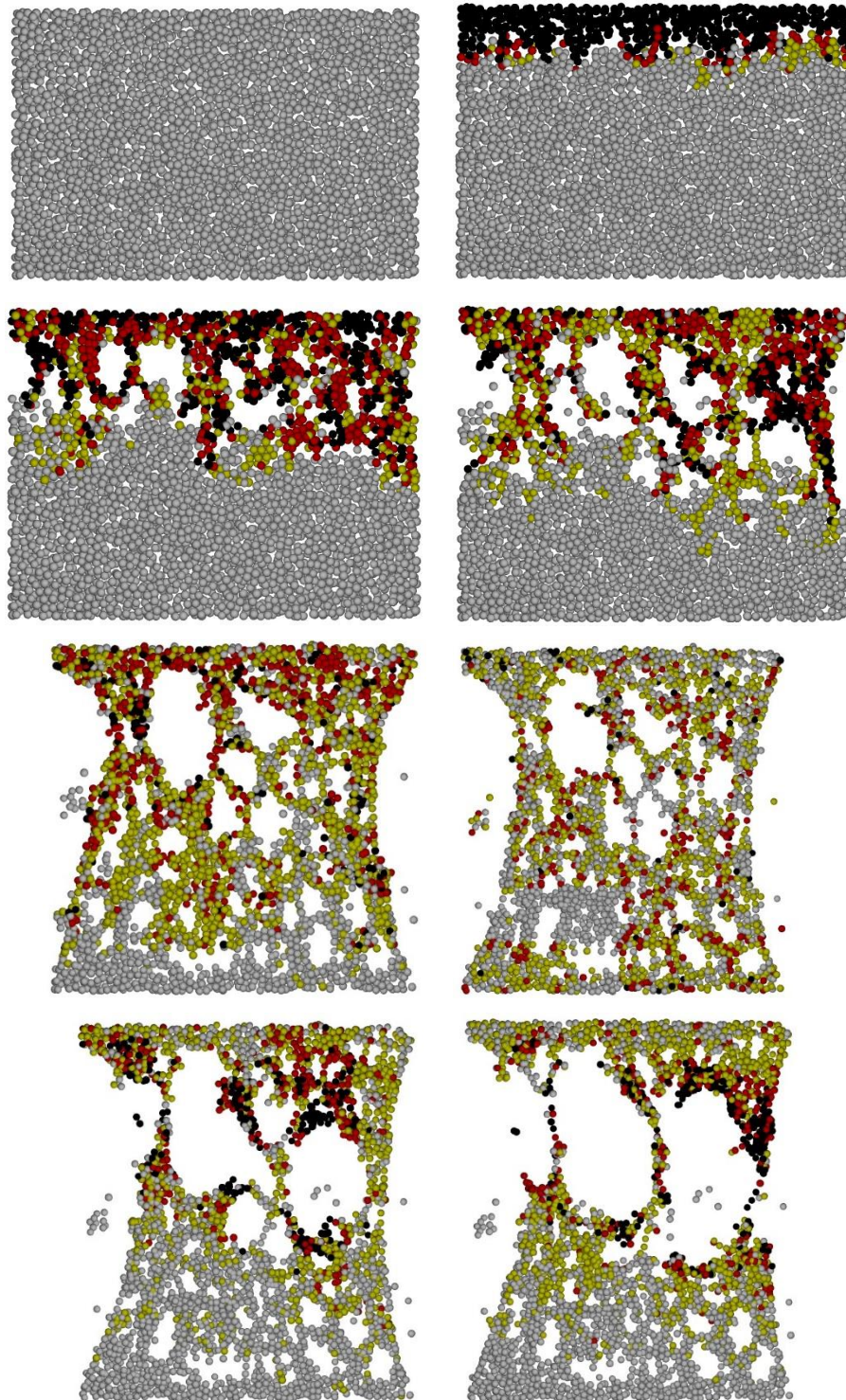
Fig. 30. Crack nucleation in a two-dimensional elastic material – a sequence of snapshots of the sample state. Intensity of colours stands for kinetic energy of particles (grey – the lowest, red and black – the highest).

The aim of this research was to examine the cracking processes on a scale typical for engineering and seismology (millimeters to meters) using micro-physics methods. The research was mainly focused on cracking hypothetical 3D materials subjected to uniaxial stretching with constant velocity and sample deformation. The proposed DEM model was related to the above-mentioned viscoelastic materials models, because in the model particles are connected with

each other by springs with implemented damping. Examples of cracks nucleation in two- or three-dimensional material in such a DEM model are presented in Fig. 29 and 30 with boundary conditions as in Fig. 31. This simulation setup can be used to analyse the behaviour of cracking structures such as thin films (e.g., biological structures), metal coverings (e.g., aircraft fuselages) or tailoring materials. Additionally, viscoelastic behaviour is also very common in geophysics.

According to Brennan (1981) the anelastic behavior of rocks and the consequences of this anelasticity are topics of considerable interest. Problems involving anelasticity are naturally more tractable if the anelastic behaviour is linear, in which case it is described by the theory of linear viscoelasticity (Timár et al. 2010). For geophysicists one of the most significant results in the theory of linear viscoelasticity is an existence of dispersion relations which relate the frequency dependences of the phase velocity and the attenuation coefficient. Carcione (1990) observed that the anisotropic linear viscoelastic rheological relation constitutes a suitable model for describing the variety of phenomena which occur in seismic wavefields. Additionally, Carcione (1993) proposed two-dimensional (2-D) and three-dimensional (3-D) forward modeling in linear viscoelastic media. Yang et al. (2015) noticed that energy is absorbed and attenuated when seismic waves propagate in real earth media. Hence, the viscoelastic medium needs to be considered. Farrington et al. (2014) found that subduction of tectonic plates into Earth's mantle occurs when one plate bends beneath another at convergent plate boundaries. The characteristic time of deformation at these convergent boundaries approximates the Maxwell relaxation time for olivine at lithospheric temperatures and pressures, it is therefore by definition a viscoelastic process. While this is widely acknowledged, the large-scale features of subduction can, and have been, successfully reproduced assuming the plate deforms by a viscous mechanism alone.

The presented research has focused mainly on analyzing the process of cracks nucleation in materials similar to viscoelastic, with different intrinsic parameters and subjected to various external loads. Simulated processes were considered with regards to energy changes inside the material during the loading, as well as deformations in the material structure.
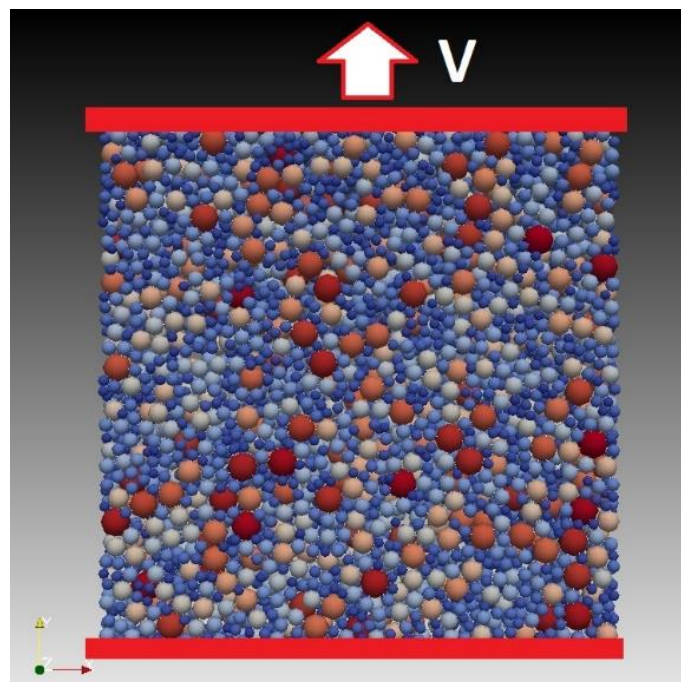

Fig. 31. The sample used in the simulations which consists of 3,587 randomly distributed particles with radii of 0.1–0.3 mm.

4.4.2 Simulation settings

Simulations were conducted assuming that the tested materials can be described as a collection of "tight" packed spherical particles with different radii (statistical inhomogeneity of materials) in a given area interacting with each other by harmonic forces that can be represented as springs that connect the "molecules". The simulations were performed by a relatively simple mechanism of cracking solids under the influence of uniaxial stretching.

Despite the simplicity of the used model, such simulations have already provided valuable information on the characteristics of the area around the tip of the developing cohesive zone. In performed simulations, the block of particles (Fig. 31) was inserted into the simulation object. Non-rotational elastic bonds between bonded particles were created as specified in the *NRot-BondPrms* (Abe et al. 2014*)* parameter set. Detailed description of this kind of interaction can be find in the Section 3.3.2. The full set of used parameters is presented in Table 9.

Table 9

Uniaxial stretching simulations – parameter settings

Particles size	from 0.1 to 0.3 mm
Time step	1.0e-05s
Time steps	200000
Type of bonds	
Name: *NRotBondPrms*	Parameters: youngsModulus = 1.0e+06, poissonsRatio = 0.25, cohesion = 1000.0, tanAngle = 1.0
Unbonded particles	
Name: *NRotFrictionPrms*	Parameters: name = "pp_friction", normalK = in accordance with Table 10, dynamicMu = 0.6, shearK = 100.0, scaling = True
Elastic repulsion with the walls	
Name: *NRotElasticWallPrms*	Parameters: normalK = the same as normalK in *NRotFrictionPrms*
Translational viscous damping	
Name: *LinDampingPrms*	Parameters: viscosity = 1.0, maxIterations = 100
Stretching rate	
Velocity	5, 10 or 50 mm/s
rampTime	1000 time steps

4.4.3 Simulation results

As it is shown in Table 10, various samples with different elastic stiffness of the bonds between particles were prepared. Samples (Fig. 31) had 3576 particles with radii from 0.1 to 0.3 mm and dimensions 10 mm × 10 mm × 1 mm. Firstly, a series of measurements of uniaxial stretching

were conducted with clamps velocity equal to 1 mm/s. The aim was to calculate the macroscopic Young's modulus of the samples. In this way it was possible to recognize what type of real elastic material the checked samples correspond to.

Then, after calibration, a series of measurements with three uniaxial stretching velocities: 5, 10, and 50 mm/s were carried out. For each value the maximum stress when the main crack occurs was calculated. It was interesting to note that the maximum stress weakly depends on elastic stiffness for smaller values of this parameter (500–20000 for velocities 10 and 50 mm/s, 500–10000 for velocity 5 mm/s). In this range, the character of cracking seemed to be similar. However, for higher values of elastic stiffness there was significant increase in the maximum value of stress. At the same time, for the same value of elastic stiffness, different uniaxial stretching velocities weakly influenced the maximum stress.

Table 10

Micro- and macro-parameters of models used in further analyses.
The parameter k defines the strength of inter-particle interactions
and E stands for Young's modulus

Model	A	B	C	D	E	F	G
k	500	1000	5000	10000	20000	50000	200000
E [GPa]	1.57	2.56	10.81	20.41	39.54	95.01	363.89

During the main part of the numerical experiment, the samples A–G were vertically stretched with three velocities: 5, 10 and 50 mm/s, until the samples completely split into two separate parts. The dragging force and the vertical strain of the samples were being monitored throughout the experiment. A special attention was paid to the strength of the samples – the maximum stress the samples can withstand. Because it was measured at a relatively large vertical deformation rate, it was referred as the *dynamical strength*. At this point it should be recalled that the classical laboratory strength measurements are quasi-static, i.e. performed with much lower dragging/compression as in presented experiments. The results are shown in Table 11.

Table 11

Maximum uniaxial strength of the considered samples in MPa
for three considered dragging velocities

Model	A	B	C	D	E	F	G
5 mm/s	732	733	742	814	1578	3890	14852
10 mm/s	1465	1467	1483	1503	1634	4034	15176
50 mm/s	7325	7335	7414	7510	7696	8209	16302

Two conclusions can be drawn from the obtained results. First, for the relatively weak materials (models A–C) a weak dependence of the sample strength on its elastic stiffness is observed, independent of the used dragging velocity. Moreover, this strength almost linearly increases with the dragging velocity. Thus, almost linear dynamic strengthening of the material is observed. Situation changes if harder materials are considered (models E–G). In such cases, for the lowest dragging velocity, 5 mm/s, the strength of the sample increases almost linearly with E. For intermediate velocity, 10 mm/s, some deviation from this linearity is observed, which finally leads to breaking down of the sample for the highest dragging velocity. For these

models, velocity-dependent strengthening of the materials can be also seen, which decreases, however, for more stiff samples, almost vanishing for the sample G.

Three types of cracking

By analysing the stress-strain curves, three different types of cracking were distinguished:

1. Type I: when multicracking occurs and, as a result, the cracking disperses in time. For this type of cracking, it is impossible to determine the main breaking event at a specific time. An example of the stress-strain curve for this type of cracking and a snapshot of crack development are shown in Fig. 32.
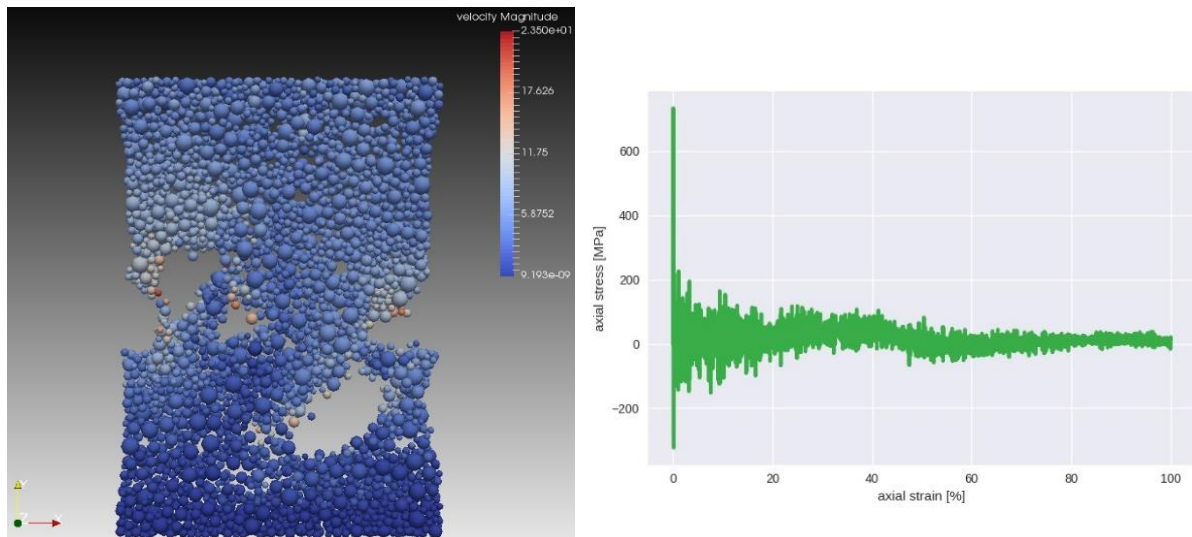

Fig. 32. An example of the stress-strain curve (right) and snapshot of the fracturing process for the type I of cracking.

2. Type II when dominating "macro-cracks" accompanied by smaller micro-cracks are developing. An example of the stress-strain curve for this type of cracking and a snapshot of cracks development is shown in Fig. 33.
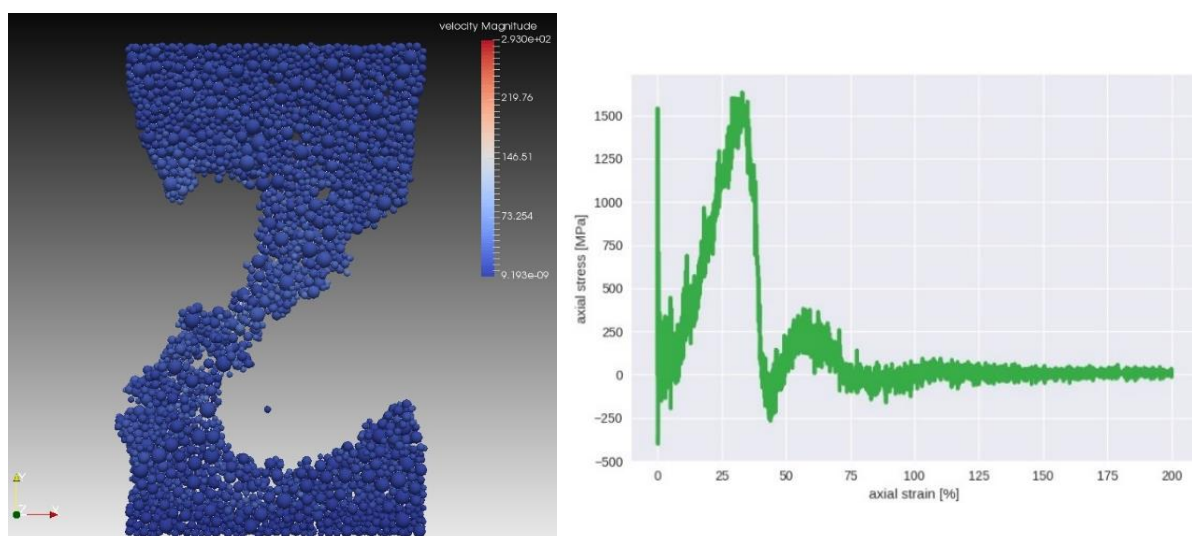

Fig. 33. An example of the stress-strain curve (right) and snapshot of a fracturing process for the type II of cracking.

3. Type III when a single crack is created. An example of the stress-strain curve for this type of cracking and a snapshot of crack development are shown in Fig. 34.
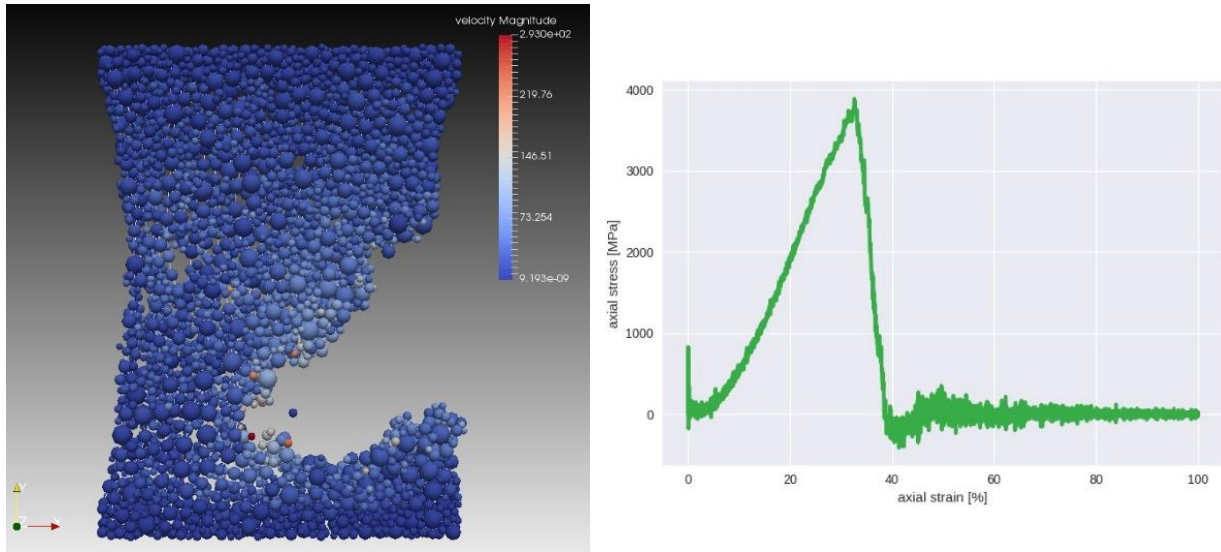

Fig. 34. An example of the stress-strain curve (right) and snapshot of a fracturing process for the type III of cracking.

In fact, the difference between cracking types I and II is quite visible, while the difference between types II and III is much less pronounced and manifests itself in a "noisy" linear (elastic) part of the stress-strain curve (type II) due to a development of secondary micro-cracks.

The observed type of cracking appears with a certain regularity depending on the experiment setup, as follows from Table 12. Type I is observed for the weakest materials only. Moreover, when the dragging velocity is high, stronger materials break by type I cracking. Type II and III are observed for stronger materials only with a tendency to fracturing according to type II rather than type III.

Table 12
Types of observed cracking

Model	A	B	C	D	E	F	G
5 mm/s	I	I	II	III	II	II	II
10 mm/s	I	I	I	III	II	II	II
50 mm/s	I	I	I	I	III	III	II

Kinetic and elastic energy

The kinetic energy refers here to the total kinetic energy of all particles at every time step. This energy is related only with the linear movement of the particles because rotational ones are not considered in performed simulations. On the *x*-axis, the strain (right) and the strain scaled to the maximum value (left) during simulation are presented.

The higher the elastic stiffness of the bonds, the higher the kinetic energy during uniaxial stretching (Fig. 35). It is interesting to note that for the same velocity, 5 mm/s, all curves have almost the same shape and the maximum occurs for the same strain.
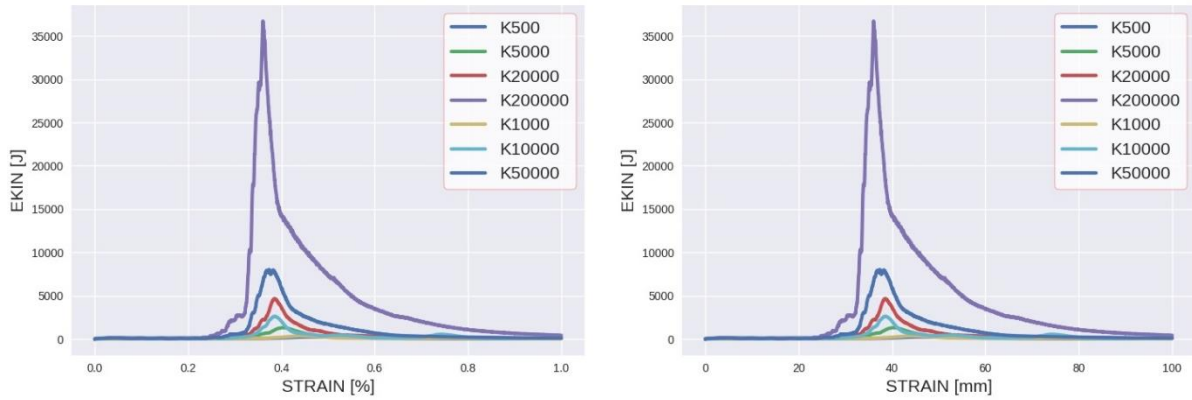
Fig. 35. Kinetic energy of all particles as a function of scaled strain (left) and strain (right) for uniaxial stretching with 5 mm/s velocity.

Fig. 36. Kinetic energy of all particles as a function of scaled strain (left) and strain (right) for uniaxial stretching with 10 mm/s velocity.
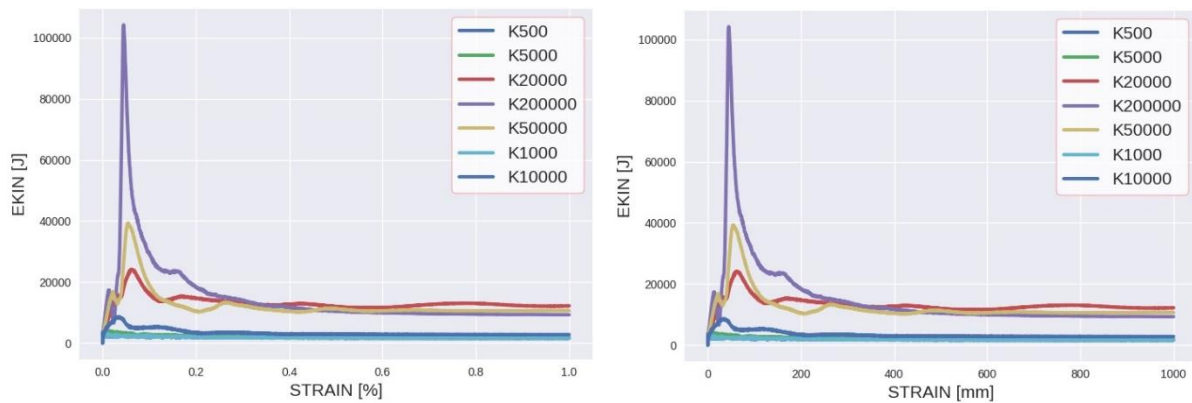
Fig. 37. Kinetic energy of all particles as a function of scaled strain (left) and strain (right) for uniaxial stretching with 50 mm/s velocity.

Figure 36 shows the dependence for 10 mm/s velocity. The energy of the cracking process is higher; however, it is not two times as one would expect on the basis of velocity change from 5 to 10 mm/s. It is interesting, as shown in Figs. 35–37, that the strain, when the peak of the kinetic energy occurs, seems not to depend on the stretching velocity and elastic stiffness of bonds. In the abovementioned figures, the strain is scaled to the maximum value; however, in real numbers, the strain is almost the same for all simulations.

Potential energy

Potential energy describes all kinds of interactions connected with bonds between particles. As in case of kinetic energy, this is total value in every time step. Results are shown in Figs. 38–40. Two interesting results can be observed. First, as in the case of kinetic energy, the strain for which peak of energy occurs seems not to depend on the stretching velocity and elastic stiffness of bonds. Additionally, the maximum value of potential energy strongly depends on elastic

Fig. 38. Potential energy of all bonds between particles as a function of strain (left) and scaled strain (right) for uniaxial stretching with 5 mm/s velocity.
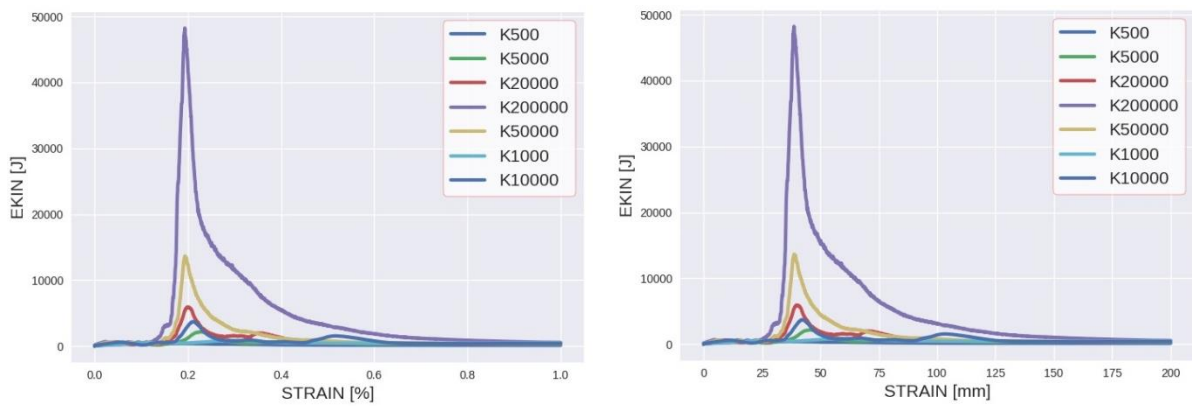
Fig. 39. Potential energy of all bonds between particles as a function of strain (left) and scaled strain (right) for uniaxial stretching with 10 mm/s velocity.
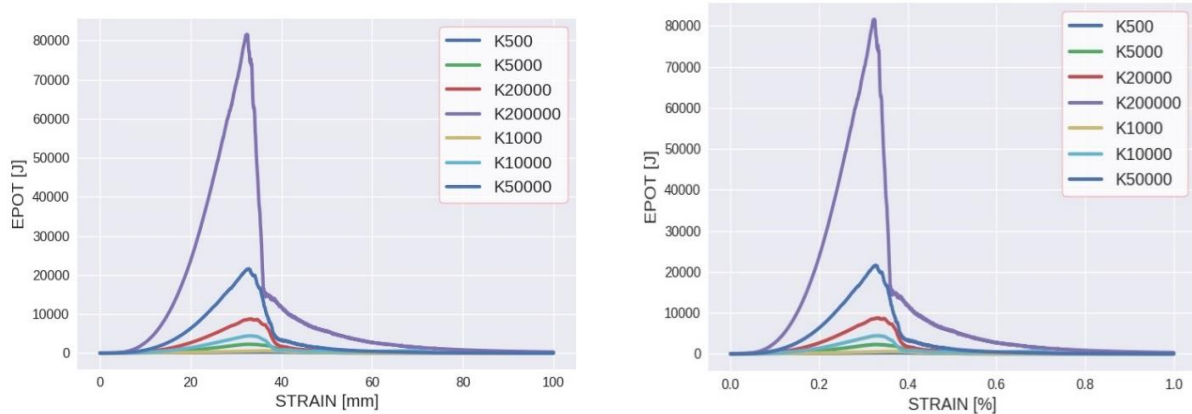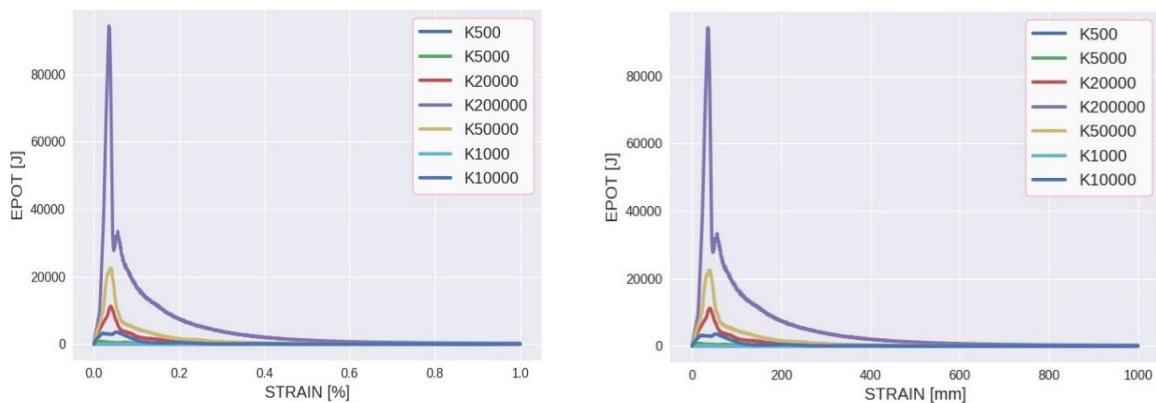
Fig. 40. Potential energy of all bonds between particles as a function of strain (left) and scaled strain (right) for uniaxial stretching with 50 mm/s velocity.
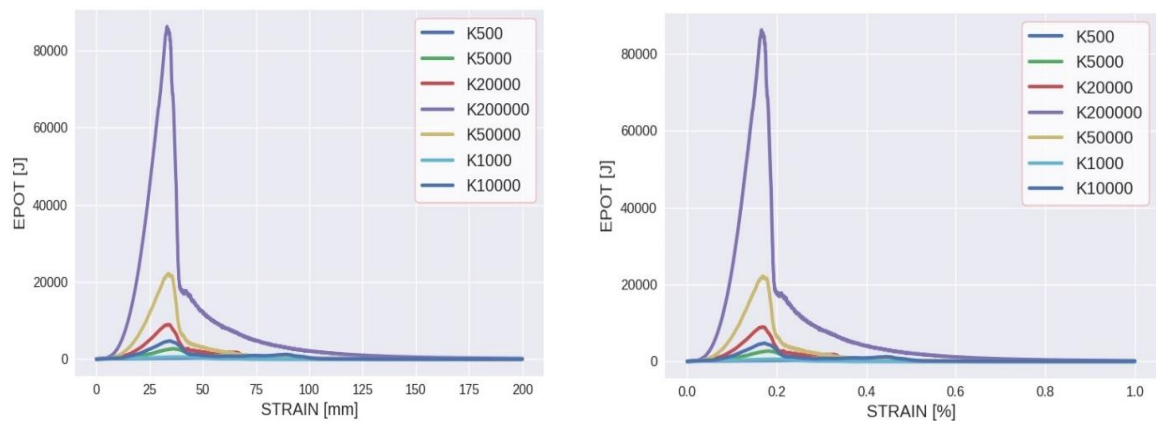
stiffness; however, it does not depend much on velocity. For instance, for an elastic stiffness of 200 000 N/mm, the total maximum potential energy is equal to about 80 000 J and only slightly changes when the velocity increases from 5 to 50 mm/s.

Number of bonds

The initial number of bonds between particles inside the material was about 9700. The relationship between the number of bonds as well as elastic stiffness and velocity is shown in Figs. 41–43. For velocity of 5 mm/s, paradoxically, the highest loss of bonds occurred for elastic stiffness 1,000. This clearly shows that there is no clear relationship between these parameters. For

Fig. 41. Number of bonds between particles as a function of scaled strain (left) and strain (right) for uniaxial stretching with 5 mm/s velocity.

Fig. 42. Number of bonds between particles as a function of scaled strain (left) and strain (right) for uniaxial stretching with 10 mm/s velocity.
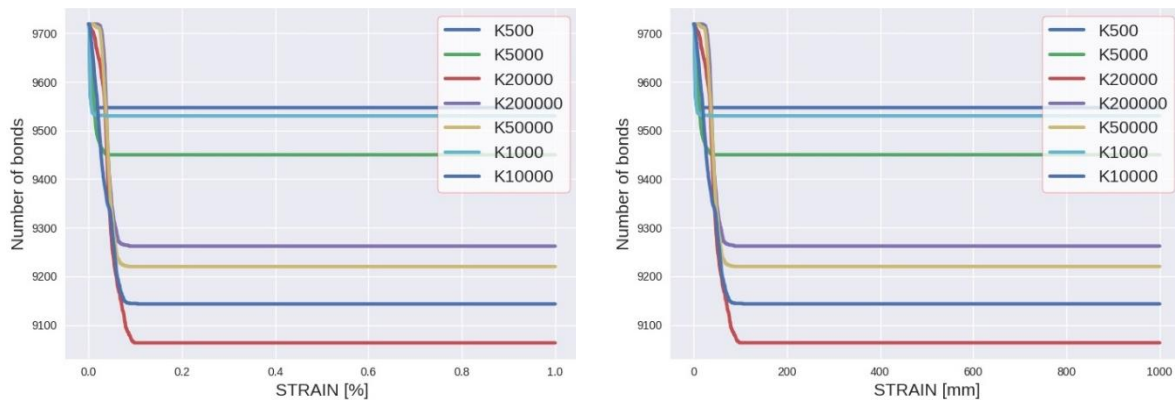
Fig. 43. Number of bonds between particles as a function of scaled strain (left) and strain (right) for uniaxial stretching with 50 mm/s velocity.
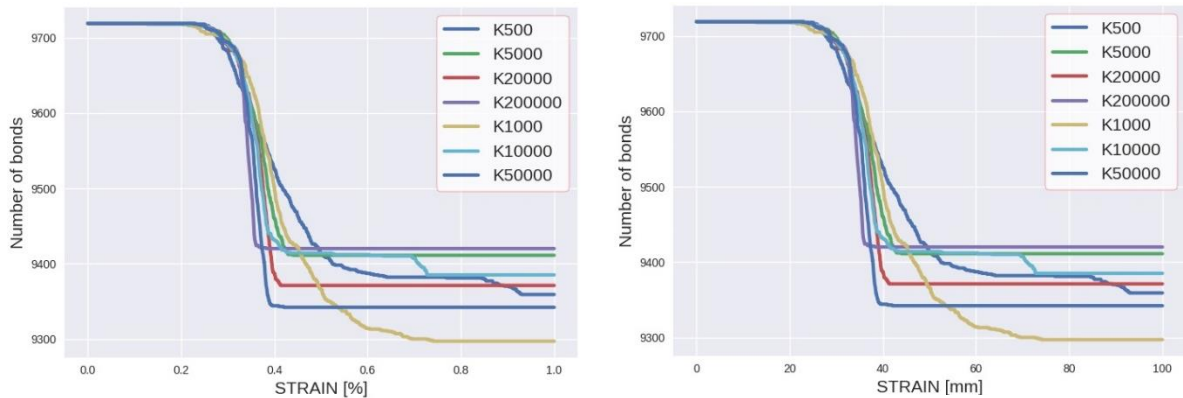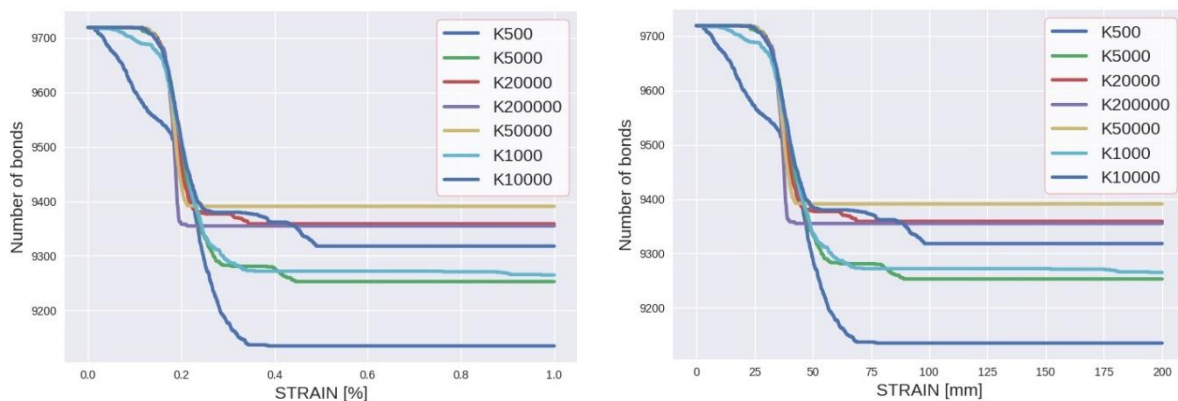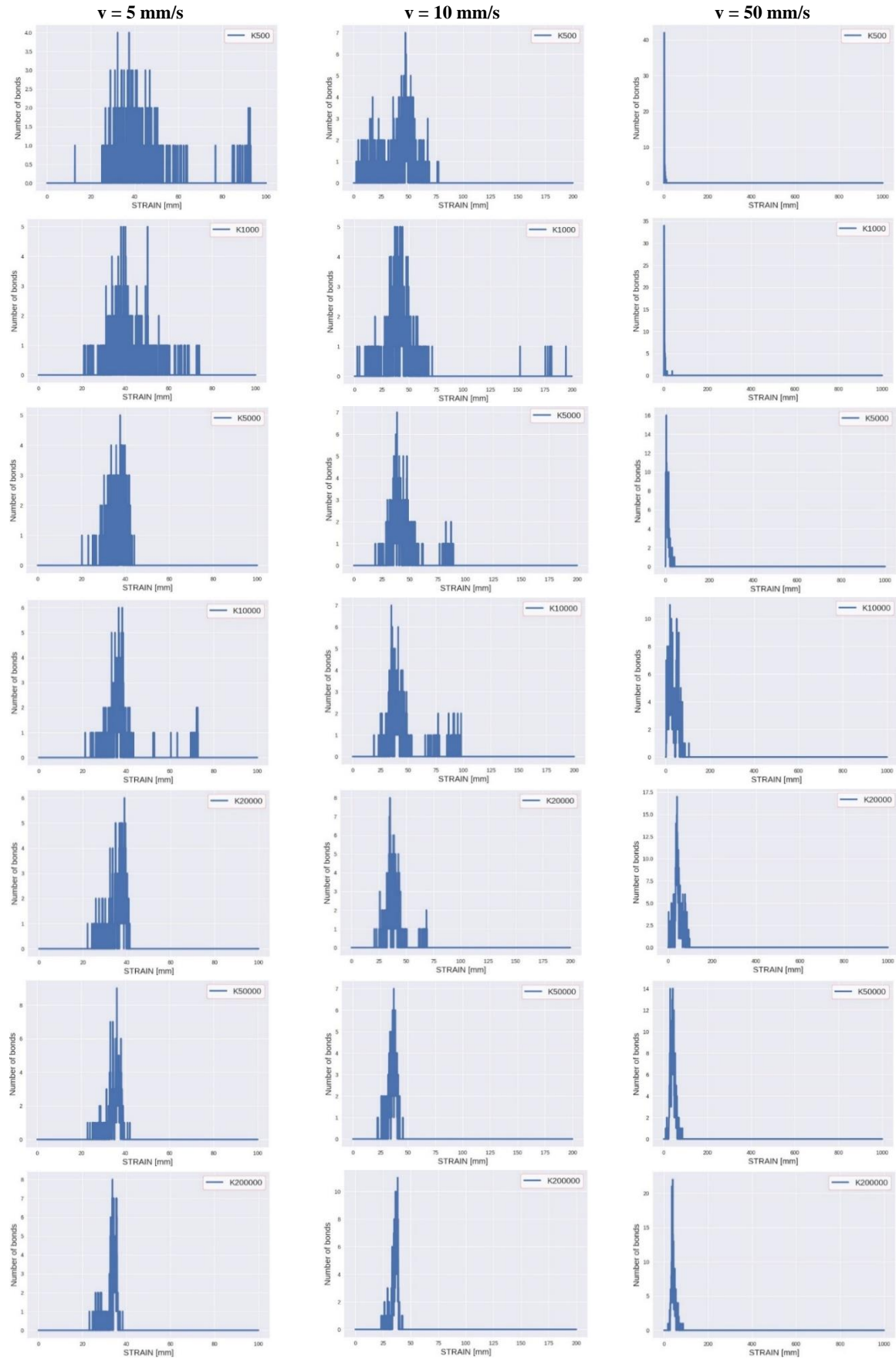
Fig. 44. Dynamics of changes in the number of bonds for dragging velocities: 5, 10, 50 mm/s and different elastic stiffness of bonds.

velocity of 10 mm/s, a similar result is observed, as shown in Fig. 42. The result for 50 mm/s velocityis quite interesting, which is shown in Fig. 43. For this type of stretching, the change in the number of bonds is the most rapid and after cracking quickly becomes constant.

Dynamics of changes in the number of bonds

In Fig. 44 the results of investigation on the number of broken bonds with time are presented. It was checked how many bonds disappear in every time step for stretching velocities of 5, 10 and 50 mm/s for different elastic stiffness of bonds. For higher values of K and for larger velocities, bonds disappear significantly faster.

Maximum kinetic and potential energy

Almost linear dependence was observed between the maximum kinetic energy during the entire simulation and stretching velocity, for different values of elastic stiffness of bonds (Fig. 45). Meanwhile, the maximum potential energy was almost constant as a function of stretching velocity (Fig. 46).
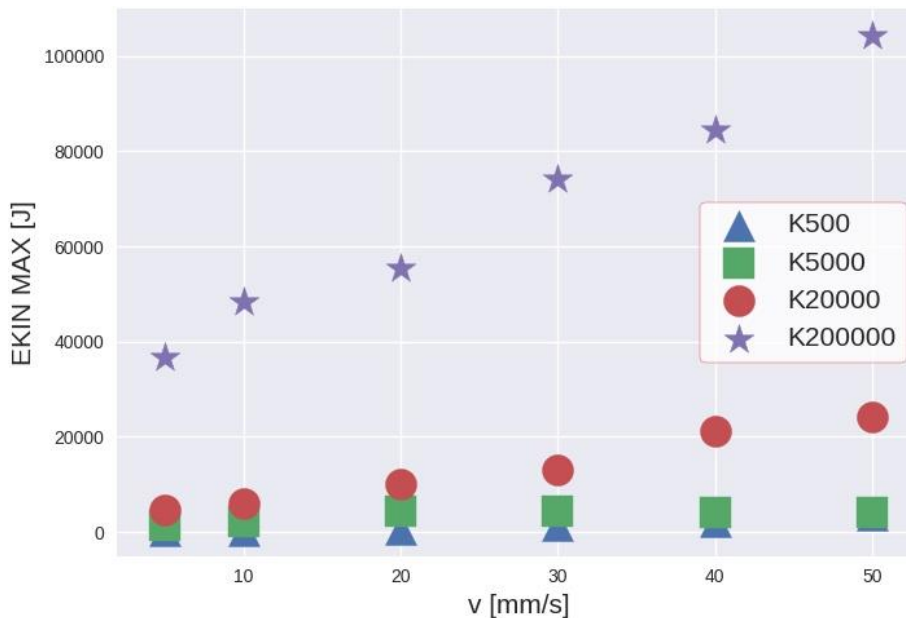
Fig. 45. The relationship between the maximum kinetic energy during the entire simulation and stretching velocity for different elastic stiffness of bonds.
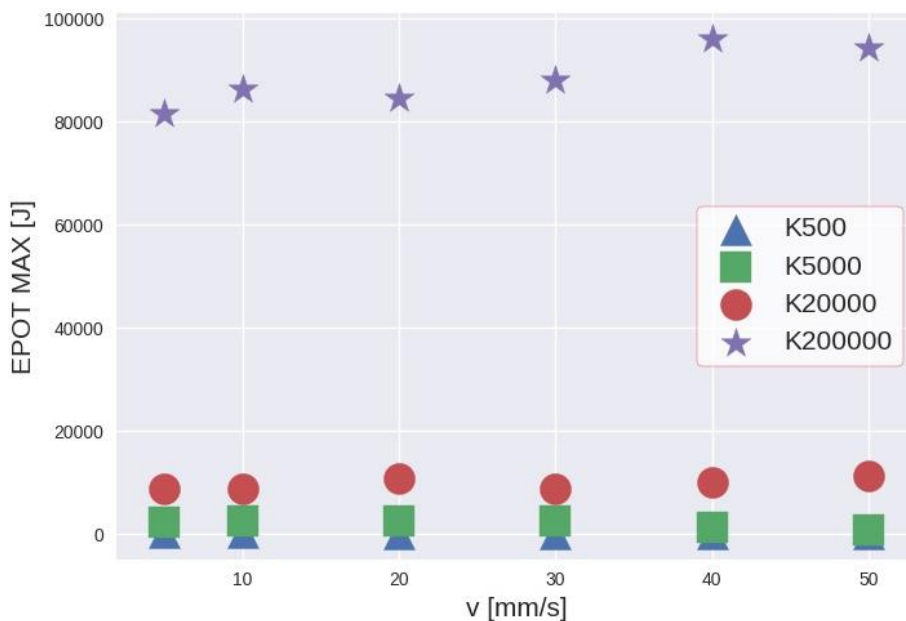
Fig. 46. The relationship between the maximum potential energy (of bonds) during the entire simulation and stretching velocity for different elastic stiffness of bonds.

4.4.4 Summary

In the presented research, numerous parameters related with uniaxial stretching of sample were investigated for different elastic stiffness of the bonds between particles and stretching velocity. It was possible to distinguish three different types of cracking for materials and the macroscopic Young's modulus of the whole sample and the maximum stress when the main crack occurs were calculated. Additionally, the relationship between the kinetic energy of particles due to linear movement, potential energy of bonds between particles, and the number of bonds between particles as a function of stretching velocity and elastic stiffness of the bonds were analysed.

4.5 Conclusions

DEM modelling was applied in this chapter to simulate fracturing of different materials during three basic material tests: uniaxial compression, Brazilian test and uniaxial stretching. This research was mainly related to analysis of parameters describing particles of the matter and bonds between them during a growing external load.

Considerations were started with probably the most common and popular material test – uniaxial compression. These simulations provided results in three groups of issues: dependencies between microscopic and macroscopic parameters of samples with different densities, as well as average potential energy of bonds and average kinetic energy of particles as a function of increasing external load. One of the clearest relationships between microscopic and macroscopic parameters was this between the microscopic Young's modulus and the macroscopic Young's modulus. A higher value of the first parameter corresponds very clearly to a higher value of the second parameter. Another conclusions came from the observation of a parameter such as cohesion. When keeping the remaining microscopic parameters fixed, the change in cohesion did not affect macroscopic parameters, Young's modulus and Poisson's ratio, or affects them slightly. For some of the results, the higher microscopic cohesion corresponds to the lower macroscopic Young's modulus. It was also concluded that the lower microscopic Poisson's ratio translates straightly into a higher macroscopic Young's modulus. Additionally, microscopic Poisson's ratio and tangent of the friction significantly affect macroscopic Poisson's ratio, while their influence on macroscopic Young's modulus is much weaker.

Interesting results were obtained when considering potentials energies of bonds as a function of external load. It appeared that the average percentage contribution of different potential energies of bonds to the average overall potential energy of bonds during the breaking process is always constant. Namely, the share of particular energies was 61% for the normal energy, 38% for shearing energy, bending energy and twisting energy were generally less than 1%. Similar analysis of average kinetic energies of particles in a function of external load was not as clear as in the case of potential energy of bonds. Results showed that linear kinetic energy prevails, ranging from about 80% to 96%. Within these data it was possible to distinguish two separated groups of results for which the ratio between linear kinetic energy and rotational kinetic energy was about 80% to 20% or about 94% to 6%. After a comparison with relevant microscopic parameters of bonds it appeared that the microscopic parameter of cohesion was responsible for these different ratios.

In the next step, the issue of Brazilian test was taken, popular geotechnical laboratory test for indirect measurement of tensile strength of materials. By performing these kind of numerical simulations a few goals were attended. The DEM method allowed a detailed monitoring of the internal microscopic state of a loaded sample including changes in particle kinetic and potential energies, to name a few. From the physical point of view, an insight was obtained into creation of the tensile crack under the simulated laboratory conditions. It was possible to monitor the

nucleation and temporal evolution of tensile crack which finally lead to breaking apart of Brazilian test samples. Following an evolution of the total kinetic and potential energies during loading, a few stages were identified in a response of the samples to constant speed loading. At the beginning of loading, the elastic response of the samples was clearly visible. During the intermediate loading, the samples exhibited a viscoelastic properties due to inducing particles dislocations. At the end of this stage, large dislocation occurring in block resulted in a visible plastic behaviour of the samples and finally lead to crack nucleation and breaking the sample apart.

Moreover, it was very interesting to observe how size of the used particles influenced each of the abovementioned stages. Although relatively small range of particle sizes was used, the obtained results clearly show that the stage most sensitive to the material composition was the intermediate loading stage when dislocations start to change the properties of materials and lead to a crack nucleation. On the other hand, the rather weak relationship of the critical strain and the strain when the crack fully breaks the sample into two pieces shows that this failure stage is rather insensitive to the material composition. However, it can be concluded that the most important result of the performed simulations was reporting of the scaling of the critical load that the sample could withstand as a function of the inverse of the size of the smallest particles building the sample.

The third and final stage of this part of the research were DEM simulations of uniaxial stretching. The performed simulations were related to a relatively simple mechanism of cracking of solids under the influence of uniaxial stretching force. A series of measurements were carried out with different stretching velocities. For each of them, the maximum value of stress when the main crack occurs was calculated. An interesting point was that the maximum stress weakly depends on elastic stiffness for smaller values of this parameter. In this range, the character of cracking seemed to be similar. However, for higher values of elastic stiffness there was a significant increase in the maximum value of stress. At the same time, for the same values of elastic stiffness different uniaxial stretching velocities weakly influenced the maximum stress. Additionally, due to analysing stress-strain curves, it was possible to distinguishe three different types of cracking: type I, when multicracking occurs and the cracking is dispersed in time; for this class of process it was impossible to extract the main breaking event at its specific time; type II, when dominating "macro-cracks" accompanied with smaller micro-cracks were developing; type III, when a single crack was created.

Furthermore, the kinetic energy and potential energy of the bonds were analysed. Two interesting issues could be observed. First, it was interesting to note that the peak of the kinetic energy occurred always for the same value of strain, and did not depend on stretching velocity or elastic stiffness of bonds. Second, the maximum value of potential energy strongly depended on elastic stiffness, but it did not depend very much on velocity. Another observation concerned an almost linear relationship between the maximum kinetic energy during entire simulation and stretching velocity, for different values of elastic stiffness of bonds. At the same time, the maximum potential energy was almost constant as a function of stretching velocity.

Summarizing, in this chapter there was presented the DEM modelling of different basic material tests. In laboratory conditions, such experiments are aimed at measurement of the characteristics and behaviour of different substances under various conditions. The data obtained in this way can be used in specifying the suitability of materials for various applications. However, not every aspect of the fracturing process can be analysed by experimental methods. The aim of this research was applying computer modelling to obtain a complementary data, not available experimentally. DEM models were created to study the microscopic aspects of fracturing, especially all issues connected with particles interactions, rotations and movements as a function

of external load. Performed simulations can be useful in predicting capabilities of the different structures and its intrinsic response to applied external load.

5. DISCRETE ELEMENT SIMULATIONS OF GLACIER CALVING

5.1 Introduction

DEM simulations presented in the previous part of the dissertation concerned the fracturing process of materials in a relatively small, laboratory scale (order of millimeters). Meanwhile, the second part of the dissertation is devoted to DEM simulations of real fracturing phenomenon – glacier calving. The motivation to take up this subject are current climate changes, which give a high priority to research on polar regions, particularly to glaciers. Application of numerical methods for uncovering the mysteries of glaciers is a quite new and promising approach.

The mass of glaciers and their thermal inertia are very large, so it takes many years to observe the effect of temperature changes on melting and retreating of glaciers (Schulson and Duval 2009; Timco and Frederking 1996; Timco and Weeks 2010). However, it turns out that the current scale of changes is unique in the scale of history. For instance, Strzelecki et al. (2018) presented the results of several years research on the coasts of Spitsbergen. It appeared that the forehead of concerned glacier retreated 1,600 meters compared to the 1930s and lost 60% of its area. Such processes have accelerated especially in the last 30 years. The accelerated pace of glaciers melting is one of the most important symptoms of current climate changes. The World Glacier Monitoring Service reported in 2013 (basing on data from 100 glaciers around the world) that the mass balance for all reference glaciers is constantly decreasing (The World Glacier Monitoring Service, https://wgms.ch). The mass loss of glaciers occurs due to various processes, among which one of the most significant is calving, still poorly understood.

The term "glacier calving" covers the wide range of processes through which intact chunks of ice are discharged to the seas and the oceans from the termini of glaciers or the margins of ice shelves (Benn et al. 2007a, Jania 1997). Examples of a water-terminating glaciers are presented in Figs. 47–49. Calving of such glaciers is normally caused by the expansion of the glacier, and it occurs as a sudden release and breaking away of a mass of ice from a forehead (Burgess et al. 2005, Jania 1997). The ice that breaks away can be classified as an iceberg, but may also be a growler, bergy bit, or a crevasse wall breakaway. Calving of glaciers is often accompanied by a loud cracking or booming sound before blocks of ice up to 60 meters high break loose and crash into the water. The entry of the ice into the water causes large, and often hazardous waves (Andrews 1985; Bahr 1996; Benn et al. 2007b; Chaplin 2016).

A detailed description of the mechanisms controlling the calving is essential for the reliable estimation and prediction of mass loss from glaciers. However, collecting the relevant data is a demanding task. On-site measurements are often difficult and dangerous (Górski 2014; Górski and Teisseyre 2006). The research used so far focused mainly on the satellite data, but the resolution of commonly available photos is relatively small, so, the quality of results is consequently low. Quite new and promising method is gathering the relevant information about glaciers by analysing signals, which are spread by glacier. Many various signals are associated with glaciers, and they result from internal, as well as external factors. Glaciers vibrate under the influence of external factors, such as wind, and the sound they emit is called the "singing" of glaciers. Analyzing "singing" can help monitor changes inside the glacier. Chaput et al. (2018) carried out detailed research on the Ross Ice Shelf. The ice vibrated differently when strong winds moved large amounts of snow or when the air temperatures on the surface grew or decreased, which influenced the speed of seismic waves moving in the snow. Analysis of these vibrations can give clues how the glacier reacts on the changing climate conditions, and changes in the "melody" may be a warning signal that the glacier is in danger of disintegration. Glaciers also emit signals due to the internal factors. Glowacki et al. (2015) contributed to the
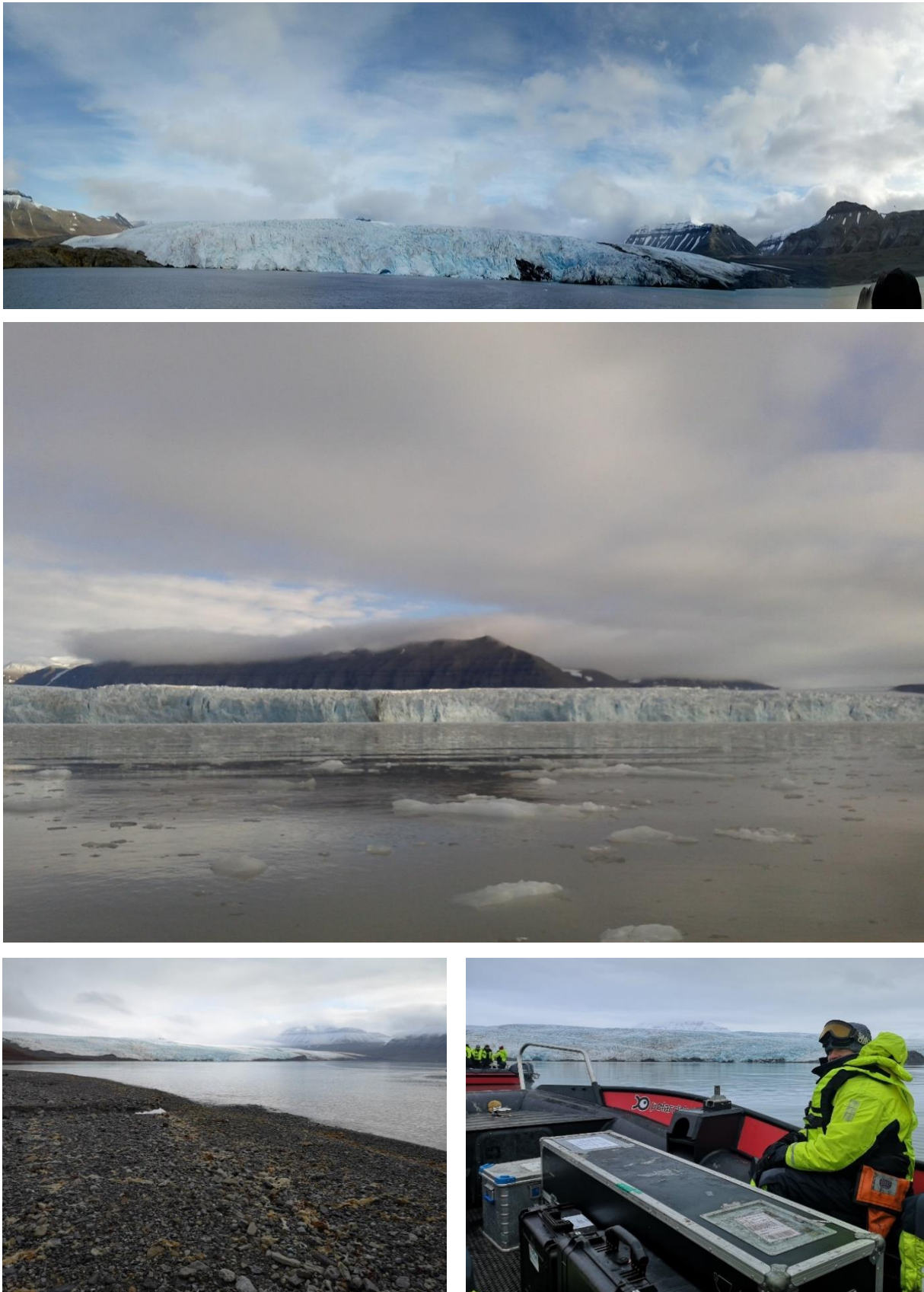
Fig. 47. Nordenskiöld Glacier and Tuna Glacier (in the middle), Spitsbergen. Photos by Piotr Klejment (top and middle) and Anders Stordal Fjeldsbø (bottom).

Fig. 48. Nordenskiöld Glacier, Spitsbergen. Photos by Anders Stordal Fjeldsbø.

Fig. 49. Nordenskiöld Glacier (bottom) and Tuna Glacier (top), Spitsbergen. Photos by Piotr Klejment (top) and Giuseppe Matera (bottom).

development of a new method of glacier mass loss estimation. It turns out that thanks to the analysis of underwater sounds associated with the calving of glaciers, it is possible to estimate how much ice was detached. A relatively simple method – recording the underwater sounds – can say not only when the glacier is calving, but also allows to discriminate different types of this phenomenon.

Motivated by abovementioned research, this chapter is devoted for describing the DEM application to glacier calving process. DEM was used to simulate fracturing of the glacier during calving, and then, to analyse signals propagating inside the glacier and in water after the fracturing occured.

In general, the DEM has a great potential in the area of glaciology. A model consisting of discrete particles fits ideally for simulating brittle behaviour of ice, especially in the case of glaciers (glacier calving, glaciers surging), icebergs, ice floe, etc. Numerical modelling offers a new approach to study the mentioned phenomena and can be a complementary tool for field and laboratory efforts in discovering the secrets of glaciers (Jarosch 2008, Gagliardini et al. 2013, Jouvet et al. 2011, Le Meur 2004; Zwinger and Moore 2009).

The history of DEM applications in glaciology is relatively short due to the heavy computational burden of this method (Nick et al. 2010). Most of the research papers on DEM appeared in recent several years, usually with two-dimensional approach. It is worth to mention a few of these papers. Robel (2017) analyzed thinning sea ice that weakens buttressing force of iceberg mélange. In this research a discrete element model was used to simulate explicitly mélange as a cohesive granular material. Åström et al. (2014) worked on termini of calving glaciers as self-organized critical systems. This work focuses on the discrete nature of calving and the understanding of the process itself. On the basis of the calving data obtained from small events on glaciers up to the size of ice-shelves, the authors give strong arguments that calving fronts behave as self-organized critical systems that switch from subcritical stable to supercritical calving modes. DEM was also used (Damsgaard et al. 2013) to model subglacial sediment deformation and to investigate the highly nonlinear dynamics of a granular bed when exposed to stress conditions comparable to those at the bed of warm-based glaciers. Herman (2016) proposed a discrete-element-bonded-particle sea ice model. In this model, sea ice was represented as an assemblage of objects of two types: disk-shaped "grains" and semi-elastic bonds connecting them. The grains move on the sea surface under the influence of forces from the atmosphere and the ocean, as well as interactions with surrounding grains. Riikilä (2017) used the DEM model to simulate various ice-specific applications with resulting flow rates that were compatible with Glen's law, and produced under fragmentation fragment-size distributions that agreed with the known analytical and experimental results. Riikilä et al. (2015) also developed simulations of calving of an ice block partially supported in water, which was similar to a grounded marine glacier terminus, and fracturing of an ice block on an inclined plane of varying basal friction, which could represent transition to fast flow or surging.

In comparison to the abovementioned research, the application of DEM to glaciology presented here is a little bit different. A numerical model, presented in this dissertation, represents the glacier's forehead and the water beneath it. Under the influence of the force of gravity, the fragment of the glacier took off and fell into the water. Various possible scenarios of such fracturing were explored when a block of different sizes fell to water from different heights. The whole process was tracked and recorded by a network of receivers placed in a water reservoir, as well as inside the glacier. The results obtained in this way allowed to describe the dependence between different scenarios of calving and resulting signal propagation in the water and inside the glacier.

5.2 Simulation settings

Simulating glacier behaviour requires a thorough knowledge of ice properties. From the numerical point of view, the insight into ice structure is necessary to know what simplifications should be adopted. Ice is an extremely complicated structure (Dobrowolski 1923; Hobbs 1974) and full 3D simulations of large-scale glacier including all parameters, for example, mechanical, thermal, electric, etc., are simply impossible. In fact, ice has 18 different crystal structures and three amorphous states (Chaplin 2016). The form that exists under the typical temperature and pressure conditions of glaciers and ice sheets is termed as ice Ih (Greve and Blatter 2009). The letter h stands for hexagonal because water molecules in this type of crystalline form are arranged in layers of hexagonal rings. The hexagonal plane is referred to as the basal plane and perpendicular to this plane is the optic axis or *c*-axis (see Fig. 50a).
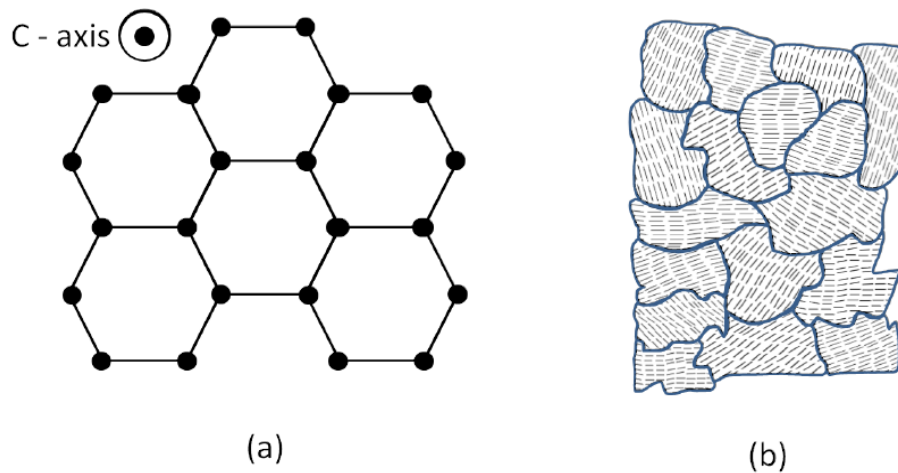

Fig. 50. Ice at different scales: (a) crystal hexagonal structure of ice Ih, and (b) polycrystalline ice formed from distinct ice crystals. In (a) the circles represent oxygen atoms of H_2O molecules, and in (b) the lines represent directions of *c*-axes (from Riikilä 2017).

The elastic and brittle properties of the hexagonal crystal structure are highly anisotropic (Jania 1997; Weeks and Assur 1967). Fortunately, large ice masses do not occur in single crystals but as an aggregate of them, i.e., as polycrystalline ice (Fig. 50b). Inside a single crystal of polycrystalline ice the *c*-axes are more or less oriented in the same direction (variations occur due to crystallographic defects) but in a large collection of randomly oriented crystals the anisotropy of single crystals is averaged out and the material becomes effectively isotropic (Walter et al. 2010; Cuffey and Paterson 2010; Glen 1955). The typical size of crystals or grains is in the submillimeter scale in freshly formed or highly deformed ice, to tens of centimeters in very old or slowly moving ice (Greve and Blatter 2009). In a glacier measured in hundreds of meters or kilometres, the isotropy assumption is well justified; hence, this assumption was adopted in presented DEM model.

Within the scope of this part of the work two main issues were undertaken: creation of a DEM model that can mimic a glacier calving and a measurement of parameters linked with this process, and, subsequently, an attempt to find a relationship between two parameters characterizing calving (the size of an ice block falling to the water and the height from which the fall occured) and accelerations of the glacier and water particles. Created DEM model consists of two blocks of particles. One block contains bonded particles and represents glacier. The second block consists of unbonded particles that undergo frictional interactions and represents water. The 2D cross-section of the model is presented in Fig. 51. Ice-like block of particles is 2 meters in depth, 10 meters in height, and maximally 45 meters in length. One of the dimensions is
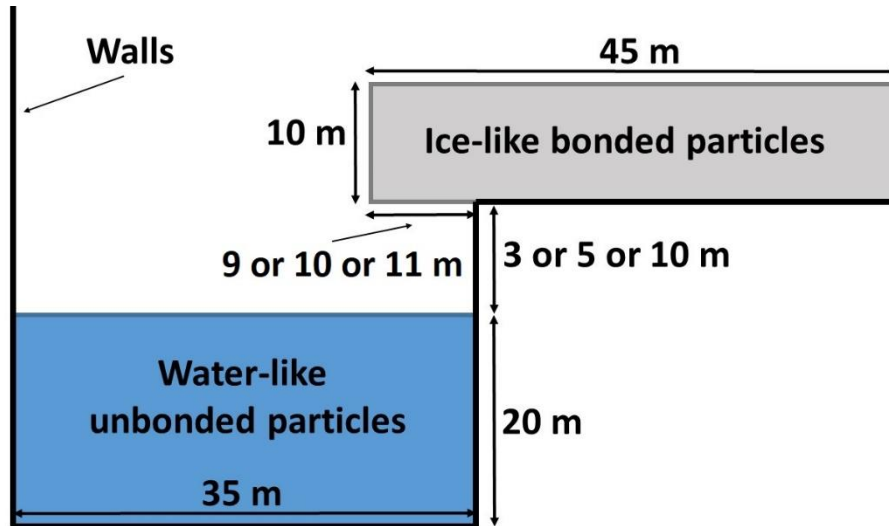
Fig. 51. The 2D cross-section of DEM model of calving glacier.

much smaller than the other dimensions; the idea underlying this simplification was to save computational time. The length of the glacier is changeable because the falling down part of the ice to the water could be 9, 10 or 11 meters long. The ice block that enters the water could have dimensions of 180 m^3 (9 m × 10 m × 2 m), 200 m^3 (10 m × 10 m × 2 m), or 220 m^3 (11 m × 10 m × 2 m). Water-like block of particles has dimensions of 35 m × 20 m × 2 m. Particles were connected by *BrittleBeamPrms* interaction, described wider in the Section 3.3.2.

The preparation of an appropriate model was complicated due to the fact that a glacier is not a uniform mass consisting of ice with the same properties, but is a mixture of different types of ice and snow. Glacial ice is a grain-shaped ice, which is the result of several transformations under the influence of the accumulation of successive layers of snow. Multiple melting leads to
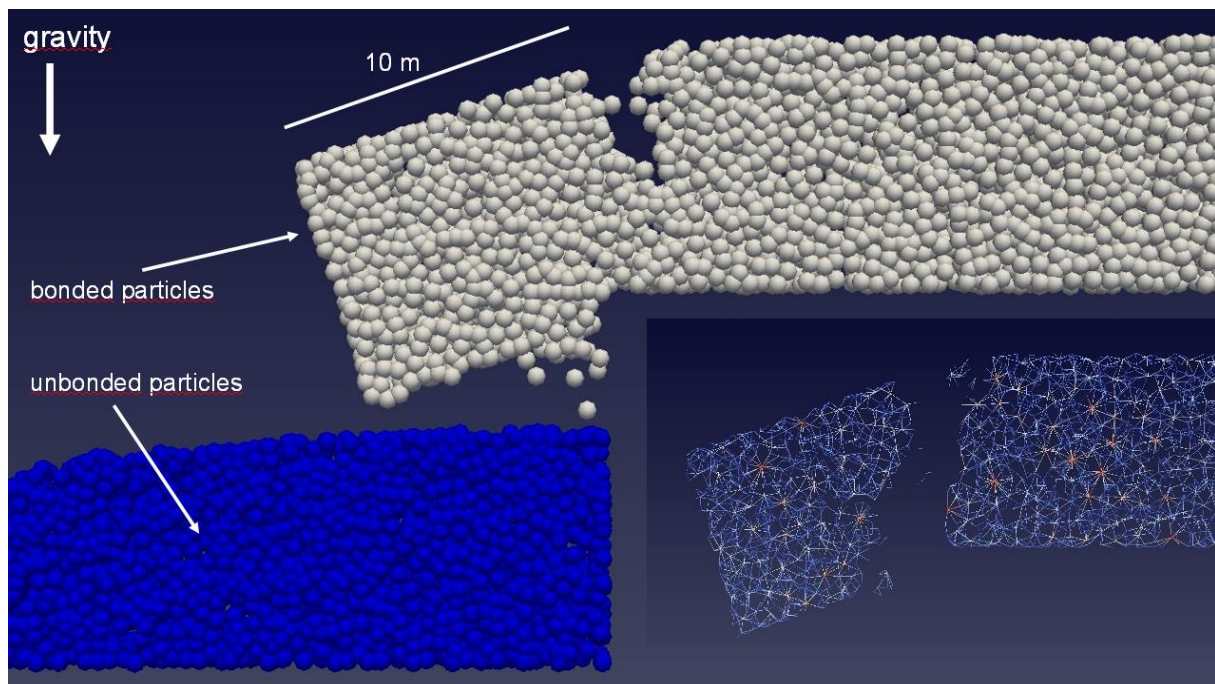
Fig. 52. Part of the glacier goes down due to gravity force – a snapshot from the simulation. In the right bottom corner – a view of breaking bonds.

a change in the structure of snow from fine crystalline (snowflakes) to "ice porridge", called a firn. Subsequent melting and freezing remove most of the air remaining between the ice grains, resulting in formation of the firn ice, much more dense than the density of snow. Under the influence of the weight generated by snow, the bottom layer of ice transforms into a blue ice made of large (up to a few centimetres in diameter) ice grains. Taking into account the above-mentioned information, some simplifications had to be adopted when choosing appropriate microscopic parameters for a DEM model.

The purpose of the presented research was not to test the properties or breaking process of ice itself, so the following simplifications have been made. Model parameters were selected to fulfil the three basic assumptions: to obtain the effect of brittle fracturing of the hanging part of the glacier under the influence of gravity; to obtain the effect of breaking into pieces of ice block during the contact with the water surface; and to prevent collapsing of glacier main body under influence of the gravity force (Fig. 52). The full set of parameters used in simulations is presented in Table 13.

Table 13

The set of parameters used during DEM glacier simulations

| Particles size	from 200 to 800 mm inside the glacier from 67 mm to 267 mm inside the water
Time step	dt = 1.0e-04 s
Time steps	time_steps = 2000000
Density of particles	940 kg/m^3 in a glacier 1000 kg/m^3 in a water
Type of bonds	
Name: *BrittleBeamPrms*	Parameters: youngsModulus = 1.0e+06, poissonsRatio = 0.25, cohesion = 1000.0, tanAngle = 1.0
Unbonded particles	
Name: *FrictionPrms*	Parameters: youngsModulus = 1.0e+06, poissonsRatio = 0.25, dynamicMu = 0.4, staticMu = 0.6
Elastic repulsion with the walls	
Name: *NRotElasticWallPrms*	Parameters: normalK = 1.0e+06
Translational and rotational viscous damping	
Name: *LinDampingPrms*	Parameters: viscosity = 0.002, maxIterations=50
Name: *RotDampingPrms*	Parameters: viscosity = 0.002, maxIterations = 50
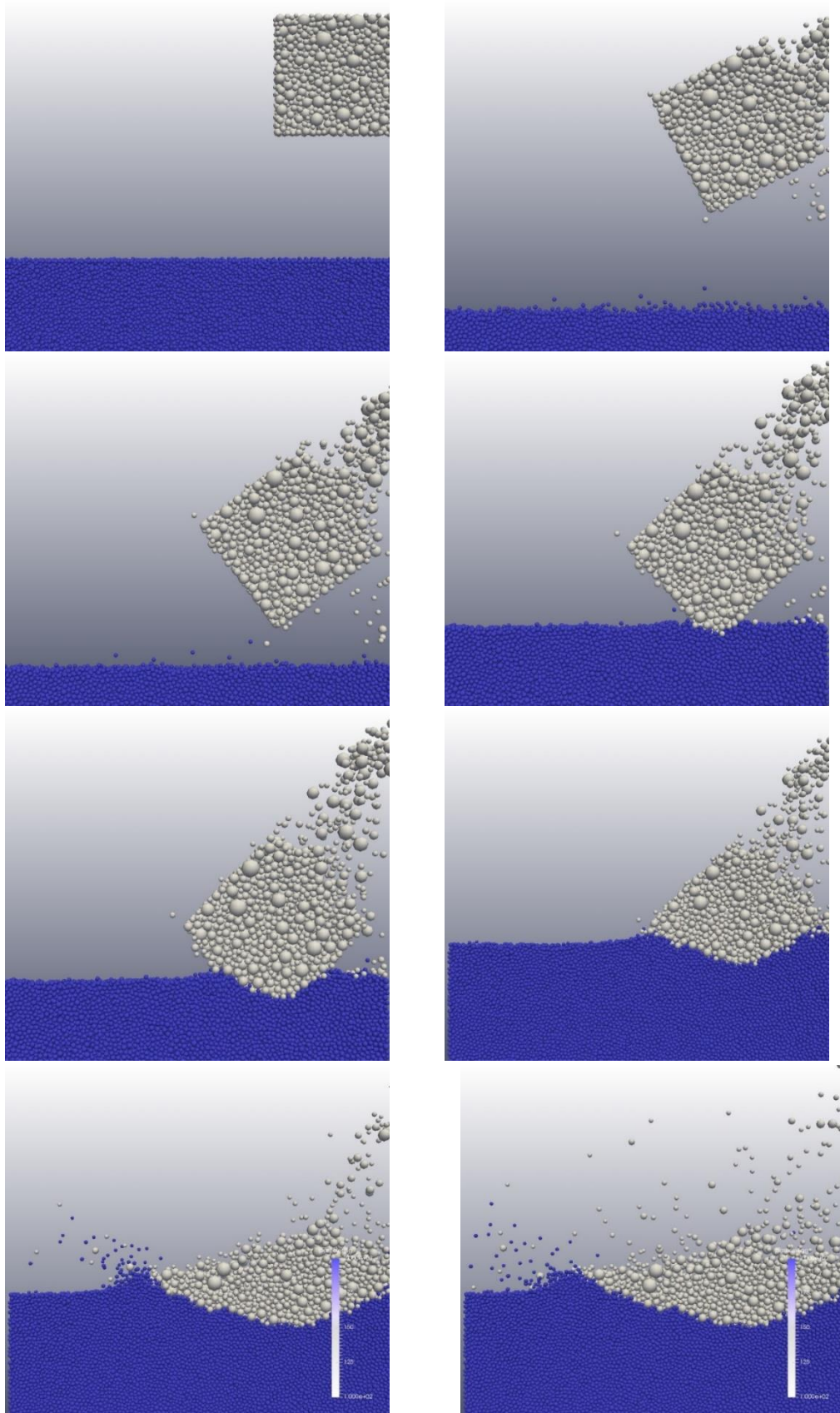
Fig. 53. Examples of the selected snapshots from the glacier calving process simulated with DEM. On the scale color means ice particles (white) or water partciles (blue).

An important limiting factor for the simulation was a computational time. Due to it, particles inside the modelled glacier were taken much bigger than in reality (several times), and particles creating the water were also large to reduce the number of particles involved in the simulation. As mentioned earlier, the parameters of bonds between glacier particles were chosen to obtain the effect of brittle fracturing. Very challenging issue was to imitate liquid (water) in the presented model. It has been decided to model the water below the glacier as a collection of unbonded particles. Very important property of fluids is a viscosity that characterizes their internal friction resulting from the shifting of fluid layers during the flow. In the presented model, viscosity was taken into account by applying frictional interactions between particles.

The selected snapshots of simulated calving process are presented in Fig. 53.

The aim of the presented simulations was the analysis of the calving process. For this purpose, some particles were selected as "receivers" and their accelerations along x-, y-, and z-axis were recorded. There were six receivers inside the water and four receivers inside the glacier (Fig. 54).
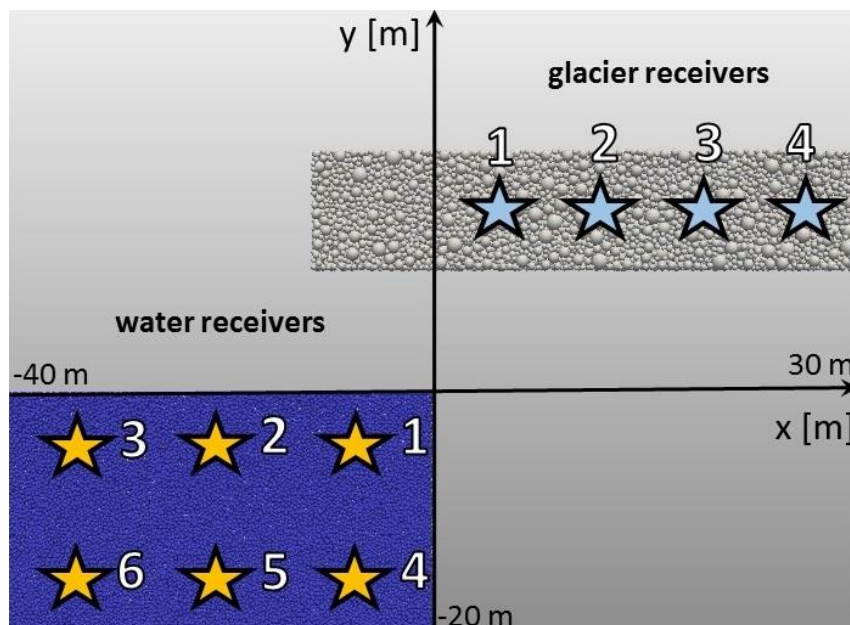
Fig. 54. Network of receivers during glacier calving simulations with receivers numbers (cross-section of the model).

The contact time (time when a falling down block of ice hits the surface of a water) of the height of 10 m was approximately 55 s; of 5 m, approximately 41 s; and of 3 m, approximately 36 s.

5.3 Simulations results

Results are divided into two main categories with respect to analysed signals, water-located receivers and glacier-located receivers.

5.3.1 Water-located receivers

This section includes data recorded by six receivers placed in water (see Fig. 54). Nine different combinations of parameters were analysed, for the volume of ice 180, 200, 220 m^3 falling down from height of 3, 5, and 10 m. On the basis of obtained results, it was attempted to draw conclusions about the characteristics of waves generated in water by falling mass.

Fig. 55. Simulated acoustic signals generated by 180 m^3 of ice falling from the height of 3 m: acceleration readings from receivers 1 to 6 placed in water.

Figure 55 shows the accelerations of the six receivers placed in the water, when 180 m^3 of ice falls from the height of 3 m. Receiver 1 has rerecorded high accelerations peaks around the impact time – just after the 36th second. Duration of the signal was approximately less than 10 seconds. Receiver 2 started to accelerate later than receiver 1. It has recorded the biggest acceleration between 55 and 110 second. Relatively long duration of these vibrations was probably caused by reflections of the waves inside the tank and their superposition, as experienced by receiver 2. Interestingly, receiver 3 noted only small disturbances during the whole simulation; probably, at this distance, signals have been already dumped. For the receivers placed in depths,

the results are as follows. Receiver 4, just below the place of impact, recorded rapid acceleration toward negative direction of the *x*-axis around the 40th second. This can be related to the wave propagation after the ice enters the water. Receiver 5 noted acceleration before the event on the surface; this may be the numerical result of preliminary movements of particles inside the tank. Receiver 6, in the left bottom corner of the tank, seems to be insensitive to external interference.

Fig. 56. Simulated acoustic signals generated by 200 m^3 of ice falling from the height of 3 m: acceleration readings from receivers 1 to 6 placed in water.

Figure 56 presents accelerations of the six receivers placed in the water, when 200 m^3 of ice falls from the height of 3 m. Because the only difference between these results and the previous ones lies in volume, the charts are similar. Receiver 1 noted accelerations just after the ice hit the water, and then it attenuates. Receiver 2 has accelerated significantly in the middle part of the simulation. Receiver 3 recorded acceleration at the end of the simulation. The first receiver in depths, receiver 4, accelerates around the moment of impact on the surface. Receivers 5 and 6 show farther propagation of the signal through the medium.
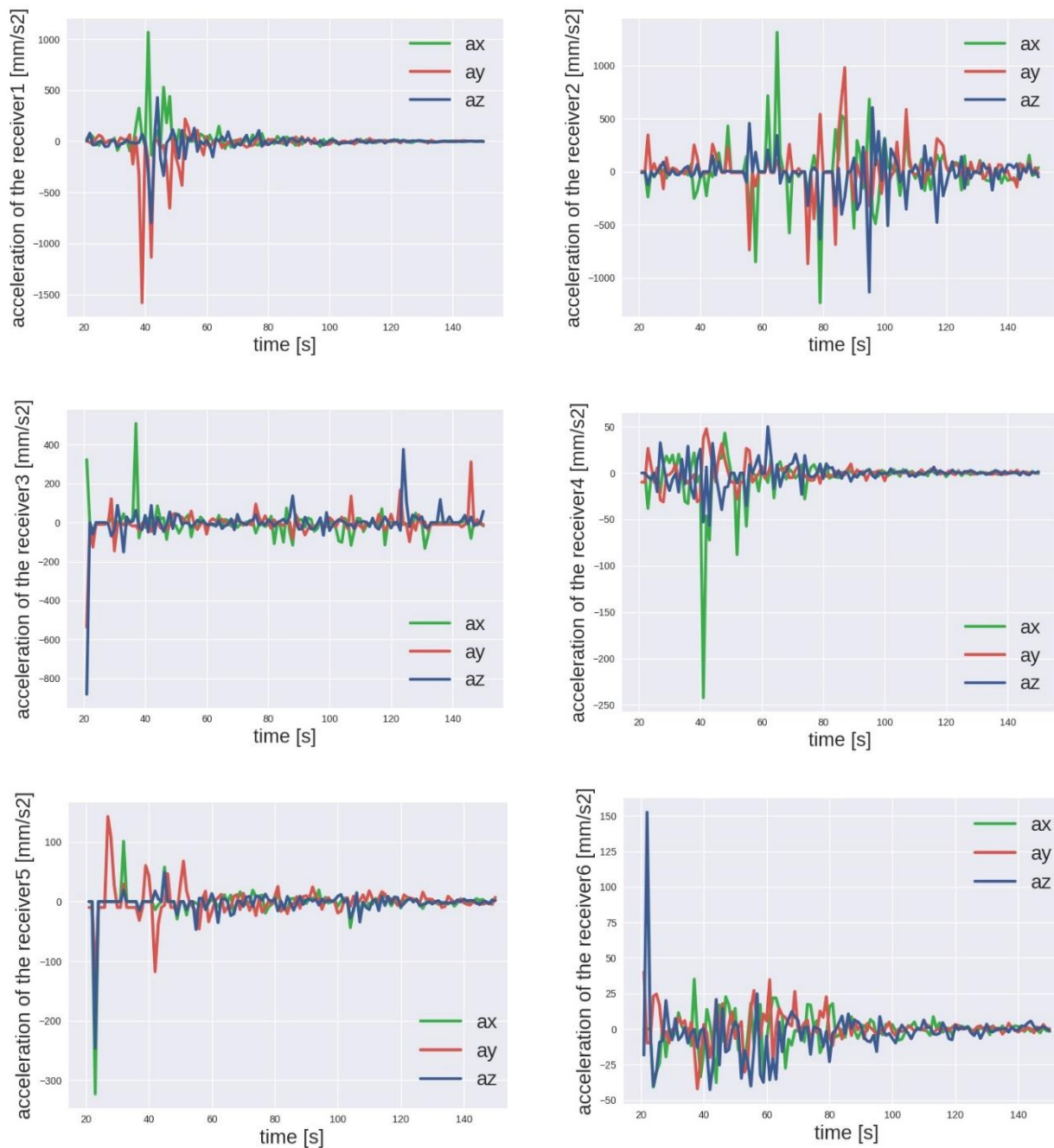

Fig. 57. Simulated acoustic signals generated by 220 m^3 of ice falling from the height of 3 m: acceleration readings from receivers 1 to 6 placed in water.

Figure 57 shows the accelerations of the six receivers placed in the water, when 220 m^3 of ice falls from the height of 3 m. Receiver 1 noted significant accelerations around the impact time. Receiver 2 begins to accelerate after the 40th second, and the high peak is visible around 80th second along the y- and the z-axis. It can be the result of interfering waves. Receiver 3 showed small acceleration around the 60th second, between the 90th and 120th second, and a significant peak in acceleration appears around the 140th second along the positive direction of the x-, y-, and z-axis. Receiver 4 noted significant accelerations after the event on the surface, which are visible after 40th second. Receiver 5 did not record accelerations when the ice hit the water surface. Receiver 6 recorded only one huge peak of acceleration after the 40th second, the impact time.
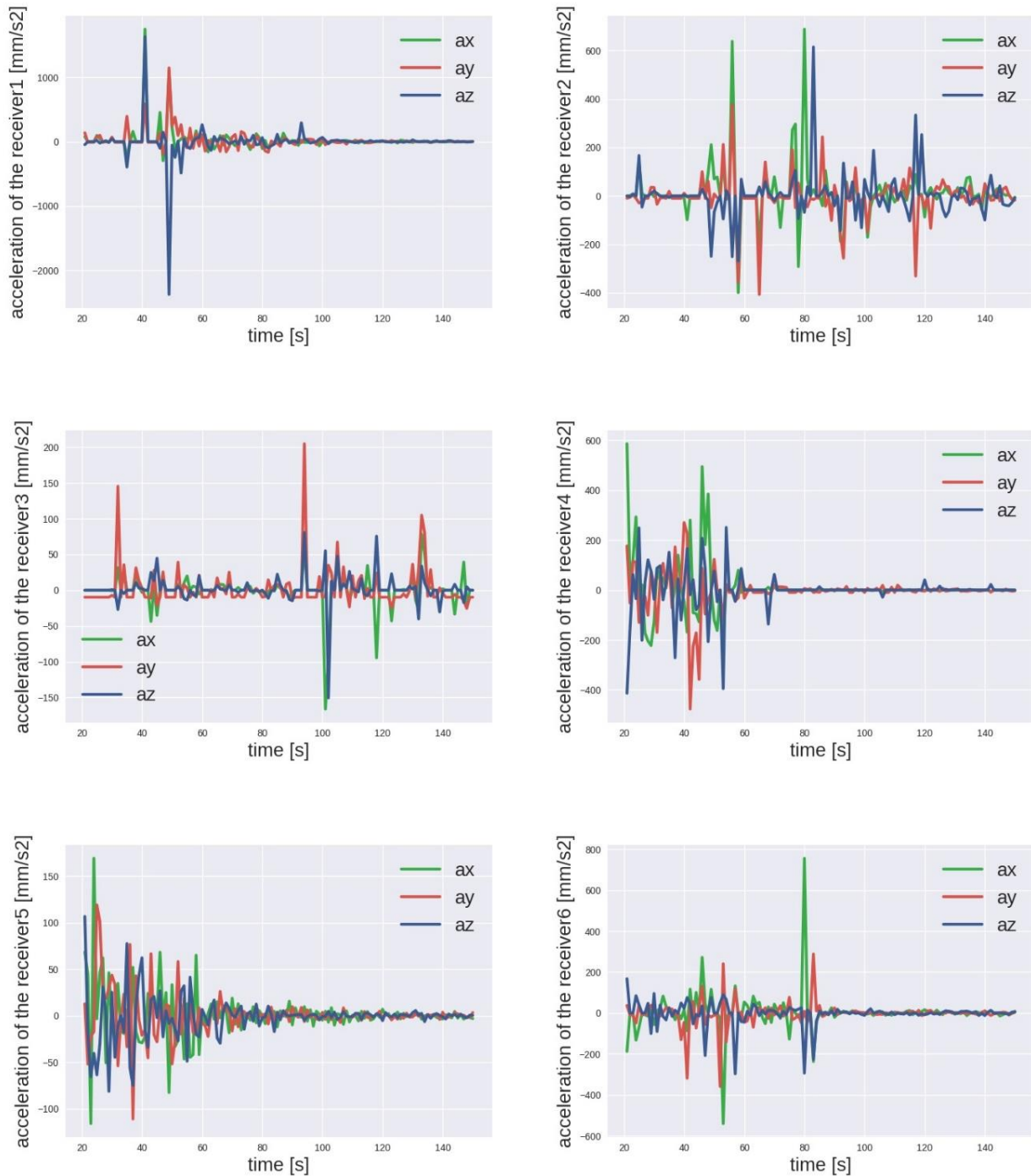

Fig. 58. Simulated acoustic signals generated by 180 m^3 of ice falling from the height of 5 m: acceleration readings from receivers 1 to 6 placed in water.

Figure 58 shows accelerations of the six receivers placed in the water, when 180 m^3 of ice falls from the height of 5 m. For this height – the falling ice hits the water after around 41 s. This moment is clearly visible on receiver 1. Receiver 2 noted huge acceleration in the middle part of the simulation; this was probably due to waves moving back and forth and superposing. Receiver 3 recorded small accelerations except a huge peak at the end of the simulation, for *z*-component (around 130th second). Receiver 4 in depths recorded accelerations around the 41st second, which then disappeared. Similar dependence is visible for the receiver 6, however, accelerations appeared later. Receivers 5 does not seem to depend on events on the surface.

Figure 59 shows the accelerations of the six receivers placed in the water, when 200 m^3 of ice falls from the height of 5 m. Receiver 1 clearly noted the impact moment, while receiver 2
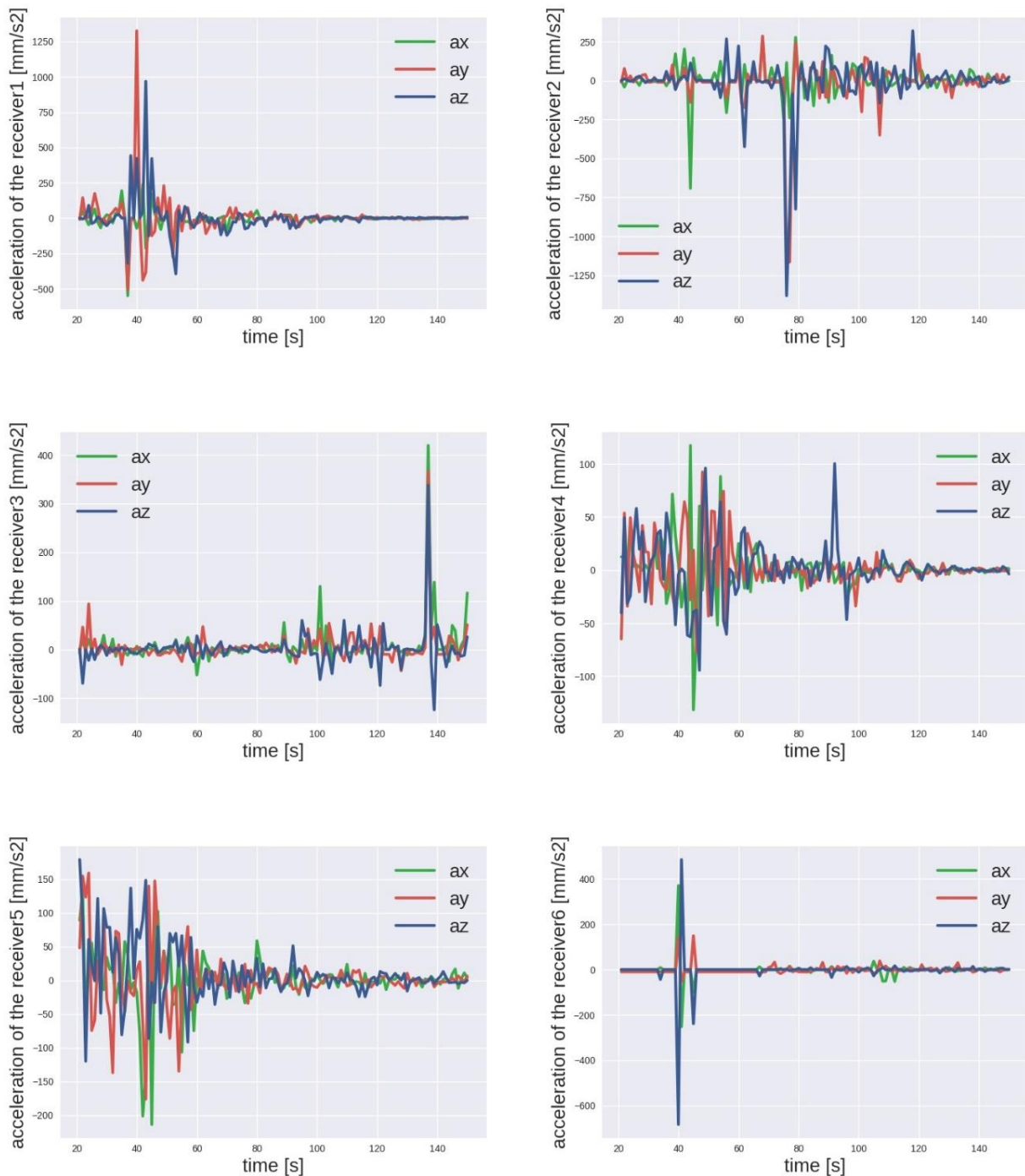

Fig. 59. Simulated acoustic signals generated by 200 m^3 of ice falling from the height of 5 m: acceleration readings from receivers 1 to 6 placed in water.

noted propagation of all waves through the surface. On receiver 3 accelerations appeared at the end of the simulation, after the 80th second, and are very irregular. Receiver 4 recorded considerable accelerations around the impact time. The oscillations that receivers 5 and 6 recorded are due to the influence of upper layers of particles.

Figure 60 shows the accelerations of the six receivers placed in the water, when 220 m^3 of ice falls from the height of 5 m. Results for this setup show a similar scheme as that for previous ones. Receiver 1 noted only the impact moment. Receiver 2 accelerates mostly in the middle part of the simulation. Receiver 3 accelerated significantly at the end of the simulation. Receiver 4 recorded strong motion from the beginning up to 120 s, and it covered accelerations due to the ice hit. A very similar result was noted for receiver 5. Receiver 6 shows similar peaks in acceleration like the receiver 1, which suggests it dependence on the surface event.

Fig. 60. Simulated acoustic signals generated by 220 m^3 of ice falling from the height of 5 m: acceleration readings from receivers 1–6 placed in water.
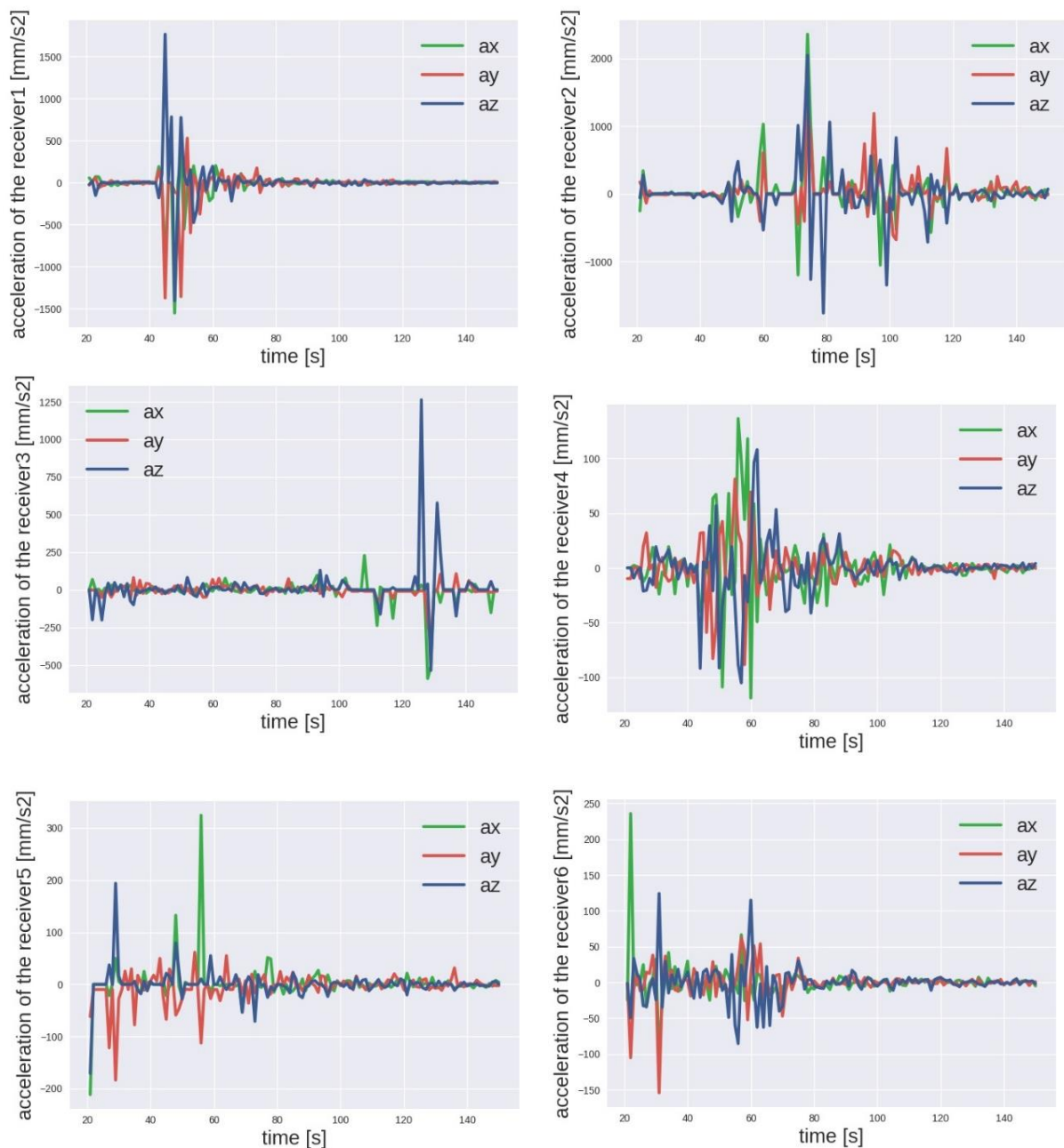
Fig. 61. Simulated acoustic signals generated by 180 m³ of ice falling from the height of 10 m: acceleration readings from receivers 1 to 6 placed in water.

Figure 61 shows the accelerations of the six receivers placed in the water, when 180 m³ of ice falls from the height of 10 m. Receiver 1 noted exactly the moment of impact, around the 55th second. The accelerations then attenuate. Receiver 2 accelerated according to all waves propagation through the tank during the simulation, back and forth, especially their superpositions. Receiver 3 shows no movements up to the end of the simulation, i.e., after the 120th second. Receiver 4 accelerates mostly around the 60th second; this suggests a link with the surface event. Receiver 6 also shows a similar result.

Figure 62 shows the accelerations of the six receivers placed in the water, when 200 m³ of ice falls from the height of 10 m. Receiver 1 accelerates exactly at the moment of the impact. For receiver 2, accelerations appeared in the middle of the simulation, while for receiver 3, it appeared at the end. Receiver 4 shows significant acceleration around the 60th second, which
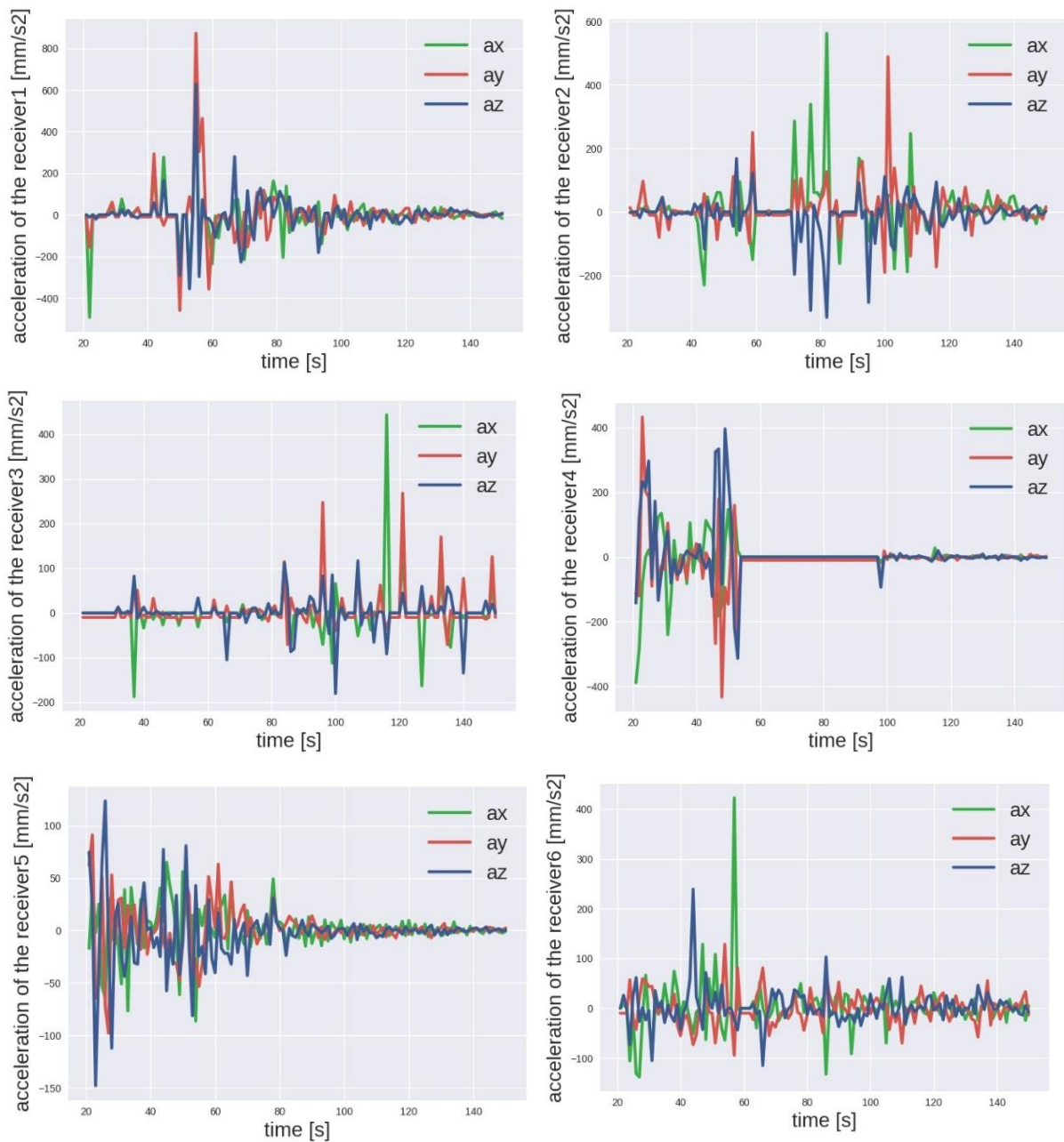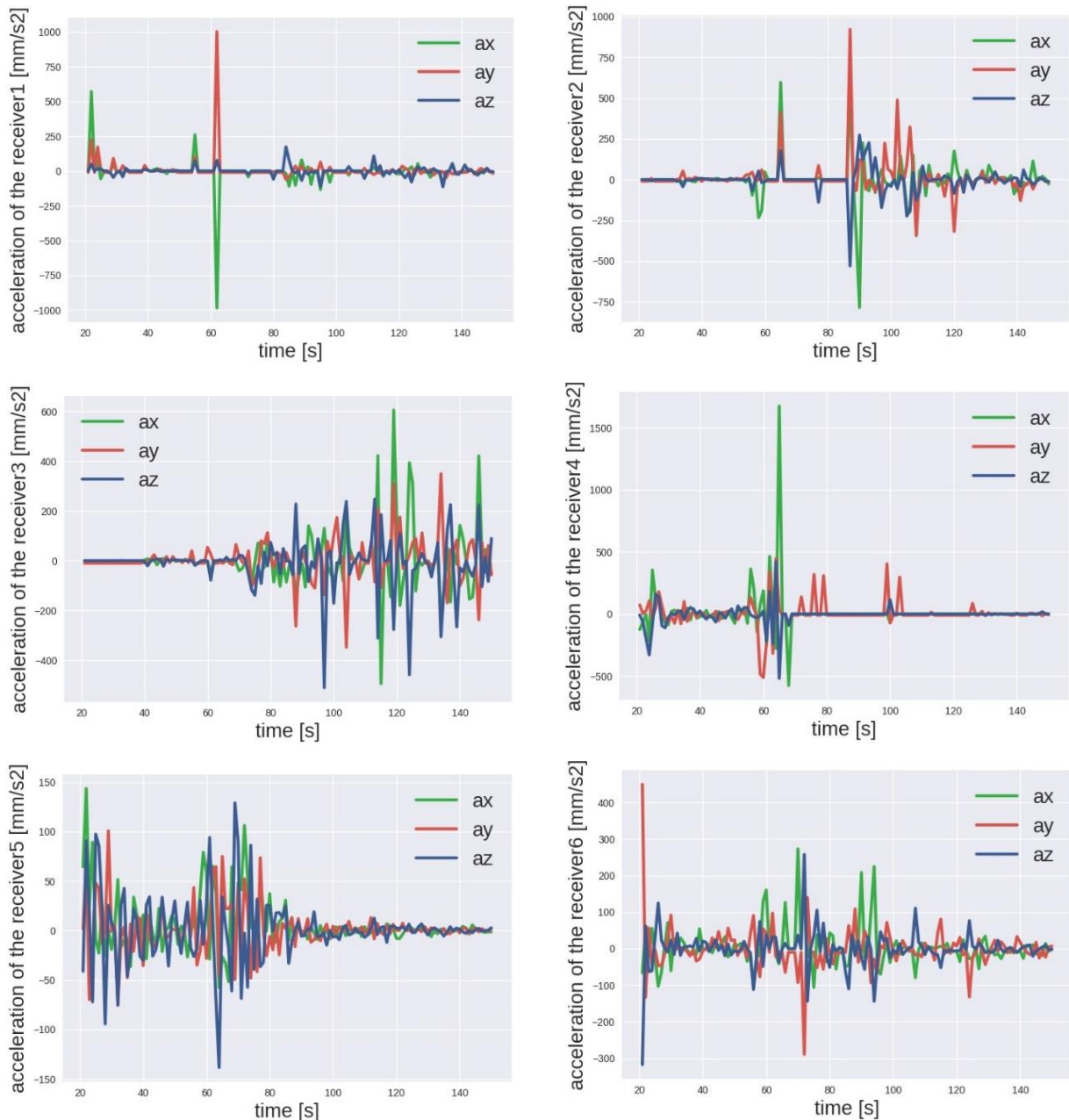
Fig. 62. Simulated acoustic signals generated by 200 m^3 of ice falling from the height of 10 m: acceleration readings from receivers 1 to 6 placed in water.

should be linked with the ice hitting the water. Receivers 5 and 6 also vibrate after the 50th second, probably due to reflected waves.

Figure 63 shows the accelerations of the six receivers placed in the water, when 220 m^3 of ice falls from the height of 10 m. The last part of the results corresponds to the biggest block of ice falling down from the biggest height. Receiver 1 experienced the moment of impact very significantly. Interestingly, repeated high accelerations appear on the receiver 4 just after oscillations on the receiver 1. Receiver 2 shows oscillations in the middle of the simulation and receiver 3, at the end. Receiver 5 and 6 noted considerable accelerations for approximately 50 s, and it seemed to depend on the surface event.

To summarize all the results, the selected characteristics of recorded signals are gathered in Table 14. For different values of height and ice volume, the maximum and minimum
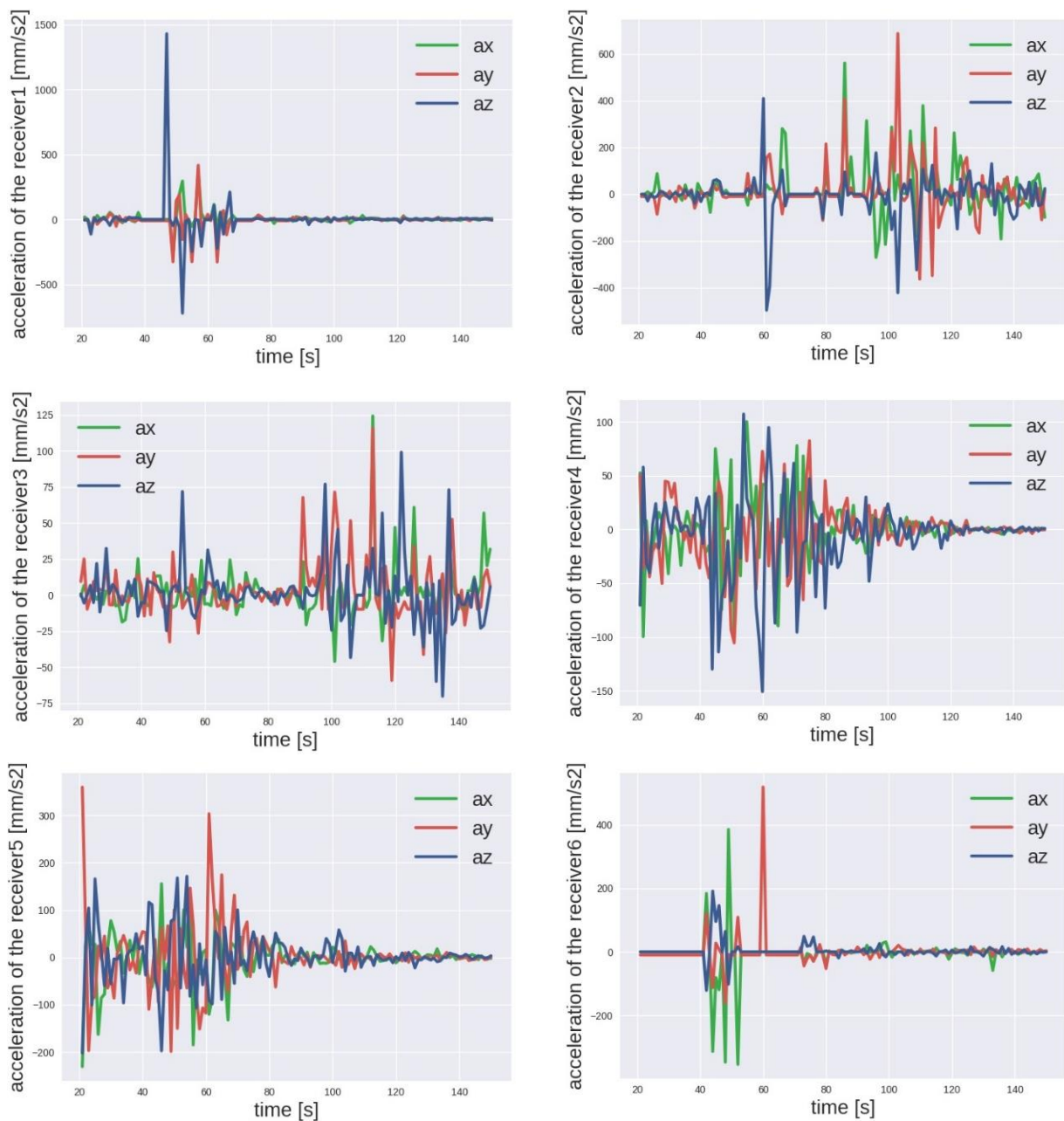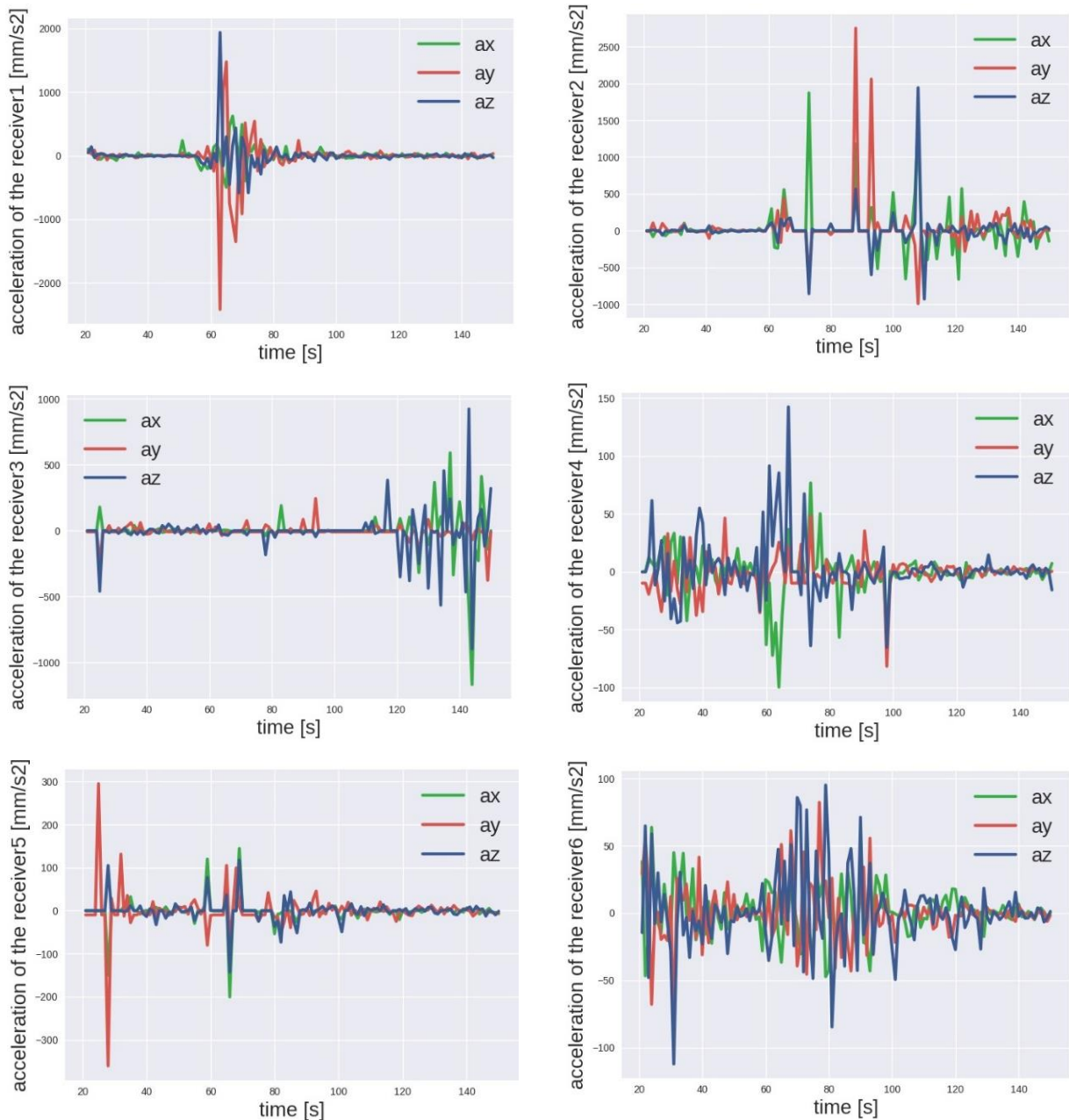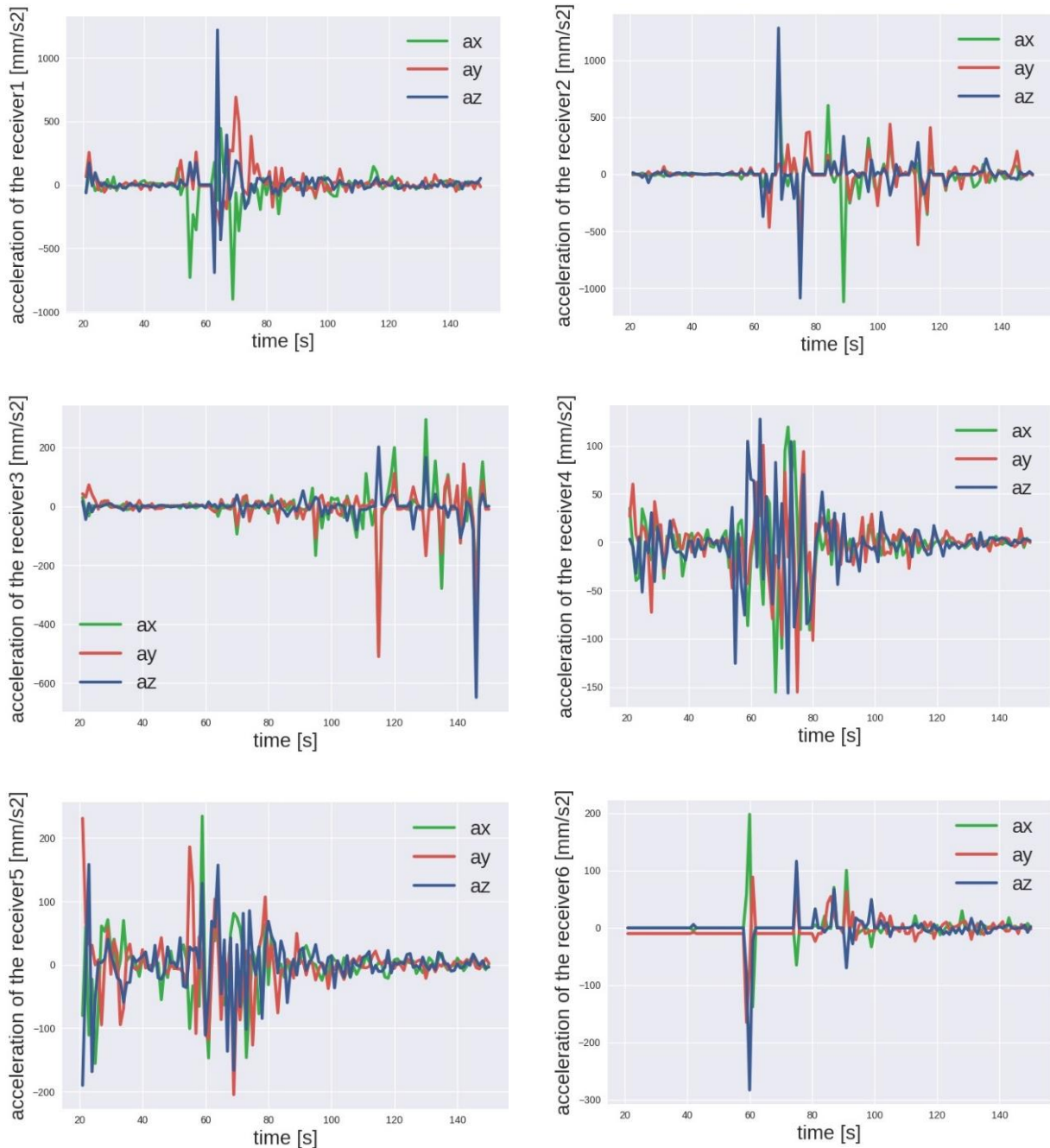
Fig. 63. Simulated acoustic signals generated by 220 m^3 of ice falling from the height of 10 m: acceleration readings from receivers 1 to 6 placed in water.

values of acceleration during the whole simulation (regardless of direction) and the approximate time of the main peak are shown.

Finally, it can be concluded that along the surface, acceleration recorded by receivers quickly decreases with distance, while for receivers in depth, there is no straightforward dependence. Moreover, larger volume of ice falling down to the water causes smaller acceleration of water particles or this acceleration does not depend on the volume (however, this is true only for the surface receivers; receivers in depth are not sensitive to volume parameter). It may seem that an opposite relationship should occur – in fact, the conducted simulations showed another dependence. What is interesting, there is no direct relationship between the acceleration of wa-

Table 14

Summary of acceleration readings during glacier calving simulations
for receivers placed in water

Receivers in water – acceleration								
Volume 180 m³			Volume 200 m³			Volume 220 m³		
Receiver number	Acceleration range [mm/s²]	Time of main event [s]	Receiver number	Acceleration range [mm/s²]	Time of main event [s]	Receiver number	Acceleration range [mm/s²]	Time of main event [s]
height of 3 meters								
R1	−1500 to 1000	37–50	R1	−2000 to 1000	35–60	R1	−500 to 1250	35–60
R2	−1000 to 1000	X	R2	−400 to 600	45–120	R2	−1250 to 250	35–120
R3	−800 to 500	X	R3	−150 to 200	90–130	R3	−100 to 400	90–140
R4	−250 to 50	20–80	R4	−400 to 500	20–60	R4	−120 to 100	20–100
R5	−300 to 100	20–60	R5	−100 to 150	20–60	R5	−200 to 150	20–60
R6	−50 to 150	20–80	R6	−600 to 800	20–85	R6	−600 to 400	40–45
height of 5 meters								
R1	−1500 to 1500	40–60	R1	−400 to 800	40–80	R1	−700 to 1500	45–70
R2	−1500 to 2000	50–120	R2	−300 to 600	70–110	R2	−500 to 600	55–120
R3	−500 to 1250	110–140	R3	−200 to 400	80–140	R3	−75 to 125	90–150
R4	−100 to 150	40–70	R4	−400 to 400	20–55	R4	−150 to 100	20–100
R5	−200 to 300	20–60	R5	−150 to 150	20–80	R5	−200 to 400	20–80
R6	−150 to 250	20–70	R6	−150 to 400	40–60	R6	−300 to 500	40–60
height of 10 meters								
R1	−2500 to 2000	60–80	R1	−1000 to 1000	60–62	R1	−1000 to 1000	50–80
R2	−1000 to 2500	60–120	R2	−750 to 1000	90–120	R2	−1000 to 1000	60–120
R3	−1200 to 1000	120–150	R3	−500 to 600	90–150	R3	−600 to 300	100–150
R4	−100 to 150	55–100	R4	−500 to 1500	55–70	R4	−150 to 200	50–90
R5	−300 to 300	30–70	R5	−150 to 150	20–80	R5	−200 to 200	50–90
R6	−120 to 100	60–100	R6	−300 to 400	50–100	R6	−300 to 200	60

ter particles and the height from which the ice block falls. Obviously, it can also noted that along the surface, the longer the distance, the bigger the time when the main shockwave comes. However, the result is completely different for receivers in the depth. Their times are almost the same as times noted by receiver 1.

5.3.2 Glacier-located receivers

This section includes data recorded by four receivers placed in the glacier (see Fig. 54). Three different combinations of parameters were analysed, for volumes of ice 180, 200, and 220 m^3 falling down from the height of 5 m. On the basis of the obtained results, it was attempted to draw conclusions about the characteristics of waves travelling through the solid medium.

Figure 64 presents the accelerations of the four receivers placed in the glacier, when 180 m^3 of ice falls from the height of 5 m. The moment of impact for falling down from the height of 5 m is approximately 41 s. The period of intensified accelerations for receiver 1 appears before 40 s, it then attenuates and disappears. Receiver 2 starts to accelerate with some delay (after the 30th second); however, vibrations for this receiver are longer. A similar pattern can be observed for receivers 3 (after the 40th second) and 4 (after the 60th second).

Fig. 64. Simulated acoustic signals generated by 180 m^3 of ice falling from the height of 5 m: acceleration readings from receivers 1 to 4 placed in glacier.

Figure 65 presents the accelerations of the four receivers placed in the glacier, when 200 m^3 of ice falls from the height of 5 m. Receiver 1 starts to accelerate around the 10th second, the maximum period is between the 30th second and the 70th second, and the vibrations then decrease. Receiver 2 accelerates from the 20th second; vibrations are the greatest, up to the 80th second, and then, they are smaller, but not considerably. The same pattern was recorded by the receiver 3 with accelerations starting at the 40th second. Interestingly, changes can be observed for receiver 4 with negative accelerations between the 30th and 40th seconds and positive accelerations between the 50th and 60th seconds.

Fig. 65. Simulated acoustic signals generated by 200 m^3 of ice falling from the height of 5 m: acceleration readings from receivers 1 to 4 placed in glacier.

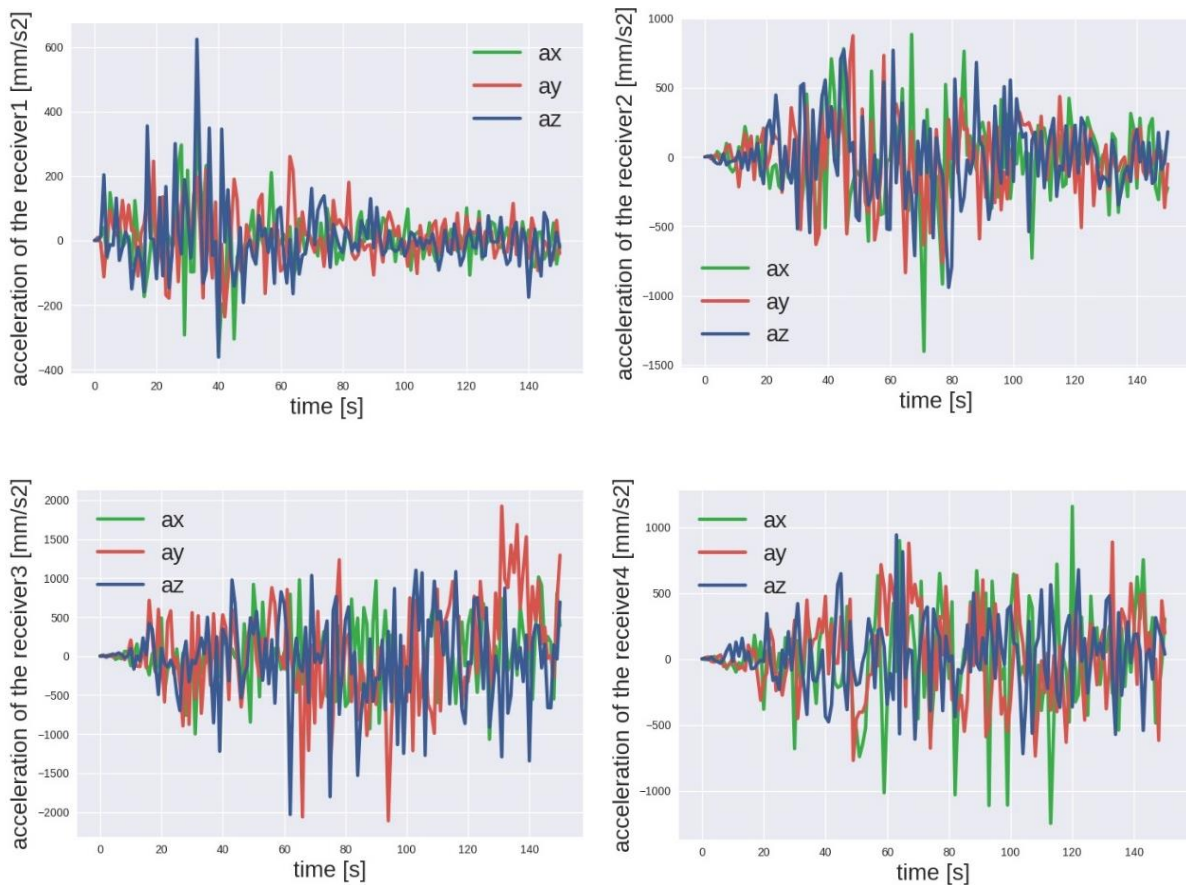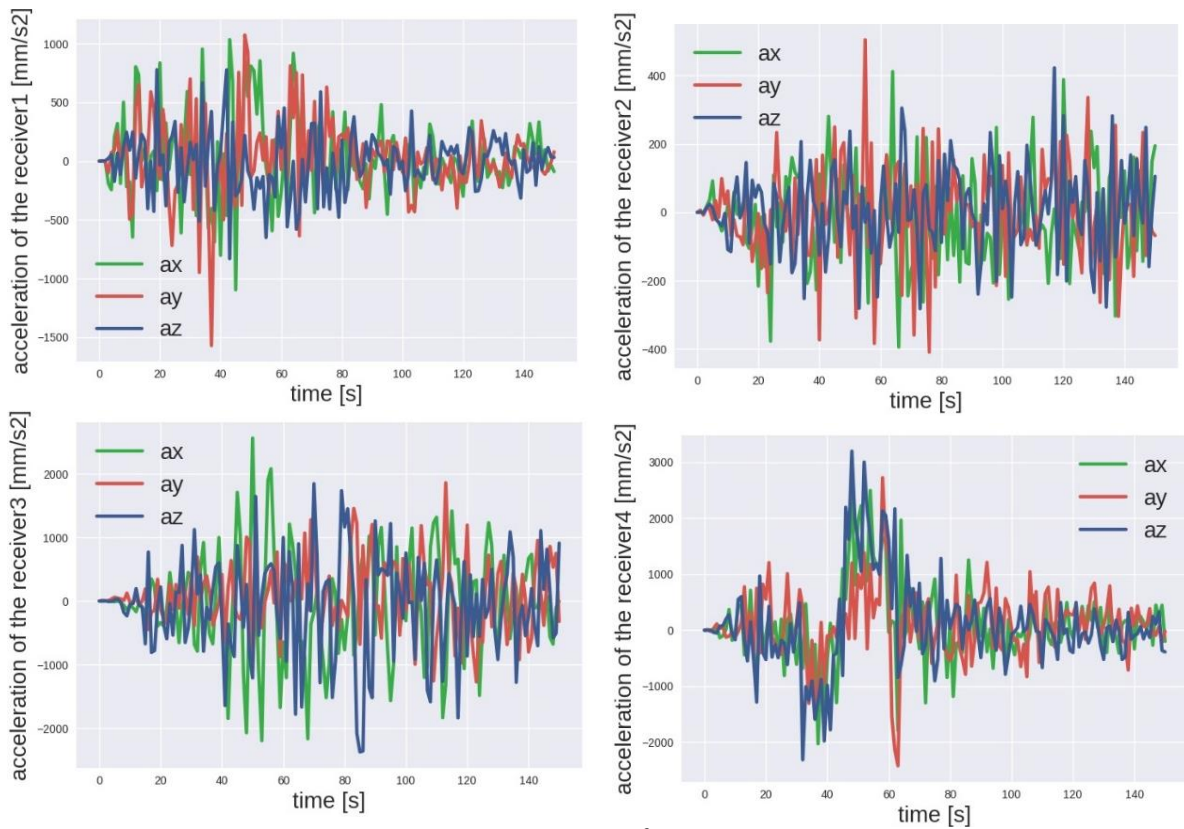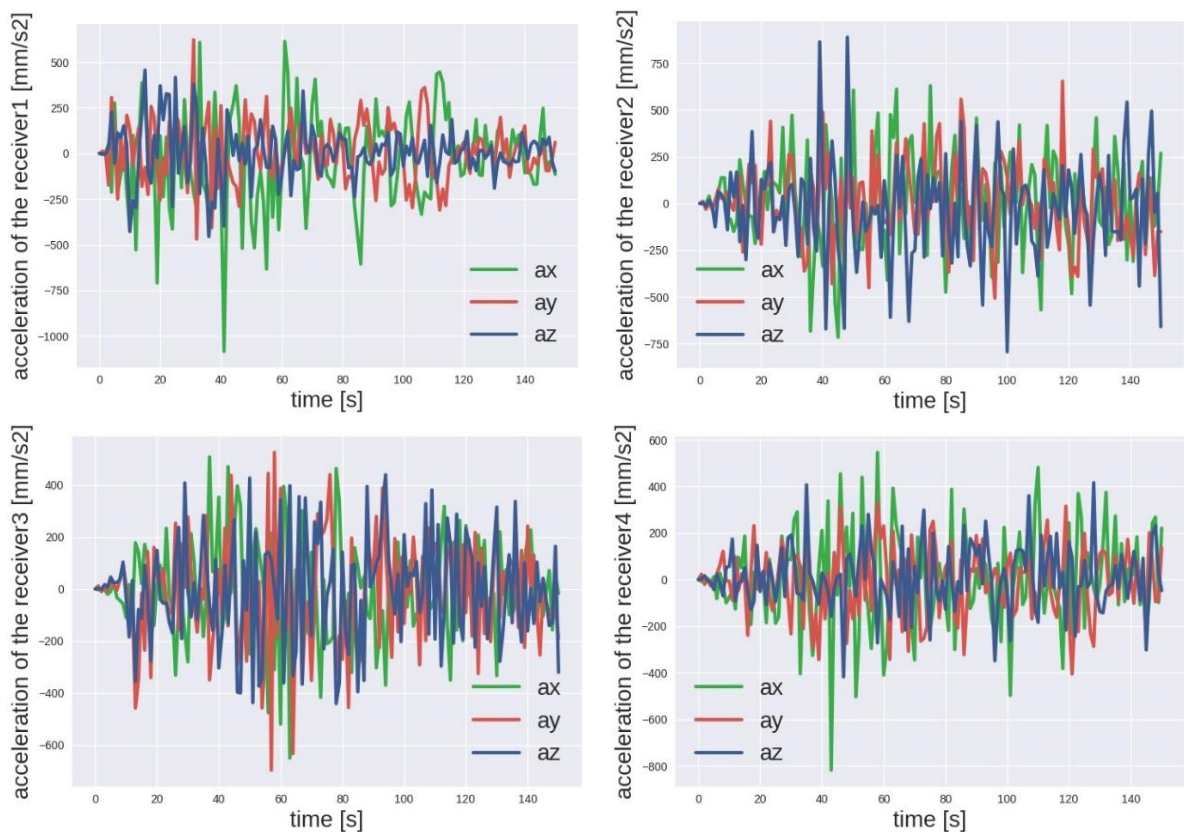Fig. 66. Simulated acoustic signals generated by 220 m^3 of ice falling from the height of 5 m: acceleration readings from receivers 1 to 4 placed in glacier.

Figure 66 presents the accelerations of the four receivers placed in the glacier, when 220 m³ of ice falls from the height of 5 m. The pattern from previous results is repeated for all receivers, that is, receivers start to accelerate with some delay related to the distance from the place of fracturing. Then, these motions have a similar size or attenuate. Receiver 1 starts to accelerate after the 5th second, and the maximum acceleration is up to the 120th second. For receiver 2, the acceleration begins around 30th second, and this result is similar for receivers 3 and 4. Within the simulation time, the recorded signals visibly attenuate for the receiver 1 while still remain large for other ones.

To summarize, the selected characteristics of recorded signals are gathered in Table 15. The maximum and minimum values of acceleration during all the simulations (regardless of direction) are shown for different values of the height and ice volume.

Table 15

Summary of acceleration readings during glacier calving simulations
for receivers placed in glacier

Receivers in glacier – acceleration					
Volume 180 m³		Volume 200 m³		Volume 220 m³	
Receiver number	Acceleration range [mm/s²]	Receiver number	Acceleration range [mm/s²]	Receiver number	Acceleration range [mm/s²]
R1	–400 to 600	R1	–1500 to 1000	R1	–1000 to 500
R2	–1500 to 1000	R2	–400 to 500	R2	–750 to 750
R3	–2000 to 2000	R3	–2000 to 2500	R3	–600 to 500
R4	–200 to 0	R4	–2000 to 3000	R4	–800 to 600

(height of 5 m)

Signals recorded inside the glacier do not depend directly on the size of breaking apart block of ice and do not depend even on the distance from the place of fracturing.

5.4 Conclusions

In this chapter, DEM simulations of glacier calving phenomena have been presented. The DEM model of a calving glacier was created, which consists of two blocks of particles. One block, with bonded particles, simulates glacier. The other one, with unbonded particles, simulates water.

Presented model is highly simplified. Some simplifications are introduced to save the computational time (size of particles, size of the model), while others are a consequence of software limitations (only mechanical properties of the material are considered). Additionally, nature and physics of the ice are so complex that the current computer models are unable to consider all mechanical, thermal, electrical and optical properties simultaneously. Because of the limited time during PhD studies, it was not possible to compare our data with measurements carried out close to the real glaciers.

Despite all the simplifications, some interesting conclusions have been drawn. Along the surface, acceleration recorded by receivers quickly decreases with distance, while for receivers in the depth, there is no straightforward dependence. Moreover, larger volume of ice falling down to the water causes smaller acceleration of water particles or this acceleration does not depend on the volume (however, only for the surface receivers, receivers in depth are not sensitive to volume parameter). What is interesting, there is no direct relationship between the acceleration of water particles and the height from which the ice block falls. It can also be noted that along the surface, the longer the distance, the bigger the time when the main shockwave

comes. However, the result is completely different for receivers in the depth. Their times are almost the same as the times noted by receiver 1.

Furthermore, the general patterns were found related to movements of the particles for all heights and sizes of the block of ice. Considering receivers in the water, it was observed that receiver 1 accelerates exactly at the moment of impact and then accelerations always disappear. Receiver 4 just below the receiver 1, but close to the bottom, also accelerates just after the impact. In contrast, receivers 5 and 6, which are also close to the bottom, show mostly accelerations related to movements of the particles due to the gravitational force. Receiver 2, in the centre of the tank and close to the surface, accelerates in the middle period of the simulation. This seems to be a result of wave superposition, which moves back and forth inside the tank. Receiver 3 accelerates only at the end of the simulation. Patterns for the receivers in the glacier are more difficult to describe. However, it was observed that oscillations in acceleration start with delay related to the distance between the receiver and the place of cracking.

The model consisting of discrete particles seems to fit ideally for simulating behaviour of ice. In the presented research, DEM model of calving glacier was prepared and this process was analysed thanks to the network of receivers. It was not possible to discover clear relationships between parameters related to calving (ice block size, falling height); however, some extensive information about waves propagation in the water and in the glacier were gained.

6. SUMMARY AND CONCLUSIONS

In a DEM model, loads and deformations can be applied to virtual samples to simulate physical laboratory tests, and the particle scale mechanism that underlies the complex overall material response can be monitored and analyzed. In a DEM model the evolution of the contact forces, the particle and contact orientations, the particle rotations, etc., can be easily measured. It is incredibly difficult (and arguably impossible) to access all this information in a physical laboratory test. The DEM model allows to look inside the material and to understand the fundamental particle interactions underlying the complex, macro-scale response. To date knowledge of brittle material response has relied largely on empirical observations of the overall material response in laboratory tests. DEM simulations thus present a valuable set of tools to complement existing techniques and, as a result, DEM has a potential to be an essential tool in basic research in geomechanics.

Summarizing all parts of the work, an insight into the process of material cracking was made. The DEM allows to obtain innovative results, such as describing the cracking process from the point of view of individual grains, and their displacements, velocity, acceleration and energy. In DEM, even if simple numerical models are used to simulate the inter-particle contacts, and ideal, approximate, particle geometries are used, many of the mechanical response features associated with the material can be captured. Simplifying the particle shapes (e.g. using spheres) and adopting very basic models of the contact response reduce the computational cost of the simulation and thus allow systems involving relatively large numbers of particles to be analyzed while still capturing the salient response characteristics of material behavior.

The results were presented in two chapters. The first one described numerical simulations of materials tests: uniaxial compression, Brazilian test, and uniaxial stretching. The analysis of the fracturing process was carried out for all three cases, focusing on kinetic and potential energies, the impact of particle size and material density, and the formation of cracks. An insight into creation of cracks under the simulated laboratory conditions was obtained. Additionally, the procedure was able to monitor a nucleation and temporal evolution of cracks which finally lead to breaking apart of using Brazilian test and uniaxial compression samples. Simulations of the uniaxial stretching provided information about three classes of elastic material cracking,

depending on the inter-particles bond parameters. The second part presents the results of simulations of glacier calving. The relationship between the volume of ice falling into the water and the height from which the ice falls and the acceleration of water and ice particles was studied. The general patterns concerning movements of the particles for all heights and sizes of the block of ice were found.

Consequently, the most important achievements within this work are as follows.

DEM model of uniaxial compression:

❑ The simulations of uniaxial compression provided results in three groups of issues: dependencies between microscopic (Young's modulus, Poisson's ratio, cohesion, tangent of the friction angle) and macroscopic (Young's modulus, Poisson's ratio) parameters of samples with densities 940 and 2260 kg/m^3, average potential energy of bonds, average kinetic energy of particles.

❑ One of the clearest relationships between microscopic and macroscopic parameters is that between the microscopic Young's modulus and the macroscopic Young's modulus. A higher value of the first parameter corresponds to a higher value of the second parameter.

❑ Other conclusions came from the observation of a parameter such as cohesion. When keeping the remaining three microscopic parameters fixed, the change in cohesion does not affect macroscopic parameters, Young's modulus and Poisson's ratio, or slightly affects them. For some results the higher microscopic cohesion corresponds to the lower macroscopic Young's modulus.

❑ The lower microscopic Poisson's ratio translates into a higher macroscopic Young's modulus. Additionally, microscopic Poisson's ratio and tangent of the friction affect significantly macroscopic Poisson's ratio, while macroscopic Young's modulus is much weaker.

❑ Interesting results were obtained while considering potential energies of bonds. The average percentage contribution of different potential energies of bonds to the average overall potential energy of bonds during the breaking process is constant. Normal energy is around 61%, shearing energy being around 38%. The smallest share belongs to bending energy and twisting energy, both of these energies being generally less than 1%.

❑ The relationship between kinetic energies of particles is not as obvious at first glance as in the case of energy of potential bonds. Linear kinetic energy prevails, ranging from about 80% to 96%. It is possible to distinguish between two groups of results for which the ratio between linear kinetic energy and rotational kinetic energy is about 80% to 20% or about 94% to 6%. A comparison with microscopic parameters of bonds leads to the conclusion that the microscopic parameter – cohesion – is responsible for the higher proportion of rotational kinetic energy during the breaking process.

DEM model of Brazilian test:

❑ A detailed monitoring of internal microscopic state of loaded samples including changes in kinetic and potential energies of particles.

❑ An insight into the creation of tensile cracks under the simulated laboratory conditions.

❑ Monitoring of the nucleation and temporal evolution of a tensile crack which finally led to the breaking apart of Brazilian test samples.

- Following the evolution of the total kinetic and potential energies during loading, it was possible to identify a few stages in a response of the samples to constant speed loading. At the beginning of loading, the elastic response of the samples was clearly visible. For the intermediate loading, the samples exhibited a viscoelastic property due to the induced particle dislocations. At the end of this stage, large dislocation occurring in block resulted in a visible plastic behaviour of the samples and finally led to crack nucleation and breaking the samples apart.

- Observation how the size of used particles influenced each of the above stages. Although a relatively small range of particle sizes was used, the obtained results clearly showed that the most sensitive to the material composition is the intermediate loading stage when dislocations start to change the properties of materials and lead to crack nucleation. On the other hand, the rather weak dependence of the critical strain and the strain when the crack fully breaks the sample into two pieces shows that this failure stage is rather insensitive to the material composition.

- Scaling of the critical load which the sample can withstand with the inverse of the size of the smallest particles building the sample.

DEM model of uniaxial stretching:

- A series of measurements with three uniaxial stretching velocities. For each one of them, the value of maximum stress was calculated when the main crack occurred. An interesting point is that the maximum stress weakly depends on elastic stiffness for smaller values of this parameter. In this range, the character of cracking seems to be similar. However, for higher values of elastic stiffness there is a significant increase in the maximum value of stress. At the same time, for the same values of elastic stiffness, different uniaxial stretching velocities weakly influence the maximum stress.

- Three different types of cracking; Type I, when multicracking occurs and the cracking is dispersed in time. For this class of processes it is impossible to extract the main breaking event at its specific time; Type II, when dominating "macro-cracks" accompanied with smaller micro-cracks are developing; Type III, when a single crack is created.

- Analysis the kinetic energy and potential energy of the bonds. It is interesting to note that when the peak of the kinetic energy occurs, the strain does not seem to depend on the stretching velocity and elastic stiffness of bonds. Potential energy describes all kinds of interactions related to bonds between particles. For kinetic energy this is total value in every time step. Two interesting issues can be observed. First, as in the case of kinetic energy, the strain for which peak of energy occurs does not seem to depend on stretching velocity and elastic stiffness of bonds. Additionally, the maximum value of potential energy strongly depends on elastic stiffness, but it does not depend very much on velocity.

- Almost a linear relationship between the maximum kinetic energy during the entire simulation and stretching velocity, for different values of elastic stiffness of bonds. Meanwhile, the maximum potential energy is almost constant as a function of stretching velocity.

- The relationship between kinetic energy of particle linear movement, potential energy of bonds between particles and number of bonds between particles as a function of stretching velocity and elastic stiffness of the bonds.

DEM model of glacier calving:

- ❑ Acceleration recordeded by receivers in the water (on the surface) quickly decreases with distance, while for receivers in the depth, there is no straightforward dependence. Moreover, larger volume of ice falling down to the water causes smaller acceleration of water particles or this acceleration does not depend on the volume (however, this is true only for the surface receivers, receivers in depth are not sensitive on volume parameter).

- ❑ General patterns related to movements of the particles for all heights and sizes of the block of ice were outlined. Considering surface receivers, the one located closest to the place of ice fall accelerates exactly at the moment of impact and then accelerations always disappear. Receiver in the centre of the tank accelerates in the middle period of the simulation. This seems to be a result of wave superposition, which moves back and forth inside the tank. The farthest receiver accelerates only at the end of the simulation. For receivers in depth, receiver just below the place of fall accelerates just after the impact moment. In contrast, other receivers, which are also close to the bottom, show mostly accelerations related to movements of the particles due to the gravitational force.

- ❑ Patterns for the receivers in the glacier are more difficult to describe. However, it was observed that oscillations in acceleration start with a delay related to the distance between the receiver and the place of cracking.

The scientific goal adopted at the beginning of the research was to obtain the microscopic insight into fracturing of brittle materials using the Discrete Element Method. In the light of the abovementioned conclusions, it can be claimed that the preliminary assumptions were achieved.

APPENDIX A

Okeanos Supercomputer

DEM simulations require a significant number of particles and a huge amount of computational resources. The best solution (in the case of complex models consisting of a huge number of particles) is to run DEM calculations on powerful machines such as supercomputers. A supercomputer is a type of computer that has the architecture, resources and components needed to achieve massive computing power. Today's supercomputers are built of tens of thousands of processors that are able to perform billions and trillions of floating point operations per second. Supercomputers incorporate architectural and operational principles from parallel and grid processing, where a process is simultaneously executed on thousands of processors or is distributed among them.

In the presented work, the supercomputer Cray XC40 "Okeanos" (Fig. A.1), which belongs to Interdisciplinary Centre for Mathematical and Computational Modelling of Warsaw University was used with great advantage (Computational Research Grants on The Okeanos Supercomputer ICM UW, Project GC70-6, Project GB72-7). The work started in July 2016 and comprised 1084 computing nodes. Each node had 24 Intel Xeon CPU cores (x86_64 architecture, code name Haswell) with a 2-way Hyper Threading (HT). The nodes are connected with a Cray Aries Network, with a Dragonfly topology. Each node has 128 Gb of main memory (RAM). The memory is organized in ccNUMA (cache coherent Non-Uniform Memory Access) domains. Computing nodes do not have a local storage. All data is stored on the parallel file

Fig. A.1. The supercomputer Cray XC40 "Okeanos" (from kdm.icm.edu.pl/kdm/Witamy).

system. Detailed description of the ICM machines can be found on the webpage [kdm.icm.edu.pl/kdm/ Witamy].

Access to the Okeanos system is available with secure shell interface. User sessions are started on a login node, visible as OkeanosX (where X = 1,2,3), by using a round-robin order. Login-nodes are only for job preparation, data transmission and program compilation. It is not allowed to run any computation or load intensive applications on the login-nodes. User jobs are submitted to the batch system and executed on computing nodes. The system is controlled by the Slurm resource manager (batch system). To prepare a computing job, user should create dedicated script with resource specification and commands to execute the application. The system runs on the Linux operating system. The system is characterized by very high computational power as well as outstanding graph analytics capability and extreme performance on data-intensive workloads. Okeanos is best suited for large-scale computations, which require several thousand cores and several tens of terabytes of memory in a single run. Supporting such large-scale computations is the primary purpose of the Okeanos supercomputer.

The efficiency of the supercomputer was verified during "scaling test", performed on the basis of uniaxial compression. For the purpose of this test, a cylindrical sample consisting of about 100 000 particles was used. Particle sizes were in range of 0.3–3.0 mm. The cylinder was 20 cm in height, with a diameter of 10 cm (Fig. A.2).

The calculation times were determined for different core distributions. In ESyS-Particle, the simulation domain is divided between cores spatially according to vector $[x,y,z]$. Numbers x, y, and z describe how many cores work in which direction. Total number is equal to $x*y*z$ plus one Master core. The results are shown in Table A.1.
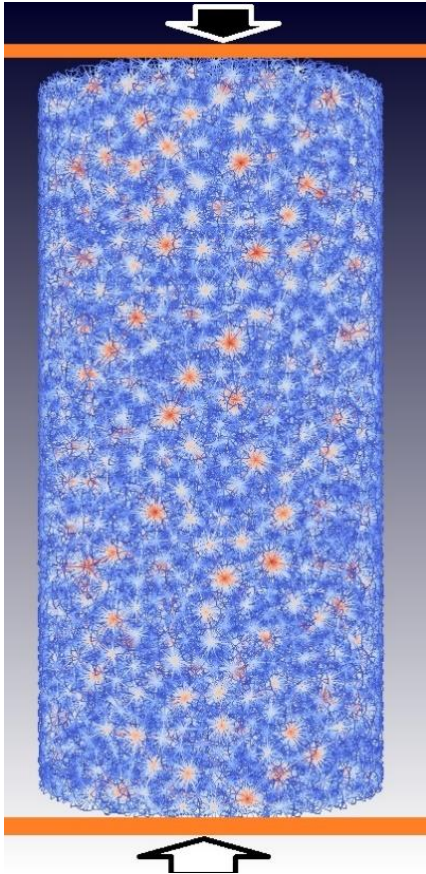
Fig. A.2. The sample used for determining calculation times on the supercomputer. View of bonds for approximately 100 000 particles.

Table A.1

Calculation times for different core distribution

Cores distribution	Number of processors	Time	
		minutes	seconds
[1,1,1] = 1 PC	1	412	52
[1,1,1] = 1	1	416	28
[2,2,2] = 8	8	156	19
[2,3,2] = 12	12	193	48
[2,5,2] = 20	20	137	7
[2,9,2] = 36	36	153	37
[2,10,2] = 40	40	140	2
[2,10,2] = 40	40	139	34
[2,10,2] = 40	40	139	28
[2,11,2] = 44	44	142	42
[2,20,2] = 80	80	110	48
[2,20,2] = 80	80	110	44
[3,10,3] = 90	90	203	56
[5,5,5] = 125	125	195	39
[5,8,5] = 200	200	152	37
About 100 000 particles in range 0.3–3.0 mm			

First, the simulation was ran using only one core of the supercomputer, and then one core of the personal computer. One core of the supercomputer executed simulation with more than 416 minutes. Surprisingly, one core of the personal computer was 4 minutes faster and dealt with the task within about 412 minutes. Certainly, the real power of the supercomputer is visible for higher number of cores. For this type of simulation, the most efficient number of cores was 80 with distribution [2,20,2]. With this setup our simulation was almost 4 times faster than that run on the one core.

As shown in Fig. A.3, the bigger the number of cores, the faster the simulation. However, this is true only up to some point. When too many cores are used with respect to the size of the sample, the calculation time increases.

Fig. A.3.The relationship between core number and calculation time.
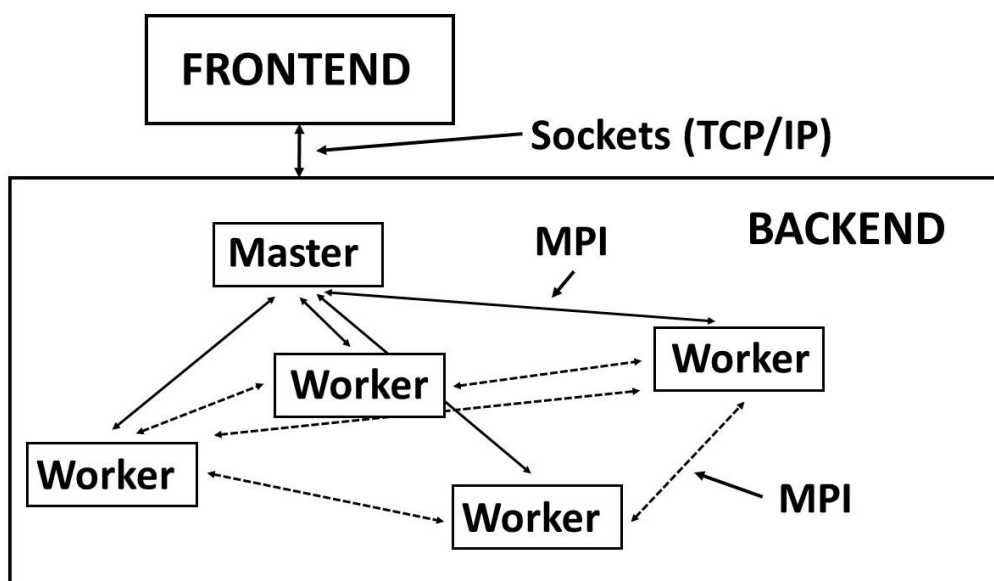
Fig. A.4. Process structure of the parallel ESyS-Particle. The communication between the parallel processes is provided by MPI interface (from Abe et al. 2004).
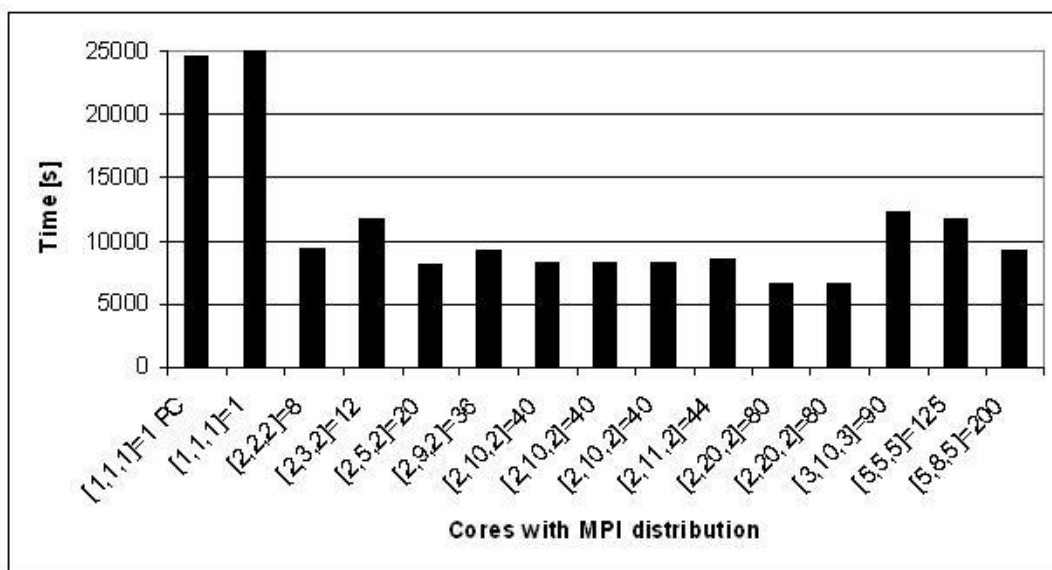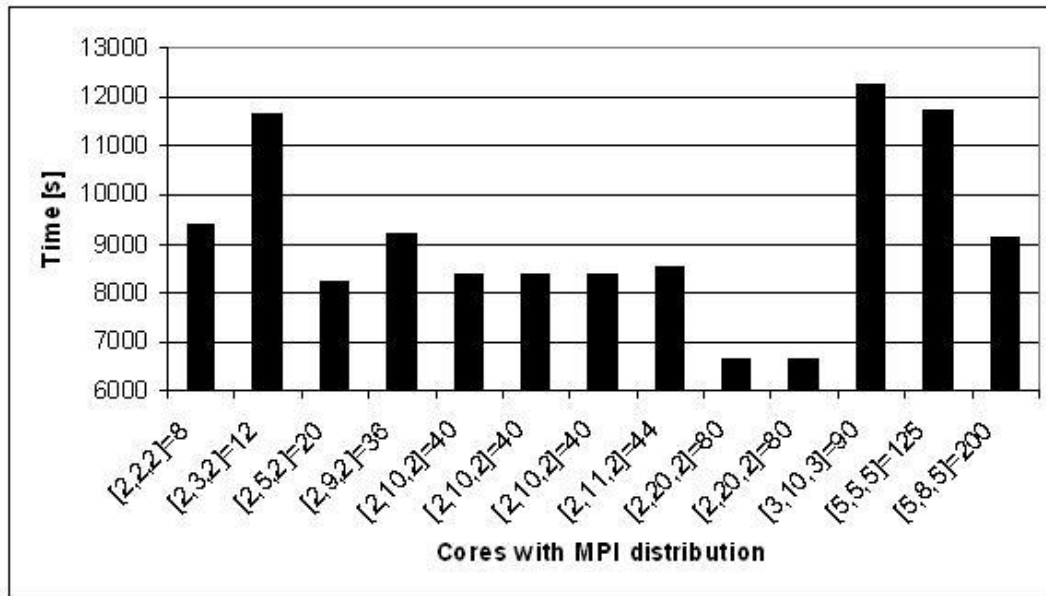
Fig. A.5. Enlarged part of the chart shown in Fig. A.3, only for bigger number of cores.

The reason underlying such phenomena is the MPI structure (Fig. A.4). Workers communicate with each other and are managed by the master. However, when the amount of work is too small for assigned workers, then the time for communication becomes a dominating factor. Consequently, the efficiency of calculation decreases.

For reasons mentioned earlier, one has to take care about proper core distribution. As shown in Fig. A.5, the calculation time may increase significantly after exceeding the critical threshold.

APPENDIX B

Anatomy of the ESyS-Particle and GenGeo scripts, on the example of glacier calving simulation

This appendix presents the complete set of programs for simulating glacier calving. It consists of the following scripts:

- ❑ Slurm Script: this script is prepared to run the simulation on the supercomputer and defines important parameters such as allocation of computing resources, maximum calculation time or name of the main program.
- ❑ GenGeo Script: GeoGeo is additional library associated with ESyS-Particle and is used for generating particle geometries. After generation, such geometry is implemented later in the main ESyS-Particle script.
- ❑ ESyS-Particle Script: this is the main part, which describes all technical and physical aspects of the simulation.
- ❑ Mesh Files: some simulations require more sophisticated geometries, where standard walls implemented in ESyS-Particle are insufficient. In such case, it is necessary to create additional walls in separated files (mesh files).

I would like to gratefully acknowledge all ESyS-Particle team for their great tutorial (Abe et al. 2014). This appendix is based on it and presents only small part of the software possibilities. Deeper description can be found in the abovementioned tutorial or on the webpages: [https://launchpad.net/esys-particle] and [https://launchpad.net/esys-particle/gengeo].

Slurm script for supercomputer

```
#!/bin/bash -l
#SBATCH --job-name=calving1
#SBATCH --output="output.out"
#SBATCH --error="error.err"
#SBATCH --account="GB72-7"
#SBATCH --nodes=1
#SBATCH --tasks-per-node=48
#SBATCH --time=48:00:000


module swap PrgEnv-cray PrgEnv-intel
module load esys-particle

time srun -n 2 esysparticle iceberg_mesh.py
```

This script defines important parameters such as allocation of computing resources, maximum calculation time, name of the main program, additional libraries, and, finally, the name of the main program.

Simulation geometry generated with GenGeo

```
# --- geometry setup script for block with smooth sides ---
from gengeo import *


# particle size range
minRadius = 200
maxRadius = 800


# - input parameters --
# block dimensions
x0=-50000
y0=-50000
z0=-50000

xdim0=50000
ydim0=50000
zdim0=50000
```

```
# corner points
minPoint0 = Vector3(x0,y0,z0)
maxPoint0 = Vector3(xdim0,ydim0,zdim0)



# neighbour table
mntable = MNTable3D(
minPoint=minPoint0,
maxPoint=maxPoint0,
gridSize=2.5*maxRadius,
numGroups=3 #the initial number of groups (default: 1)
)

#lod
x1=-15000
y1=10000
z1=0

xdim1=30000
ydim1=20000
zdim1=2000



#woda
x3=-40000
y3=-20000
z3=0

xdim3=-5000
ydim3=0
zdim3=2000

# corner points
minPoint1 = Vector3(x1,y1,z1)
maxPoint1 = Vector3(xdim1,ydim1,zdim1)



minPoint3 = Vector3(x3,y3,z3)
maxPoint3 = Vector3(xdim3,ydim3,zdim3)



# block volume1
box1 = BoxWithPlanes3D(minPoint1,maxPoint1)

# boundary planes
bottomPlane1=Plane(minPoint1,Vector3(0.0,1.0,0.0))
leftPlane1=Plane(minPoint1,Vector3(1.0,0.0,0.0))
frontPlane1=Plane(minPoint1,Vector3(0.0,0.0,1.0))
topPlane1=Plane(maxPoint1,Vector3(0.0,-1.0,0.0))
rightPlane1=Plane(maxPoint1,Vector3(-1.0,0.0,0.0))
backPlane1=Plane(maxPoint1,Vector3(0.0,0.0,-1.0))
```

```
# add them to the box
box1.addPlane(bottomPlane1)
box1.addPlane(leftPlane1)
box1.addPlane(frontPlane1)
box1.addPlane(topPlane1)
box1.addPlane(rightPlane1)
box1.addPlane(backPlane1)


# block volume3
box3 = BoxWithPlanes3D(minPoint3,maxPoint3)

# boundary planes
bottomPlane3=Plane(minPoint3,Vector3(0.0,1.0,0.0))
leftPlane3=Plane(minPoint3,Vector3(1.0,0.0,0.0))
frontPlane3=Plane(minPoint3,Vector3(0.0,0.0,1.0))
topPlane3=Plane(maxPoint3,Vector3(0.0,-1.0,0.0))
rightPlane3=Plane(maxPoint3,Vector3(-1.0,0.0,0.0))
backPlane3=Plane(maxPoint3,Vector3(0.0,0.0,-1.0))

# add them to the box
box3.addPlane(bottomPlane3)
box3.addPlane(leftPlane3)
box3.addPlane(frontPlane3)
box3.addPlane(topPlane3)
box3.addPlane(rightPlane3)
box3.addPlane(backPlane3)


# -- setup packer --
# iteration parameters
insertFails = 1000
maxIter = 1000
tol = 1.0e-6

# packer
packer = InsertGenerator3D(200,800,insertFails,maxIter,tol,False)
packer3 = InsertGenerator3D(67,267,insertFails,maxIter,tol,False)

# pack particles into volume
packer.generatePacking(
volume=box1, #the volume to fill with particles
ntable=mntable, #the neighbours table that particles are inserted into
groupID=0,#the group ID assigned to particles (default: 0)
tag=100#the tag assigned to the generated particles (optional (default: -
1) if not followed by ShapeList)
)

# pack particles into volume
packer3.generatePacking(
```

```
volume=box3, #the volume to fill with particles
ntable=mntable, #the neighbours table that particles are inserted into
groupID=2,#the group ID assigned to particles (default: 0)
tag=200#the tag assigned to the generated particles (optional (default: -
1) if not followed by ShapeList)
)


# create bonds between neighbouring particles:
mntable.generateBonds(
groupID=0,#the group ID of particles to bond together (default: 0)
tolerance=1.0e-5,#maximum distance separating bonded particles
bondID=0)#the bond ID to assign generated bonds


# write a geometry file
mntable.write("berg_meshBezKlastrow2.geo", 1)
mntable.write("berg_meshBezKlastrow2.vtu", 2)
```

Explanation of GenGeo script

The GenGeo is an additional library created for generating advanced particle geometries (Fig. B.1), which can be used in ESyS-Particle simulations.

The GenGeo library is built around three basic concepts: geometrical volumes to fill with particles, a "Packer" to place the particles into the volumes according to given criteria, and the "Neighbour Table" – a container to store the particles and to keep track of their relative positions and neighbour relations.

```
# --- geometry setup script for block with smooth sides ---
from gengeo import *
```

The implemented packers are based on the insertion-based algorithm. The advantages of this packing strategy are that it produces relatively dense particle arrangements where each interior particle is touched by at least 4 other particles in 3D (by 3 other particles in 2D) and that there are nofrozen-in stresses between the particles. The disadvantage is that the user cannot control the particle size distribution except for the minimum and maximum particle radius allowed.

Most GenGeo scripts consist of 5 steps:
1. setting up a neighbour table
2. defining the volume to be filled
3. setting up the packer
4. running the packer to fill the box and, if required, bond the particles together
5. write the particle data to an output file

First, a couple of parameters is defined that will be needed repeatedly throughout the script, namely the dimensions of the box, which is intended to fill and the minimum and maximum radius of the particles. This sets the shape of the box to a square prism.
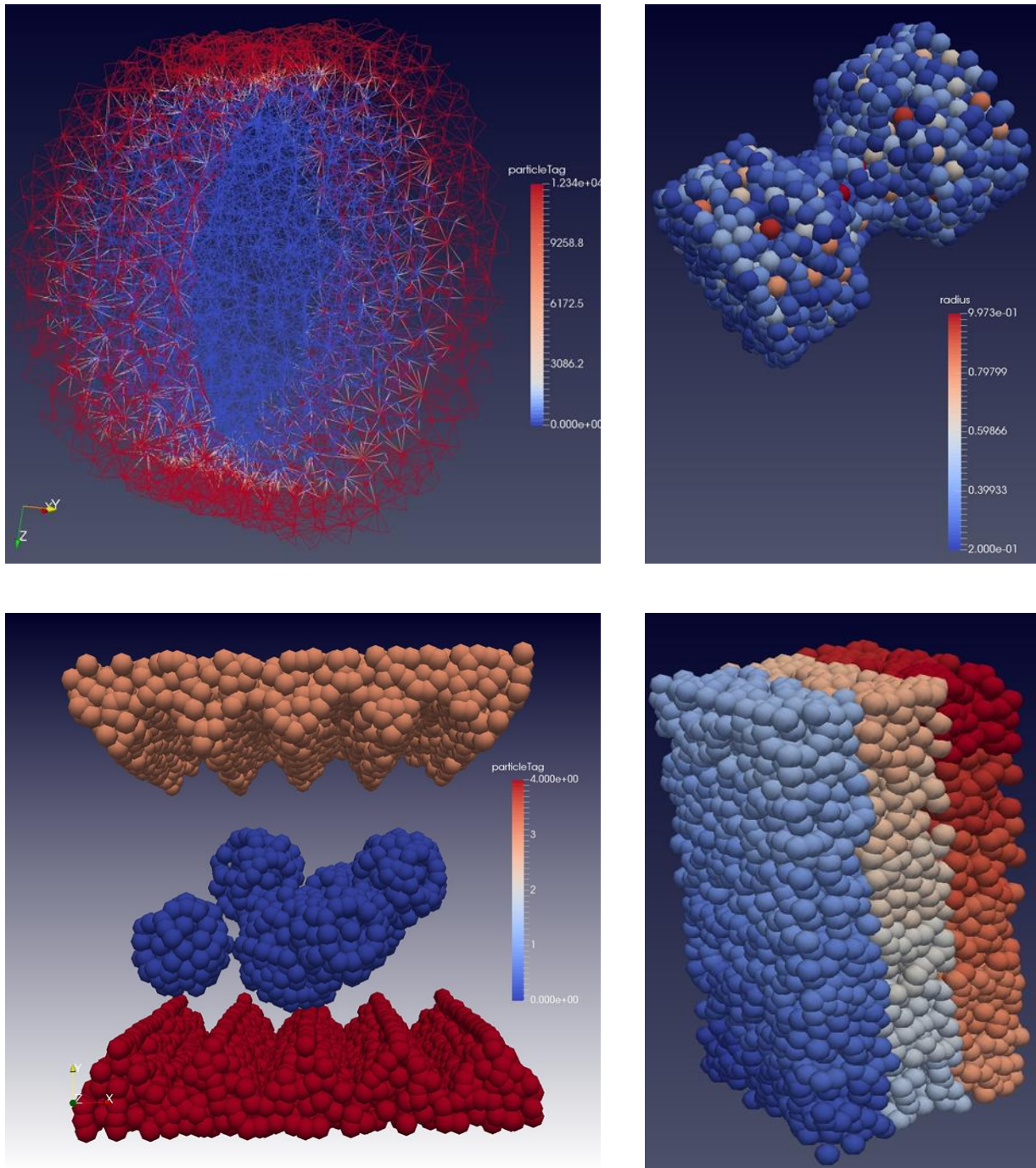
Fig. B.1. Examples of geometries generated with GenGeo.

```
x1=-15000
y1=10000
z1=0

xdim1=30000
ydim1=20000
zdim1=2000
```

The corner points can be used to define both the volume to be filled and the neighbour table to contain the particles. The volume, which is of the class BoxWithPlanes3D, takes exactly two parameters in its constructor, describing the locations of two opposite corners of the box. Therefore, both parameters are of type Vector3.

```
# corner points
minPoint1 = Vector3(x1,y1,z1)
maxPoint1 = Vector3(xdim1,ydim1,zdim1)

# block volume1
box1 = BoxWithPlanes3D(minPoint1,maxPoint1)

# boundary planes
bottomPlane1=Plane(minPoint1,Vector3(0.0,1.0,0.0))
leftPlane1=Plane(minPoint1,Vector3(1.0,0.0,0.0))
frontPlane1=Plane(minPoint1,Vector3(0.0,0.0,1.0))
topPlane1=Plane(maxPoint1,Vector3(0.0,-1.0,0.0))
rightPlane1=Plane(maxPoint1,Vector3(-1.0,0.0,0.0))
backPlane1=Plane(maxPoint1,Vector3(0.0,0.0,-1.0))

# add them to the box
box1.addPlane(bottomPlane1)
box1.addPlane(leftPlane1)
box1.addPlane(frontPlane1)
box1.addPlane(topPlane1)
box1.addPlane(rightPlane1)
box1.addPlane(backPlane1)
```

Next, it is necessary to create a neighbour table to store the particles. The constructor for the neighbour table takes four arguments: two corner points (minPoint, maxPoint) to describe the volume covered by the model, the grid spacing (gridSize) and the number of particle groups (numGroups). The volume covered by the neighbor table should ideally be the bounding box of the whole model, i.e., it needs to cover all particles, but it should not be much larger in order to minimize the memory used. The grid spacing determines the search range used for the determining if two particles touch each other. To ensure all touching (or intersecting) pairs of particles can be found the grid spacing needs to be larger than twice the maximum particle radius. The number of particle groups will only be different from 1 for rather complicated geometry setup scripts.

```
# neighbour table
mntable = MNTable3D(
minPoint=minPoint0,
maxPoint=maxPoint0,
gridSize=2.5*maxRadius,
numGroups=3 #the initial number of groups (default: 1)
)
```

Next, the "packer" is set up that places the particles inside the volume. The most simple constructor for this type of packer takes 5 arguments. In addition to the minimum and maximum particle radius (minRadius, maxRadius) there are 3 parameters that control the performance of

the packing algorithm. These are the number of consecutive failed particle insertion attempts allowed before the algorithm gives up and terminates (insertFails), the maximum number of iterations for the internal sphere fitting procedure (maxIterations) and the precision of the sphere fitting, i.e., the maximum tolerance up to which two particles are still considered touching (tolerance). The values insertFails=1000, maxIterations=1000 and tolerance=1e-6 usually work fine for small to medium models. For large models it is necessary to increase the value of insertFails to obtain a good packing of the particles. The value of tolerance should be considered in relation to the particle radii. A sixth parameter seed can be used to force a re-seeding of the random number generator before the packing algorithm starts. Setting seed=True guarantees a different packing with each run of the script, otherwise, the run is system-dependent.

Generating an assembly of particles includes the following three steps:
1. generating a block of unbonded particles,
2. creating bonds between neighbouring particles, and
3. specifying the type of interactions between bonded-particle-pairs.

For generating a block of unbonded particles ESyS-Particle provides four methods for generating a block of particles: SimpleBlock – generates a block of particles whose centres-of-mass reside on the vertices of a regular cubic lattice. This is the simplest configuration but is typically not the best choice for serious simulations because the particle-packing is not ideal (the porosity is very high); CubicBlock – generates a Face-Centred Cubic (FCC) lattice of particles with a dense packing arrangement; HexagBlock – generates a Hexagonal Close Packing (HCP) of particles; RandomBoxPacker – generates a block of particles with radii randomly distributed in a specified range. The use of uniform particle sizes and regular particle arrangements introduces artefacts such as preferential movement along lattice planes. A simple way to remove such artefacts and to model more realistic granular materials is to use particle assemblies in which the positions and radii of particles are selected randomly.

The RandomBoxPacker and some other ESyS-Particle Packer modules make use of an iterative, geometrical space-filling algorithm to insert particles within a prescribed volume. The algorithm may be summarized as follows:
1. Insert a number of seed particles at random locations within the volume ensuring they do not overlap.
2. Identify 4 adjacent particles
(a) compute the centroid of the tetrahedron defined by the 4 particles
(b) compute the radius of a particle that touches all 4 particles
(c) if the radius of that particle is within the specified range and it is entirely within the prescribed volume, insert the particle
3. Repeat step 2 until the number of failed insertion attempts reaches the maxInsertFails

The tolerance parameter defines what is implied by touching in the above algorithm. If particles overlap by less than the prescribed tolerance, they are said to be touching. The cubicPackRadius is a parameter for setting up the neighbours table used to track relative locations of adjacent particles. The optimal value for this is approximately 2.2 x maxRadius. circDimList informs the packing algorithm of any circular (or periodic) boundaries so particles will be fitted together along these boundaries rather than being fitted to straight walls. This algorithm for filling a volume with spherical particles has some distinct advantages over some other methods but also has some limitations. The algorithm requires no equilibration simulation such as some dynamical methods (e.g. expanding particle algorithms) to achieve a close packing of relatively

low porosity. On the downside, the user has little control over the final distribution of particle sizes (apart from specifying the range of sizes). Experience has shown that for a broad range of sizes (e.g. [0:1; 1:0]) the final particle size distribution is a power-law. For a narrow range of sizes (e.g. [0:4; 0:6]) the size distribution is approximately a uniform random distribution.

```
# -- setup packer --
# iteration parameters
insertFails = 1000
maxIter = 1000
tol = 1.0e-6


# packer
packer    =    InsertGenerator3D(    minRadius,maxRadius,insertFails,max-
Iter,tol,False)
packer3    =    InsertGenerator3D(    minRadius,maxRadius,insertFails,max-
Iter,tol,False)
```

When the volume, the neighbour table and the packer are defined, the actual work can start. First the packer needs to fill the volume with particles. In the simplest case this requires two arguments to the generatePacking function of the packer: the volume to fill and the neighbour table in which to store the particles.

```
# pack particles into volume
packer.generatePacking(
volume=box1, #the volume to fill with particles
ntable=mntable, #the neighbours table that particles are inserted into
groupID=0,#the group ID assigned to particles (default: 0)
tag=100#the tag assigned to the generated particles (optional (default: -
1) if not followed by ShapeList)
)
```

The last thing to do to complete the generation of the particle arrangement is to create the bonds between touching particle-pairs. Because the neighbour table contains all information necessary to determine which particles should be bonded, i.e., particle positions and radii, the bonding procedure is a member function of the neighbour table. The most simple form of the function call, which just bonds all neighbouring particles in one group, needs 3 arguments: the ID of the particle group that should be bonded groupID, the bonding tolerance and the tag given to the newly created bonds bondID. Because considered neighbour table contains only one group of particles, the groupID can be equal to 0. The tolerance for bonding should normally be larger than the packing tolerance used in the packer, hence, 1.0e-05 is chosen here. The bond tag can be set to any value, in this case it was marked as 0.

```
# create bonds between neighbouring particles:
mntable.generateBonds(
groupID=0,#the group ID of particles to bond together (default: 0)
tolerance=1.0e-5,#maximum distance separating bonded particles
bondID=0)#the bond ID to assign generated bonds
```

ESyS-Particle script written in Python

```python
from esys.lsm import *
from esys.lsm.util import *
from esys.lsm.geometry import *
from WallLoader import WallLoaderRunnable
from WallLoaderMod import WallLoaderRunnableMod
from math import *

#mpirun -np 2 esysparticle tiger.py
#dump2vtk -i snapshot -o vtk_snaps_ -rot -t 0 2 1

maxR=800
minR=200
time_steps=2000000
increment=1000

field_saver=500
check_pointer=10000


ym=1.0e+06
pr=0.25
coh=1000.0
ta=1.0
den=940*1.0e-06
den2=1000*1.0e-06

dt=1.0e-04

plik=open("step.dat","w")
plik.write(str(dt))
plik.close()

#instantiate a simulation object:
sim = LsmMpi (numWorkerProcesses = 1, mpiDimList = [1,1,1])

#initialise the neighbour search algorithm:
sim.initNeighbourSearch (
particleType = "RotSphere",
gridSpacing = 2*maxR+0.2*minR,
verletDist = 0.2*minR
)
```

```
#set the number of timesteps and timestep increment:
sim.setNumTimeSteps (time_steps)
sim.setTimeStepSize (dt)

sim.readGeometry("berg_meshBezKlastrow2.geo")

#density
sim.setParticleDensity(
tag=100,
mask=-1,
Density=den
)

#density
sim.setParticleDensity(
tag=200,
mask=-1,
Density=den2
)

sim.createWall (
name = "right_wall",
posn = Vec3(30000.0, 0.0, 0.0),
normal = Vec3(-1.0, 0.0, 0.0)
)

sim.createWall (
name = "left_wall",
posn = Vec3(-40000.0, 0.0, 0.0),
normal = Vec3(1.0, 0.0, 0.0)
)

sim.createWall (
name = "back_wall",
posn = Vec3(0.0, 0.0, 0.0),
normal = Vec3(0.0, 0.0, 1.0)
)

sim.createWall (
name = "front_wall",
posn = Vec3(0.0, 0.0, 2000.0),
normal = Vec3(0.0, 0.0, -1.0)
)
```

```
sim.readMesh(
fileName = "meshBottom.msh",
meshName = "meshBottom_wall"
)

sim.readMesh(
fileName = "meshBottomBottom.msh",
meshName = "meshBottomBottom_wall"
)

sim.readMesh(
fileName = "meshRight.msh",
meshName = "meshRight_wall"
)


#create rotational elastic-brittle bonds between particles:
pp_bonds = sim.createInteractionGroup (
BrittleBeamPrms(
name="pp_bonds",
youngsModulus=ym,
poissonsRatio=pr,
cohesion=coh,
tanAngle=ta,
tag=0 #Connections which are tagged with tag will be created
with these parameters. bondTag
)
)

#initialise frictional interactions for unbonded particles:
sim.createInteractionGroup (
FrictionPrms(
name="friction",
youngsModulus=ym,
poissonsRatio=pr,
dynamicMu=0.4,
staticMu=0.6
)
)
#create an exclusion between bonded and frictional interac-
tions:
```

```
sim.createExclusion (
interactionName1 = "pp_bonds",
interactionName2 = "friction"
)


#initialise gravity in the domain:
sim.createInteractionGroup(
GravityPrms(name="earth-gravity", acceleration=Vec3(0,-
9.81,0))
)


#specify elastic repulsion from the top wall:
sim.createInteractionGroup (
NRotElasticWallPrms (
name = "right_wall_repel",
wallName = "right_wall",
normalK = ym
)
)

#specify elastic repulsion from the top wall:
sim.createInteractionGroup (
NRotElasticWallPrms (
name = "left_wall_repel",
wallName = "left_wall",
normalK = ym
)
)


#specify elastic repulsion from the top wall:
sim.createInteractionGroup (
NRotElasticWallPrms (
name = "back_wall_repel",
wallName = "back_wall",
normalK = ym
)
)

#specify elastic repulsion from the top wall:
sim.createInteractionGroup (
NRotElasticWallPrms (
name = "front_wall_repel",
```

```
wallName = "front_wall",
normalK = ym
)
)



sim.createInteractionGroup (
NRotElasticTriMeshPrms (
name = "meshBottom_repell",
meshName = "meshBottom_wall",
normalK = ym
))

sim.createInteractionGroup (
NRotElasticTriMeshPrms (
name = "meshBottomBottom_repell",
meshName = "meshBottomBottom_wall",
normalK = ym
))

sim.createInteractionGroup (
NRotElasticTriMeshPrms (
name = "meshRight_repell",
meshName = "meshRight_wall",
normalK = ym
))



#add translational viscous damping:
sim.createInteractionGroup (
LinDampingPrms(
name="damping1",
viscosity=0.002,
maxIterations=50
)
)
#add rotational viscous damping:
sim.createInteractionGroup (
RotDampingPrms(
name="damping2",
viscosity=0.002,
```

```
maxIterations=50
)
)


#total kinetic energy
sim.createFieldSaver (
ParticleScalarFieldSaverPrms(
fieldName="e_kin",
fileName="ekin.dat",
fileFormat="SUM",
beginTimeStep=0,
endTimeStep=time_steps,
timeStepIncr=field_saver
)
)

#linear kinetic energy
sim.createFieldSaver (
ParticleScalarFieldSaverPrms(
fieldName="e_kin_linear",
fileName="ekin_linear.dat",
fileFormat="SUM",
beginTimeStep=0,
endTimeStep=time_steps,
timeStepIncr=field_saver
)
)

#rotational kinetic energy
sim.createFieldSaver (
ParticleScalarFieldSaverPrms(
fieldName="e_kin_rot",
fileName="ekin_rot.dat",
fileFormat="SUM",
beginTimeStep=0,
endTimeStep=time_steps,
timeStepIncr=field_saver
)
)

#add a FieldSaver to store total potential energy:
sim.createFieldSaver (
InteractionScalarFieldSaverPrms(
```

```
interactionName="pp_bonds",
fieldName="potential_energy",
fileName="epot.dat",
fileFormat="SUM",
beginTimeStep=0,
endTimeStep=time_steps,
timeStepIncr=field_saver
)
)



#create a FieldSaver to store number of bonds:
sim.createFieldSaver (
InteractionScalarFieldSaverPrms(
interactionName="pp_bonds",
fieldName="count",
fileName="nbonds.dat",
fileFormat="SUM",
beginTimeStep=0,
endTimeStep=time_steps,
timeStepIncr=field_saver
)
)



#add a CheckPointer to store simulation data:
sim.createCheckPointer (
CheckPointPrms (
fileNamePrefix = "snapshot",
beginTimeStep = 0,
endTimeStep = time_steps,
timeStepIncr = check_pointer
)
)

nr=sim.getNumParticles()
print(nr)

#execute the simulation:
sim.run()
```

Mesh file generating bottom wall for glacier

```
Triangle
3D-Nodes 4
0 0 0 -5000.0 10000.0 0.0
1 1 0 30000.0 10000.0 0.0
2 2 0 30000.0 10000.0 2000.0
3 3 0 -5000.0 10000.0 2000.0


Tri3 2
0 0 0 0 1 2
1 0 0 2 3
```

Mesh file generating bottom wall for water

```
Triangle
3D-Nodes 4
0 0 0 -5000.0 -20000.0 0.0
1 1 0 -5000.0 -20000.0 2000.0
2 2 0 -40000.0 -20000.0 2000.0
3 3 0 -40000.0 -20000.0 0.0


Tri3 2
0 0 0 0 1 2
1 0 0 2 3
```

Mesh file generating left wall for water

```
Triangle
3D-Nodes 4
0 0 0 -40000.0 10000.0 0.0
1 1 0 -40000.0 10000.0 2000.0
2 2 0 -40000.0 -20000.0 2000.0
3 3 0 -40000.0 -20000.0 0.0


Tri3 2
0 0 0 2 1
1 0 0 3 2
```

Mesh file generating right wall for water

```
Triangle
3D-Nodes 4
0 0 0 -5000.0 10000.0 0.0
1 1 0 -5000.0 10000.0 2000.0
2 2 0 -5000.0 -20000.0 2000.0
3 3 0 -5000.0 -20000.0 0.0


Tri3 2
0 0 0 1 2
1 0 0 2 3
```

Explanation of ESyS-Particle script

The main components of any ESyS-Particle simulation are: initialization of an ESyS-Particle simulation object, specification of the spatial domain, particle creation and initialization, definition of inter-particle interactions, and execution of time integration. To use the ESyS-Particle simulation libraries in Python, it is necessary to import the modules, which will be used. The following statements are required:

```
from esys.lsm import *
from esys.lsm.util import *
from esys.lsm.geometry import *
from WallLoader import WallLoaderRunnable
from WallLoaderMod import WallLoaderRunnableMod
from math import *
```

These statements load a number of relevant classes and subroutines required for all ESyS-Particle simulations. These statements also import the Vec3 and BoundingBox classes. Objects of the Vec3 class are 3-component vectors, which are useful for specifying position, velocity or acceleration vectors in 3D.

Every ESyS-Particle simulation commences with the creation of an ESyS-Particle simulation object called LsmMpi. This object provides a means to define and run a simulation and can be thought of as a container to which simulation components are added, such as a list of particles, walls, different types of interactions and data output components. The following code-fragment creates a simulation object:

```
#instantiate a simulation object:
sim = LsmMpi (numWorkerProcesses = 1, mpiDimList = [1,1,1])
```

The statement creates an LsmMpi object and takes two arguments. The numWorkerProcesses argument specifies the number of MPI processes to use for calculations. However, this argument can be set to a larger value for an MPI-parallel simulation (in the case of access to a computer with multiple processor cores/CPUs). The second argument (mpiDimList) specifies

the manner in which the domain will be divided among the worker processes. The first coordinate refers to the number of subdivisions in the *x*-direction, while the second and third coordinates specify the number of subdivisions in the *y*- and *z*-directions respectively. It is important that numWorkerProcesses should be equal to the total number of subdomains specified by the mpiDimList.

```
#initialise the neighbour search algorithm:
sim.initNeighbourSearch (
particleType = "RotSphere",
gridSpacing = 2*maxR+0.2*minR,
verletDist = 0.2*minR
)
```

The statement (sim.initNeighbourSearch) specifies the type of particles used in the simulation. The two most common particle types are *NRotSphere* and *RotSphere*. sim.initNeighbourSearch also sets two parameters for the contact detection algorithm. The gridSpacing parameter defines the size of cubic cells used to identify contacting particles. This parameter needs to be larger than the maximum particle diameter. The verletDist parameter determines the frequency with which the contact lists are updated. If any particle moves a distance greater than verletDist the lists are updated. Optimal values for these two parameters satisfy the inequality gridSpacing > 2 x maxRadius + verletDist.

Reducing the verletDist will result in more accurate force calculations (because new contacts will be detected earlier) but the lists will be updated more frequently, which is computationally expensive. In most cases, the gridSpacing should be set to approximately 2.5 x the maximum particle radius and the verletDist should be approximately 0.2 x the minimum particle radius. These two statements result in the construction of a suitable ESyS-Particle simulation object called sim. The simulation object now becomes a container to which particles can be added, as well as walls, and various types of interactions. Before it is done, it is necessary to specify how many timesteps to compute during the simulation and the timestep increment (in seconds):

```
#set the number of timesteps and timestep increment:
sim.setNumTimeSteps (time_steps)
sim.setTimeStepSize (dt)
```

These two statements can be described as follows: the total number of timesteps will be computed, with a time increment of *dt* seconds between each timestep. It is usually a good idea to set the timestep increment before creating particles or interactions. In some cases, the timestep increment is needed internally to correctly initialize interactions.

Prior to addition of particles, the simulation object must be assigned a valid spatial domain. Any particles or walls residing outside this domain are eliminated from force calculations and time integration. The following code-fragment specifies the spatial domain for a simulation, which was defined by the GenGeo script.

```
sim.readGeometry("berg_meshBezKlastrow2.geo")
```

Having added particles to the simulation object, it is necessary to specify the type of interactions between the particles if they should come into contact (which they will due to the carefully selected initial positions and velocities above). There are a number of different types of particle-particle interactions that may be used, but in this code rotational elastic-brittle bonds were used.

For particle-pair interactions that incorporate both translational and rotational degrees of freedom, this is achieved in the following manner. Two bonded particles may undergo normal and shear forces, as well as bending and twisting moments. Bonds designed to import such forces and moments are known as cementitious bonds (or, in ESyS-Particle, BrittleBeamPrms interactions). Unlike the non-rotational equivalent, rotational frictional interactions impart a torque to both particles, causing the particles to rotate relative to each other when they are in frictional contact. The detailed description of inter-particle interactions can be found in the Section 3.3.2, together with a schematic picture (Fig. 6).

Because a broken bond represents a fracture surface, it is appropriate to specify frictional interactions between unbonded particles. The following code fragment implements frictional interactions between unbonded, touching particles:

```
#initialise frictional interactions for unbonded particles:
sim.createInteractionGroup (
FrictionPrms(
name="friction",
youngsModulus=ym,
poissonsRatio=pr,
dynamicMu=0.4,
staticMu=0.6
)
)
```

Rotational frictional interactions are defined by a microscopic Young's modulus (youngs Modulus) and Poisson's ratio (poissonsRatio) and two microscopic coefficients of friction. Typically the Young's modulus and Poisson's ratio for FrictionPrms interactions are set equal to their BrittleBeamPrms counterparts. The staticMu coefficient of friction is applied when two particles are in static frictional contact, i.e., prior to the first time the frictional sliding criterion is met. Thereafter the dynamicMu coefficient of friction is applied. By setting dynamicMu < staticMu, one can simulate the physical observation that the frictional force required to maintain sliding is less than the force necessary to initiate sliding.

Any given particle-pair undergoes either bonded interactions or frictional interactions but not both. This is achieved by specifying an exclusion between the two interaction groups:

```
#create an exclusion between bonded and frictional interactions:
sim.createExclusion (
interactionName1 = "pp_bonds",
interactionName2 = "friction"
)
```

Any acoustic emissions generated during fracturing should dissipate rapidly compared with the duration of the experiment. To simulate these conditions, it is necessary to incorporate two body forces designed to attenuate translational and rotational oscillations. In this case are used both LinDamping (designed to attenuate translational oscillations) and RotDamping (designed to attenuate rotational oscillations). The two damping forces are implemented as follows:

```
#add translational viscous damping:
sim.createInteractionGroup (
LinDampingPrms(
name="damping1",
viscosity=0.002,
maxIterations=50
)
)
#add rotational viscous damping:
sim.createInteractionGroup (
RotDampingPrms(
name="damping2",
viscosity=0.002,
maxIterations=50
)
)
```

The viscosity coefficients are chosen to be small so that damping has little effect on the elastic response of the simulated material, but sufficient to attenuate unwanted oscillations.

Frequently, it may be useful to incorporate fixed or movable walls in particle simulations. Walls may be planar, piecewise planar, or perhaps an arbitrary shape. ESyS-Particle implements three types of walls: Planar walls (infinite planar walls specified by a point and a normal vector), Linear meshes (a piece-wise linear mesh of line segments for arbitrarily shaped walls in 2D simulations), and Triangular meshes (a mesh of triangles used to define surfaces in 3D simulations). All three types of walls have an active side and an inactive side. For the case of an infinite wall, the normal vector points to the active side of the wall. Particles impinging on a wall from the active side will bounce off the wall. However, particles impinging on a wall from the inactive side will accelerate through the wall in an unphysical manner. Both types of mesh walls have an active side determined by the order in which vertices are specified for line-segments or triangles.

An infinite planar wall can be inserted as follows:

```
sim.createWall (
name = "right_wall",
posn = Vec3(30000.0, 0.0, 0.0),
normal = Vec3(-1.0, 0.0, 0.0)
)
```

The second argument (posn) is a Vec3 vector specifying a point lying in the plane of the wall. Finally the normal argument specifies a Vec3 normal vector for the wall.

Simply inserting a wall into a simulation object is insufficient. The type of interactions must also be defined between particles and walls. There are two common types of interactions: elastic repulsion and bonded interactions. In this code, only elastic repulsion is considered.

```
#specify elastic repulsion from the top wall:
sim.createInteractionGroup (
NRotElasticWallPrms (
name = "right_wall_repel",
wallName = "right_wall",
normalK = ym
)
)
```

Particle-wall interactions are also implemented through an InteractionGroup. The wallName argument specifies to which wall this particle-wall interaction refers. The last argument (normalK) specifies the elastic stiffness of the particle-wall interaction. The choice of elastic stiffness is not arbitrary. An elastic stiffness should be assigned sufficiently large that the wall can support the weight of the particle with a relatively small indentation (or overlap). If the elastic stiffness is too small the particle will continue to fall through the wall and eventually fall out on the other side.

Planar walls, by their definition, are infinite in length, making it difficult to simulate problems that require complex wall shapes or walls with holes. Mesh walls overcome this problem but are slightly more complicated to implement in simulations. ESyS-Particle uses a triangulated mesh format to define piecewise segments of a wall (Fig. B.2).

```
sim.readMesh(
fileName = "meshBottom.msh",
meshName = "meshBottom_wall"
)
```

Mesh walls are a powerful and flexible feature of ESyS-Particle that allow complex shapes and interactions to be simulated.

ESyS-Particle includes a group of modules called FieldSavers designed to store specific simulation data to disk. FieldSavers are closely related to the CheckPointer, with the main difference being that FieldSavers store only specific data rather than all of the state variables of the particles. FieldSavers can also be used to store data on particles (such as position or kinetic energy), interactions (such as potential energy and the number of broken bonds), and walls (such as the position of a wall and the net force acting on the wall).
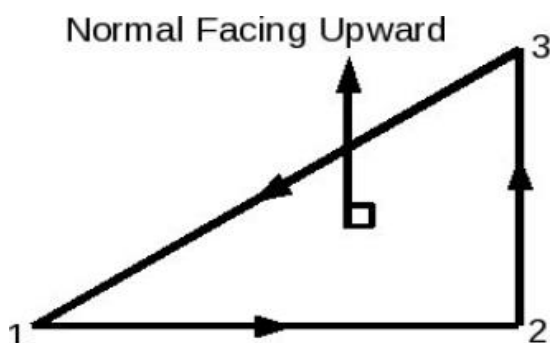

Fig. B.2. Triangulated piece of mesh wall.

```
#add a CheckPointer to store simulation data:
sim.createCheckPointer (
CheckPointPrms (
fileNamePrefix = "snapshot",
beginTimeStep = 0,
endTimeStep = time_steps,
timeStepIncr = check_pointer
)
)

#total kinetic energy
sim.createFieldSaver (
ParticleScalarFieldSaverPrms(
fieldName="e_kin",
fileName="ekin.dat",
fileFormat="SUM",
beginTimeStep=0,
endTimeStep=time_steps,
timeStepIncr=field_saver
)
)
```

References

Abe, S., and K. Mair (2005), Grain fracture in 3D numerical simulations of granular shear, *Geophys. Res. Lett.* **32**, 5, L05305, DOI: 10.1029/2004GL022123.

Abe, S., J.H. Dieterich, P. Mora, and D. Place (2002), Simulation of the Influence of rate- and state-dependent friction on the macroscopic behavior of complex fault zones with the lattice solid model, *Pure Appl. Geophys.* **159**, 1967–1983, DOI: 10.1007/s00024-002-8718-7.

Abe, S., van H. Gent, and J.L. Urai (2011), DEM simulation of normal faults in cohesive materials, *Tectonophysics* **512**, 1–4, 12-21, DOI: 10.1016/j.tecto.2011.09.008.

Abe, S., V. Boros, W. Hancock, and D. Weatherley (2014), ESyS-particle tutorial and user's guide. Version 2.3.1, https://launchpad.net/esys-particle.

Akazawa, T. (1943), New test method for evaluating internal stress due to compression of concrete: the splitting tension test, *J. Japan Soc. Civil. Eng.* **29**, 777–787.

Anderson, T.L. (1991), Fracture Mechanics: Fundamentals and Applications, CRC Press, Boca Raton.

Andrews, R.M. (1985), Measurement of the fracture toughness of glacier ice, *J. Glaciol.* **31**, 108, 171-176, DOI: 10.3189/S0022143000006420.

Åström, J.A., B.L. Holian, and J. Timonen (2000), Universality in fragmentation, *Phys. Rev. Lett.* **84**, 14, 3061-3064, DOI: 10.1103/PhysRevLett.84.3061.

Åström, J.A., D. Vallot, M. Schäfer, E.Z. Welty, S. O'Neel, T.C. Bartholomaus, Y. Liu, T.I. Riikilä, T. Zwinger, J. Timonen, and J.C. Moore (2014), Termini of calving glaciers as self-organized critical systems: Calving event catalogue, *Nature Geosci.* **7**, 874-878, DOI: 10.1038/ngeo2290.

Bahr, D.B. (1996), Analytical modeling of glacier dynamics, *Math. Geol.* **28**, 2, 229-251, DOI: 10.1007/BF02084214.

Balevičius, R., R. Kačianauskas, Z. Mroz, and I. Sielamowicz (2006), Discrete element method applied to multiobjective optimization of discharge flow parameters in hoppers, *Struct. Multidisc. Optim.* **31**, 3, 163-175, DOI: 10.1007/s00158-005-0596-z.

Barsom, J.M., ed. (1987), *Fracture Mechanics Retrospective*, American Society for Testing and Materials, Philadelphia 384 pp.

Behera, B., F. Kun, S. McNamara, and H.J. Herrmann (2005), *Fragmentation of a circular disc by impact on a frictionless plate*, *J. Phys.: Condens. Matter* **17**, 24, 2439, DOI: 10.1088/0953-8984/17/24/005.

Benn, D.I., N.R.J. Hulton, and R.H. Mottram (2007a), "Calving laws", "sliding laws" and the stability of tidewater glaciers, *Ann. Glaciol.* **46**, 1, 123-130, DOI: 10.3189/172756407782871161.

Benn, D.I., C.R. Warren, and R.H. Mottram (2007b), Calving processes and the dynamics of calving glaciers, *Earth-Science Rev.* **82**, 3-4, 143-179, DOI: 10.1016/j.earscirev.2007.02.002.

Bidgoli, M.N., Z. Zhao, and L. Jing (2013), Numerical evaluation of strength and deformability of fractured rocks, *J. Rock Mech. Geotech. Eng.* **5**, 6, 419-430, DOI: 10.1016/j.jrmge.2013.09.002.

Brennan, B.J. (1981), Linear viscoelastic behaviour in rocks. **In:** F.D. Stacey, M.S. Paterson, and A. Nicholas (eds.), *Anelasticity in the Earth*, Geodynamic Series, Vol. 4, AGU, Washington, DOI: 10.1029/GD004p0013.

Burgess, D.O., M.J. Sharp, D.W.F. Mair, J.A. Dowdeswell, and T.J. Benham (2005), Flow dynamics and iceberg calving rates of Devon Ice Cap, Nunavut, Canada, *J. Glaciol.* **51**, 173, 219-230, DOI: 10.3189/172756505781829430.

Cai, M. (2013), Fracture initiation and propagation in a Brazilian disc with a plane interface: a numerical study, *Rock Mech. Rock Eng.* **46**, 289–302, DOI: 10.1007/s00603-012-0331-1.

Cai, M., and P.K. Kaiser (2004), Numerical simulation of the Brazilian test and the tensile strength of anisotropic rocks and rocks with pre-existing cracks, *Int. J. Rock Mech. Min. Sci.* **41**, 3, 2B03, DOI: 10.1016/j.ijrmms.2004.03.086.

Carcione, J.M. (1990), Wave propagation in anisotropic linear viscoelastic media: theory and simulated wavefields, *Geophys. J. Int.* **101**, 3, 739–750, DOI: 10.1111/j.1365-246X.1990.tb05580.x.

Carcione, J.M. (1993), Seismic modeling in viscoelastic media, *Geophysics* **58**, 1, 10-179, DOI: 10.1190/1.1443340.

Carmona, H.A., F.K. Wittel, F. Kun, and H.J. Herrmann (2008), Fragmentation processes in impact of spheres, *Phys. Rev.* **E 77**, 5, 051302, DOI: 10.1103/PhysRevE.77.051302.

Carmona, H.A., F.K. Wittel, and F. Kun (2014), From fracture to fragmentation: discrete element modelling, *Eur. Phys. J. Spec. Top.* **223**, 2369–2382, DOI: 10.1140/epjst/e2014-02270-3.

Chaplin, M. (2016), Water Structure and Science. Ice phases, retrieved in June 2016, http://www1.lsbu.ac.uk/water/ice_phases.html.

Chaput, J., R.C. Aster, D. McGrath, M. Baker, R.E. Anthony, P. Gerstoft, P. Bromirski, A. Nyblade, R.A. Stephen, D.A. Wiens, S.B. Das, and L.A. Stevens (2018), Near-surface environmentally forced changes in the Ross Ice Shelf observed with ambient seismic noise, *Geophys. Res. Lett.* **45**, 20, 11187–11196, DOI: 10.1029/2018GL079665.

Christensen, R.M. (2010), *Theory of Viscoelasticity*, Dover Publications, New York.

Christensen, R.M. (2013), *The Theory of Materials Failure*, Oxford University Press, Oxford.

Claesson, J., and B. Bohloli (2002), Brazilian test: stress field and tensile strength of anisotropic rocks using an analytical solution, *Int. J. Rock Mech. Min. Sci.* **39**, 8, 991–1004, DOI: 10.1016/s1365-1609(02)00099-0.

Cohen, D., P. Lehmann, and D. Or (2009), Fiber bundle model for multiscale modeling of hydrome-chanical triggering of shallow landslides, *Water Resour. Res.* **45**, 10, DOI: 10.1029/2009WR 007889.

Collins, J.A. (1981), *Failure of Materials in Mechanical Design*, Wiley and Sons, New York.

Computational Research Grants on The Okeanos Supercomputer ICM UW, Project GC70-6, Project GB72-7.

Cook, J., J.E. Gordon, C.C. Evans, and D.M. Marsh (1964), A mechanism for the control of crack prop-agation in all-brittle systems, *Proc. R. Soc. London Ser. A. Math. Phys. Eng. Sci*. **282**, 1391, 508–520, DOI: 10.1098/rspa.1964.0248.

Courtney, T.H. (1990), *Mechanical Behavior of Materials*, McGraw-Hill, New York.

Cuffey, K.M., and W.S.B. Paterson (2010), *The Physics of Glaciers*, 4th ed., Elsevier, Massachusetts.

Cundall, P.A. (1971), A computer model for simulating progressive, large-scale movement in blocky rock systems, *Proc. Symp. Int. Soc. Rock Mech*. **2**, 8.

Cundall, P.A. (1974), A computer model for rock-mass behavior using interactive graphics for the input and output of geometrical data, National Technical Information Service, Report no. AD/A-001 602.

Cundall, P.A. (1978), BALL – A program to model granular media using the distinct element method, Technical Note, Advanced Technology Group, Dames and Moore, London.

Cundall, P.A., and O.D.L. Strack (1979), A discrete numerical model for granular assemblies, *Geotech-nique* **29**, 1, 47–65, DOI: 10.1680/geot.1979.29.1.47.

Czechowski, Z. (1991), A kinetic model of crack fusion, *Geophys. J. Int*. **104**, 2, 419–422, DOI: 10.1111/j.1365-246X.1991.tb02521.x.

Czechowski, Z. (1993), A kinetic model of nucleation, propagation and fusion of cracks, *J. Phys. Earth* **41**, 3, 127–137, DOI: 10.4294/jpe1952.41.127.

Czechowski, Z. (1995), Dynamics of fracturing and cracks. **In:** R. Teisseyre (ed.), *Theory of Earthquake Premonitory and Fracture Processes*, Polish Scientific Publishers PWN, Warszawa, 447–469.

Czechowski, Z. (1997), A kinetic model of macrocrack propagation, *Acta Geophys. Pol*. **45**, 3, 193–204.

Czechowski, Z. (1998), A generalized kinetic model of three component mixture of cracks, *Acta Geo-phys. Pol.* **46**, 4, 375–388.

Czechowski, Z. (2000), A stochastic approach to the cracktip propagation model, *Acta Geophys. Pol*. **48**, 1, 57–68.

Damsgaard, A., D.L. Egholm, J.A. Piotrowski, S. Tulaczyk, N.K. Larsen, and K. Tylmann (2013), Dis-crete element modeling of subglacial sediment deformation, *J. Geophys. Res.: Earth Surf.* **118**, 4, 2230–2242, DOI: 10.1002/2013JF002830.

de Berg, M., O. Cheong, M. van Kreveld, and M. Overmars (2008), *Computational Geometry. Algo-rithms and Applications*, 3rd ed., Springer-Verlag, Berlin Heidelberg.

Derski, W., R.J. Izbicki, L. Kisiel, and Z. Mróz (1982), *Mechanika Skał i Gruntów*, Państwowe Wydawnictwo Naukowe, Warszawa (in Polish).

Di Renzo, A., and F.P. Di Maio (2004), Comparison of contact-force models for the simulation of col-lisions in DEM-based granular flow codes, *Chem. Eng. Sci*. **59**, 3, 525-541, DOI: 10.1016/ j.ces.2003.09.037.

Dobrowolski, A.B. (1923), *Historja Naturalna Lodu*, Wydawnictwo Kasy Pomocy dla Osób Pracujących na Polu Naukowem im. D-ra J. Mianowskiego, Warszawa (in Polish).

Duan, K., C.Y. Kwok, and M. Pierce (2016), Discrete element method modeling of inherently aniso-tropic rocks under uniaxial compression loading, *Int. J. Num. Analytic. Meth. Geomech.* **40**, 8, 1150–1183, DOI: 10.1002/nag.2476.

Egholm, D.L. (2007), A new strategy for discrete element numerical models: 1. Theory, *J. Geophys. Res.* **112**, B5, B05203, DOI: 10.1029/2006JB004557.

Elliott, S.R. (1998), *The Physics and Chemistry of Solids*, John Wiley and Sons, Chichester, England.

Ergenzinger, C., R. Seifried, and P. Eberhard (2011), A discrete element model to describe failure of strong rock in uniaxial compression, *Granular Matter* **13**, 341–364, DOI: 10.1007/s10035-010-0230-7.

Eringen, A.C. (1962), *Nonlinear Theory of Continous Media*, McGraw-Hill Book Co., New York.

Exadaktylos, G.E., and K.N. Kaklis (2001), Applications of an explicit solution for the transversely isotropic circular disc compressed diametrically, *Int. J. Rock Mech. Min. Sci*. **38**, 2, 227–243, DOI: 10.1016/s1365-1609(00)00072-1.

Fakhimi, A., and E. Alavi Gharahbagh (2011), Discrete element analysis of the effect of pore size and pore distribution on the mechanical behavior of rock, *Int. J. Rock Mech. Min. Sci*. **48**, 1, 77–85, DOI: 10.1016/j.ijrmms.2010.08.007.

Farrington, R.J., L.N. Moresi, and F.A. Capitanio (2014), The role of viscoelasticity in subducting plates, *Geochem. Geophys. Geosyst*. **15**, 11, 4291–4304, DOI: 10.1002/2014GC005507.

Ferry, J.D. (1965), *Lepkosprężystość Polimerów*, Wydawnictwo Naukowo-Techniczne, Warszawa (in Polish).

Fraige, F.Y., and P.A. Langston (2004), Integration schemes and damping algorithms in distinct element models, *Adv. Powder Technol*. **15**, 2, 227–245, DOI: 10.1163/156855204773644454.

Freireich, B., R. Kumar, W. Ketterhagen, K. Su, C. Wassgren, and J.A. Zeitler (2015), Comparisons of intra-tablet coating variability using DEM simulations, asymptotic limit models, and experiments, *Chem. Eng. Sci*. **131**, 197–212, DOI: 10.1016/j.ces.2015.03.013.

Gagliardini, O., T. Zwinger, F. Gillet-Chaulet, G. Durand, L. Favier, B. de Fleurian, R. Greve, M. Malinen, C. Martin, P. Råback, J. Ruokolainen, M. Sacchettini, M. Schafer, H. Seddik, and J. Thies (2013), Capabilities and performance of Elmer/Ice, a new-generation ice sheet model, *Geoscien. Model Develop*. **6**, 4, 1299–1318, DOI: 10.5194/gmd-6-1299-2013.

Garbarczyk, J. (2000), *Wstęp do Fizyki Ciała Stałego*, Oficyna Wydawnicza Politechniki Warszawskiej, Warszawa (in Polish).

Glen, J.W. (1955), The creep of polycrystalline ice, *Proc. Roy. Soc. London A* **228**, 1175, 519–538, DOI: 10.1098/rspa.1955.0066.

Glowacki, O., G.B. Deane, M. Moskalik, Ph. Blondel, J. Tegowski, and M. Blaszczyk (2015), Underwater acoustic signatures of glacier calving, *Geophys. Res. Lett*. **42**, 3, 804–812, DOI: 10.1002/2014GL062859.

Głowacki, O., M. Moskalik, and G.B. Deane (2016), The impact of glacier meltwater on the underwater noise field in a glacial bay, J. *Geophys. Res. Oceans* **121**, 8455–8470, DOI: 10.1002/2016JC012355.

Gordon, J.E. (1976), *The New Science of Strong Materials, or Why You Don't Fall Through the Floor*, Princeton University Press.

Górski, M. (2014), *Seismic Events in Glaciers*, Geoplanet: Earth and Planetary Sciences, Springer, New York, 99 pp., DOI: 10.1007/978-3-642-31851-1.

Górski, M., and K.P. Teisseyre (2006), Glacier motion: seismic events and rotation/tilt phenomena. **In:** Teisseyre R., Takeo M., and Majewski E. (eds), *Earthquake Source Asymmetry, Structural Media and Rotation Effects*, Springer, Heidelberg, 199–215.

Greve, R., and H. Blatter (2009), *Dynamics of Ice Sheets and Glaciers*, Springer, Dordrecht.

Griffith, A.A. (1921), The phenomena of rupture and flow in solids, *Philosophic. Trans. Roy. Soc. London A*, **221**, 582–593, DOI: 10.1098/rsta.1921.0006.

Hansen, A., P.C. Hemmer, and S. Pradhan (2015), *The Fiber Bundle Model. Modeling Failure in Materials*, Wiley-VCH, Weinheim.

Herman, A. (2016), Discrete-Element bonded-particle Sea Ice model DESIgn, version 1.3a – model description and implementation, *Geosci. Model Dev*. **9**, 1219–1241, DOI: 10.5194/gmd-9-1219-2016.

Hertzberg, R.W. (1976), Deformation and Fracture Mechanics of Engineering Materials, Wiley, New York.

Hobbs, D.W. (1964), The tensile strength of rocks, *Int. J. Rock Mech. Min. Sci. Geomech. Abstr.* **1**, 3, 385–388, DOI: 10.1016/0148-9062(64)90005-1.

Hobbs, P.V. (1974), *Ice Physics*, Oxford University Press, Bristol.

Hudson, J.A., E.T. Brown, and F. Rummel (1972), The controlled failure of rock discs and rings loaded in diametral compression, *Int. J. Rock Mech. Min. Sci. Geomech. Abstr.* **9**, 2, 241–248, DOI: 10.1016/0148-9062(72)90025-3.

International Society for Rock Mechanics, Commission on Standardization of Laboratory and Field Tests (1978), Suggested methods for determining tensile strength of rock materials, *Int. J. Rock Mech. Min. Sci. Geomech. Abstr.* **15**, 3, 99–103, DOI: 10.1016/0148-9062(78)90003-7.

Irwin, G.R. (1948), *Fracturing of Metals*, American Society of Metals, Cleveland.

Jaeger, J.C., N.G.W. Cook, and R. Zimmerman (2007), *Fundamentals of Rock Mechanics*, 4th ed., Blackwell Publ., Malden, 488 pp.

Jania, J. (1997), *Glacjologia*, Państwowe Wydawnictwo Naukowe PWN, Warszawa (in Polish).

Jarosch, A.H. (2008), *Icetools: A full Stokes finite element model for glaciers*, *Comput. Geosci.* **34**, 8, 1005–1014, DOI: 10.1016/j.cageo.2007.06.012.

Jing, L., K.-B. Min, A. Baghbanan, and Z. Zhao (2013), Understanding coupled stress, flow and transport processes in fractured rocks, *Geosyst. Eng.* **16**, 1, 2–25, DOI: 10.1080/12269328.2013.780709.

Johnson, K.L. (1985), *Contact Mechanics*, Cambridge University Press, Cambridge.

Jouvet, G., M. Picasso, J. Rappaz, M. Huss, and M. Funk (2011), Modelling and numerical simulation of the dynamics of glaciers including local damage effects, *Math. Model. Natur. Phenom.* **6**, 5, 263–280, DOI: 10.1051/mmnp/20116510.

Kazerani, T. (2013), A discontinuum-based model to simulate compressive and tensile failure in sedimentary rock, *J. Rock Mech. Geotech. Eng.* **5**, 5, 378–388, DOI: 10.1016/j.jrmge.2013.07.002.

Kazerani, T., J. Zhao, and Z.Y. Yang (2010), Investigation of failure mode and shear strength of rock joints using discrete element method. **In:** J. Zhao, V. Labiouse, J.-P. Dudt, and J.-F. Mathier (eds), *Rock Mechanics in Cicil and Environmental Engineering*, Taylor, and Francis Group, London, 235–238.

Klejment, P., and W. Dębski (2017), Brazilian test – a macroscopic point of view on tensile fracture generation, Proc. V Int. Conf. Particle-based Methods – Fundamentals and Application, 78–89.

Klejment, P., and W. Dębski (2018), Crack nucleation in solid materials under external load – simulations with the Discrete Element Method, Proc. 12th Int. Fatigue Congr. (FATIGUE 2018) *MATEC Web Conf.* **165**, 22019, DOI: 10.1051/matecconf/201816522019.

Klejment, P., A. Kosmala, N. Foltyn, and W. Dębski (2016), Symulacje komputerowe parametrów mikroskopowych i makroskopowych materiałów przy pomocy Metody Elementów Dyskretnych. **In:** Ł. Koźmiński, J. Doskocz, and P. Kardasz (eds.), *Innowacje w Polskiej Nauce w Obszarze Matematyki i Informatyki*, Wyd. Nauka i Biznes, 5–19 (in Polish).

Klejment, P., W. Dębski, and A. Kosmala (2018a), Particle-based DEM model for simulating brittle cracks evolution in rock-like materials during the tensional fracturing process. **In:** E.E.Gdoutos (ed.), Proc. First Int. Conf. Theoretical, Applied and Experimental Mechanics, Springer, Cham, 215–220, DOI: 10.1007/978-3-319-91989-8_47.

Klejment, P., N. Foltyn, A. Kosmala, and W. Dębski (2018b), Discrete Element Method as the numerical tool for the hydraulic fracturing modelling. **In:** T. Zieliński, I. Sagan, and W. Surosz (eds.), *Interdisciplinary Approaches for Sustainable Development Goals*, Geoplanet: Earth and Planetary Sciences. Springer, Cham, 217–235, DOI: 10.1007/978-3-319-71788-3_15.

Knott, J.F. (1973), *Fundamentals of Fracture Mechanics*, Butterworths, London.

Komputery Dużej Mocy, Interdyscyplinarne Centrum Modelowania Matematycznego i Komputerowego, Uniwersytet Warszawski, http://kdm.icm.edu.pl/kdm/Witamy [accessed 28 July 2018].

Kruggel-Emden, H., M. Sturm, S. Wirtz, and V. Scherer (2008), Selection of an appropriate time integration scheme for the discrete element method (DEM), *Comput. Chem. Eng.* **32**, 10, 2263–2279, DOI: 10.1016/j.compchemeng.2007.11.002.

Kruggel-Emden, H., F. Stepanek, and A. Munjiza (2011), Performance of integration schemes in discrete element simulations of particle systems involving consecutive contacts, *Comput. Chem. Eng.* **35**, 10, 2152–2157, DOI: 10.1016/j.compchemeng.2010.09.008.

Kun, F., and H.J. Herrmann (1996), Fragmentation of colliding discs, *Int. J. Modern Phys. C* **7**, 6, 837–855, DOI: 10.1142/S0129183196000697.

Kun, F., and H.J. Herrmann (1999), Transition from damage to fragmentation in collision of solids, *Phys. Rev. E* **59**, 3, 2623–2632, DOI: 10.1103/PhysRevE.59.2623.

Kun, F., I. Varga, S. Lennartz-Sassinek, and I.G. Main (2013), Approach to failure in porous granular materials under compression, *Phys. Rev. E* **88**, 6, 1–11, DOI: 10.1103/PhysRevE.88.062207.

Kun, F., I. Varga, S. Lennartz-Sassinek, and I.G. Main (2014), Rupture cascades in a discrete element model of a porous sedimentary rock, *Phys. Rev. Lett.* **112**, 6, 1–5, DOI: 10.1103/PhysRevLett.112.065501.

Kundu, S., A. Stroisz, and S. Pradhan (2016), A simple discrete-element-model of Brazilian test, *The European Phys. J. B* **89**, 130–137, DOI: 10.1140/epjb/e2016-60915-y.

Kwapinska, M., G. Saage, and E. Tsotsas (2006), Mixing of particles in rotary drums: A comparison of discrete element simulations with experimental results and penetration models for thermal processes, *Powder Technol.* **161**, 1, 69–78, DOI: 10.1016/j.powtec.2005.08.038.

Lakes, R.S. (2009), *Viscoelastic Materials*, Cambridge University Press, New York.

Lambert, C., and C. Coll (2014), Discrete modeling of rock joints with a smooth-joint contact model, *J. Rock Mech. Geotech. Eng.* **6**, 1, 1–12, DOI: 10.1016/j.jrmge.2013.12.003.

Landau, L.D., and E.M. Lifshitz (1969), *Mechanics*, Course of Theoretical Physics, Vol. 1, Pergamon Press, Oxford.

Landau, L.D., and E.M. Lifshitz (1970), *Theory of Elasticity*, Course of Theoretical Physics, Vol. 7, 2nd ed., Pergamon Press, Oxford.

Landau, L.D., and E.M. Lifszic (1958), *Mechanika Ośrodków Ciągłych*, Państwowe Wydawnictwo Naukowe PWN, Warszawa (in Polish).

Lavrov, A., and A. Vervoort (2002), Theoretical treatment of tangential loading effects on the Brazilian test stress distribution, *Int. J. Rock Mech. Min. Sci.* **39**, 2, 275–283, DOI: 10.1016/s1365-1609(02)00010-2.

Le Meur, E., O. Gagliardini, T. Zwinger, and J. Ruokolainen (2004), Glacier flow modelling: a comparison of the shallow ice approximation and the full-Stokes solution, *C. R. Physique* **5**, 7, 709–722, DOI: 10.1016/j.crhy.2004.10.001.

Li, D., and L.N.Y. Wong (2013), The Brazilian disc test for rock mechanics applications: review and new insights, *Rock Mech. Rock Eng.* **46**, 2, 269–287, DOI: 10.1007/s00603-012-0257-7.

Li, Y.-G., ed. (2012), *Imaging, Modeling and Assimilation in Seismology*, De Gruyter, Berlin.

Lisjak, A., and G. Grasselli (2014), A review of discrete modeling techniques for fracturing processes in discontinuous rock masses, *J. Rock Mech. Geotech. Eng.* **6**, 4, 301–314, DOI: 10.1016/j.jrmge.2013.12.007.

Łuksza, J. (2014), *Mechanika Ośrodków Ciągłych: Wybrane Zagadnienia*, Redakcja Wydawnictw AGH, Kraków (in Polish).

Mavko, G., T. Mukerji, and J. Dvorkin (1998), *The Rock Physics Handbook. Tools for Seismic Analysis in Porous Media*, Cambridge University Press, Cambridge.

McCrum, N.G., C.P. Buckley, and C.B. Bucknall (1997), *Principles of Polymer Engineering*, 2nd ed., Oxford University Press, Oxford.

Meyers, M.A., and K.K. Chawla (2008), *Mechanical Behavior of Materials*, Cambridge University Press, Cambridge.

Mora, P., and D. Place (1993), A lattice solid model for the nonlinear dynamics of earthquakes, *Int. J. Modern Phys. C* **4**, 6, 1059–1074, DOI: 10.1142/S0129183193000823.

Mora, P., and D. Place (1994), Simulation of the frictional stick-slip instability, *Pure Appl. Geophys.* **143**, 61–87, DOI: 10.1007/BF00874324.

Morton, R.L. (2002), *Music of the Earth: Volcanoes, Earthquakes, and Other Geological Wonders*, Basic Books.

Munjiza, A. (2004), *The Combined Finite-Discrete Element Method*, John Wiley & Sons, Chichester.

Neimitz, A. (1998), *Mechanika Pękania*, Państwowe Wydawnictwo Naukowe PWN, Warszawa (in Polish).

Nick, F.M., C.J. van der Veen, A. Vieli, and D.I. Benn (2010), A physically based calving model applied to marine outlet glaciers and implications for the glacier dynamics, *J. Glaciol.* **56**, 199, 781–794, DOI: 10.3189/002214310794457344.

Nitka, M., and J. Tejchman (2015), Modelling of concrete behaviour in uniaxial compression and tension with DEM, *Granular Matter* **17**, 1, 145–164, DOI: 10.1007/s10035-015-0546-4.

Nouguier-Lehon, C., B. Cambou, and E. Vincens (2003), Influence of particle shape and angularity on the behaviour of granular materials: a numerical analysis, *Int. J. Num. Analytic. Meth. Geomech.* **27**, 14, 1207–1226, DOI: 10.1002/nag.314.

O'Sullivan, C. (2011), *Particulate Discrete Element Modelling: A Geomechanics Perspective*, Spon Press/Taylor and Francis, London.

O'Sullivan, C., and J.D. Bray (2004), Selecting a suitable time step for discrete element simulations that use the central difference time integration scheme, *Eng. Comput.* 21, 2–4, 278–303, DOI: 10.1108/02644400410519794.

Onate, E., and J. Rojek (2004), Combination of discrete element and finite element methods for dynamic analysis of geomechanics problems, *Computer Meth. Appl. Mech. Eng.* **193**, 27–29, 3087–3128, DOI: 10.1016/j.cma.2003.12.056.

Orowan, E. (1949), Fracture and strength of solids, *Rep. Prog. Phys.* **12**, 1, 185–232, DOI: 10.1088/0034-4885/12/1/309.

Pál, G., I. Varga, and F. Kun (2014), Emergence of energy dependence in the fragmentation of heterogenous materials, *Phys. Rev. E* **90**, 6, 1–8, DOI: 10.1103/PhysRevE.90.062811.

Pestel, E.C., and F.A. Leckie (1963), *Matrix Methods in Elastomechanics*, McGraw-Hill Book Co., New York.

Petrov, V.A., V.I. Vladimirov, and A.N. Orlov (1970), A kinetic approach to fracture of solids. I. General theorie, *Phys. Stat. Sol.* **42**, 1, 197–206, DOI: 10.1002/pssb.19700420121.

Place, D., F. Lombard, P. Mora, and S. Abe (2002), Simulation of the micro-physics of rocks using LSMearth, *Pure Appl. Geophys.* **159**, 9, 1911–1932, 10.1007/978-3-0348-8203-3_2.

Potyondy, D.O., and P.A. Cundall (2004), A bonded-particle model for rock, *Int. J. Rock Mech. Min. Sci.* **41**, 8, 1329–1364, DOI: 10.1016/j.ijrmms.2004.09.011.

Riikilä, T. (2017), Discrete element model for viscoelastic materials with brittle fracture: Applications on glacier dynamics, Ph.D. Thesis, University of Jyväskylä, Department of Physics.

Riikilä, T., T. Tallinen, J. Åström, and J. Timonen (2015), A discrete-element model for viscoelastic deformation and fracture of glacial ice, *Comp. Phys. Commun.* **195**, 14–22, DOI: 10.1016/j.cpc.2015.04.009.

Robel, A.A. (2017), Thinning sea ice weakens buttressing force of iceberg mélange and promotes calving, *Nat. Commun.* **8**, 14596, DOI: 10.1038/ncomms14596.

Rojek, J. (2007), Modelowanie i symulacja komputerowa złożonych zagadnień mechaniki nieliniowej metodami elementów skończonych i dyskretnych, Prace IPPT PAN, Warszawa (in Polish).

Rong, G., G. Liu, D. Hou, and C. Zhou (2013), Effect of particle shape on mechanical behaviors of rocks: A numerical study using clumped particle model, *Sci. World J.* **2013**, 589215, DOI: 10.1155/2013/589215.

Rougier, E., A. Munjiza, and N.W.M. John (2004), Numerical comparison of some explicit time integration schemes used in DEM, FEM/DEM and molecular dynamics, *Int. J. Num. Meth. Eng.* **61**, 6, 856–879, DOI: 10.1002/nme.1092.

Roylance, D. (2001a), *Engineering Viscoelasticity*, Department of Materials Science and Engineering, Massachusetts Institute of Technology, Cambridge, 37 pp.

Roylance, D. (2001b), *Introduction to Fracture Mechanics*, Department of Materials Science and Engineering, Massachusetts Institute of Technology, Cambridge, 17 pp.

Rymarz, Cz. (1993), *Mechanika Ośrodków Ciągłych*, Państwowe Wydawnictwo Naukowe PWN, Warszawa (in Polish).

Sadd, M.H. (2009), *Elasticity—Theory, Applications and Numerics*, 2nd ed., Academic Press, Burlington, USA.

Sator, N., and H. Hietala (2010), Damage in impact fragmentation, *Int. J. Fract.* **163**, 1, 101–108, DOI: 10.1007/s10704-009-9406-8.

Sator, N., S. Mechkov, and F. Sausset (2008), Generic behaviours in impact fragmentation, *Europhys. Lett.* **81**, 4, 1–6, DOI: 10.1209/0295-5075/81/44002.

Scholtes, L., and F.V. Donze (2012), Modelling progressive failure in fractured rock masses using a 3D discrete element method, *Int. J. Rock Mech. Min. Sci.* **52**, 18–30, DOI: 10.1016/j.ijrmms.2012.02.009.

Schulson, E.M., and P. Duval (2009), *Creep and Fracture of Ice*, Cambridge University Press, Cambridge.

Seweryn, A. (2003), *Metody Numeryczne w Mechanice Pękania*, IPPT PAN, Warszawa (in Polish).

Shimizu, H., T. Koyama, T. Ishida, M. Chijimatsu, T. Fujita, and S. Nakama (2010), Distinct element analysis for Class II behavior of rocks under uniaxial compression, *Int. J. Rock Mech. Min. Sci.* **47**, 2, 323–333, DOI: 10.1016/j.ijrmms.2009.09.012.

Sochor, M. (1998), *Strength of Materials I*, CTU Publishing House, Prague.

Stacey, T.R. (1981), A simple extension strain criterion for fracture of brittle rock, *Int. J. Rock Mech. Min. Sci. Geomech. Abstr.* **18**, 6, 469–474, DOI: 10.1016/0148-9062(81)90511-8.

Strawley, J.E., and W.F. Brown (1965), *Fracture Toughness Testing*, ASTM STP 381, 133.

Strzelecki, M.C., A.J. Long, J.M. Lloyd, J. Małecki, P. Zagórski, Ł. Pawłowski, and M.W. Jaskólski (2018), The role of rapid glacier retreat and landscape transformation in controlling the post-Little Ice Age evolution of paraglacial coasts in central Spitsbergen (Billefjorden, Svalbard), *Land Degrad. Develop.* **29**, 6, 1962–1978, DOI: 10.1002/ldr.2923.

Tanner, R.I. (2000), *Engineering Rheology*, Oxford University Press, Oxford.

Teisseyre, R., ed. (1995), *Theory of Earthquake Premonitory and Fracture Processes*, Polish Scientific Publishers PWN, Warszawa.

Tetelman, A.S., and A.J. McEvily, Jr. (1967), *Fracture of Structural Materials*, Wiley and Sons, New York.

Timár, G., J. Blömer, F. Kun, and H.J. Herrmann (2010), New universality class for the fragmentation of plastic materials, *Phys. Rev. Lett.* **104**, 9, 1–4, DOI: 10.1103/PhysRevLett.104.095502.

Timco, G.W., and R.M.W. Frederking (1996), A review of sea ice density, *Cold Regions Sci. Technol.* **24**, 1, 1–6, DOI: 10.1016/0165-232X(95)00007-X.

Timco, G.W., and W.F. Weeks (2010), A review of the engineering properties of sea ice, *Cold Regions Sci. Technol.* **60**, 2, 107–129, DOI: 10.1016/j.coldregions.2009.10.003.

Udias, A., R. Madariaga, and E. Buforn (2014), *Source Mechanisms of Earthquakes: Theory and Practice*, Cambridge University Press, Cambridge.

Verlet, L. (1967), Computer "experiments" on classical fluids. I. Thermodynamical properties of Lennard-Jones molecules, *Phys. Rev.* **159**, 1, 98–103, DOI:10.1103/PhysRev.159.98.

Vesga, L.F., L.E. Vallejo, and S. Lobo-Guerrero (2008), DEM analysis of the crack propagation in brittle clays under uniaxial compression tests, Int. J. Num. Analytic. Meth. Geomech. **32**, 11, 1405–1415, DOI: 10.1002/nag.665.

Walter, F., S. O'Neel, D. McNamara, W.T. Pfeffer, J.N. Bassis, and H.A. Fricker (2010), Iceberg calving during transition from grounded to floating ice: Columbia Glacier, Alaska, *Geophys. Res. Lett.* **37**, 15, 1–5, DOI: 10.1029/2010GL043201.

Wang, Y.C. (2009), A new algorithm to model the dynamics of 3-D bonded rigid bodies with rotations, *Acta Geotech.* **4**, 2, 117-127, DOI: 10.1007/s11440-008-0072-1.

Wang, Y.C., P. Mora, C. Yin, and D. Place (2004), Statistical tests of Load-Unload Response Ratio signals by Lattice Solid Model: Implication to tidal triggering and earthquake prediction, *Pure Apl. Geophys.* **161**, 1829–1839, DOI: 10.1007/s00024-004-2534-1.

Wang, Y.C., S. Xue, and J. Xie (2012), Discrete element method and its applications in earthquake and rock fracture modelling. **In:** Y.-G. Li (ed.) *Imaging, Modeling and Assimilation in Seismology*, De Gruyter, 235–262.

Weatherley, D. (2015), What are the different advantages of three DEM open-source software: Yade, ESyS-Particle and LIGGGHTS?, available from: https://www.researchgate.net/post/What_are_the_different_advantages_of_three_DEM_open-source_software_Yade_ESyS-Particle_and_LIGGGHTS (accessed: 28 July 2018).

Weatherley, D.K., V.E. Boros, W.R. Hancock, and S. Abe (2010), Scaling benchmark of ESyS-Particle for elastic wave propagation simulations, 2010 IEEE Sixth Int. Conf. e-Science, Brisbane, Australia, 277–283, DOI: 10.1109/eScience.2010.40.

Weeks, W., and A. Assur (1967), *The Mechanical Properties of Sea Ice*, Monograph II-C, U.S. Army Materiel Command, Cold Regions Research and Engineering Laboratory, Hanover, New Hampshire.

Wiącek, J., M. Molenda, J. Horabik, and J.Y. Ooi (2012), Influence of grain shape and intergranular friction on material behavior in uniaxial compression: Experimental and DEM modeling, *Powder Technol.* **217**, 435–442, DOI: 10.1016/j.powtec.2011.10.060.

Williams, J.R., Hocking G., and Mustoe G. G. W. (1985), The theoretical basis of the discrete element method. **In:** *Proc. NUMETA '85 Conference "Numerical Methods of Engineering, Theory and Applications"*, Balkema, Rotterdam, 897-906.

Wolff, M.F.H., V. Salikov, S. Antonyuk, S. Heinrich, and G.A. Schneider (2013), Three-dimensional discrete element modeling of micromechanical bending tests of ceramic-polymer composite materials, *Powder Technol.* **248**, 77–83, DOI: 10.1016/j.powtec.2013.07.009.

Yang, R., W. Mao, and X. Chang (2015), An efficient seismic modeling in viscoelastic isotropic media, *Geophysics* **80**, 1, T63–T81, DOI: 10.1190/geo2013-0439.1.

Yang, S.-Q., Y.-H. Huang, H.-W. Jing and H.-R. Liu (2014), Discrete element modeling on fracture coalescence behavior of red sandstone containing two unparallel fissures under uniaxial compression, *Eng. Geol.* **178**, 28–48, DOI: 10.1016/j.enggeo.2014.06.005.

Zehnder, A.T. (2012), *Fracture Mechanics*, Series Lecture Notes in Applied and Computational Mechanics, Vol. 62, Springer, London.

Zhang, Z.F., and J. Eckert (2005), Unified tensile fracture criterion, *Phys. Rev. Lett.* **94**, 9, 1–4, DOI: 10.1103/PhysRevLett.94.094301.

Zhao, Z. (2017), Application of discrete element approach in fractured rock masses. **In:** A.K. Shojaei and J. Shao (eds.), *Porous Rock Fracture Mechanics with Application to Hydraulic Fracturing, Drilling and Structural Engineering*, Woodhead Publ., 145–176.

Zhu, W.C., and C.A. Tang (2006), Numerical simulation of Brazilian disk rock failure under static and dynamic loading, *Int. J. Rock Mech. Min. Sci. Geomech. Abstr.* **43**, 2, 236–252, DOI: 10.1016/j.ijrmms.2005.06.008.

Zwinger, T., and J.C. Moore (2009), Diagnostic and prognostic simulations with a full Stokes model accounting for superimposed ice of Midtre Lovénbreen, Svalbard, *The Cryosphere* **3**, 217–229.

"Publications of the Institute of Geophysics, Polish Academy of Sciences: Geophysical Data Bases, Processing and Instrumentation" appears in the following series:

A – Physics of the Earth's Interior

B – Seismology

C – Geomagnetism

D – Physics of the Atmosphere

E – Hydrology (formerly Water Resources)

P – Polar Research

M – Miscellanea

Every volume has two numbers: the first one is the consecutive number of the journal and the second one (in brackets) is the current number in the series.